A finite elements method to solve the Bloch-Torrey equation applied to diffusion magnetic resonance imaging of biological tissues

Dang Van Nguyen

Thèse

Présentée pour obtenir le grade de

DOCTEUR DE L'ÉCOLE POLYTECHNIQUE

Spécialité : Mathématiques Appliquées

par

Dang Van NGUYEN

A finite elements method to solve the Bloch-Torrey equation applied to diffusion magnetic resonance imaging of biological tissues

Soutenue le 7 Mars 2014 devant le jury composé de :

M.	**Denis GREBENKOV**	Co-Directeur de Thèse
M.	**Houssem HADDAR**	Examinateur
M.	**Johan JANSSON**	Rapporteur
M.	**Denis LE BIHAN**	Rapporteur
Mme.	**Jing-Rebecca LI**	Directeur de Thèse
M.	**Rachid TOUZANI**	Rapporteur

Acknowledgment

First and foremost I would like to express my deepest gratitude to my supervisors, Dr. Jing-Rebecca Li and Dr. Denis Grebenkov, who have supported me during my thesis with their enthusiasm and patience. Knowing and working with them is a great chance for me to enrich my knowledge not only about my current work but also about my own life.

I would like to thank Dr. Denis Le Bihan and Dr. Cyril Poupon who have facilitated good conditions for my work during the time I worked at Neurospin, CEA Saclay.

I am very thankful for all helpful discussions in the launchpad with Fenics supporters during the course of our code development. I am grateful to J. Jansson and J. Hoffman at the KTH, Sweden for their welcome and help during and after our visit.

Related to the use of the Salome platform, we would like to thank Christophe Bourcier, Nathalie Gore and Serge Rehbinder in the Laboratoire de Genie Logiciel et de Simulation at the CEA, Saclay, France.

In current work related to the formulation and simulation on the new interface conditions, I also wish to thank Dr. Houssem Haddar and Caubet Fabien for their help.

Finally, I would like to thank all my friends and my family, especially my wife Bich Loan for their encouragement to help me overcome some difficult periods.

This work is funded in part by the ANR (Agence Nationale de la Recherche), project 'SIMUDMRI'.

Contents

Thesis summary

Diffusion magnetic resonance imaging (dMRI) is a non-invasive imaging technique that gives a measure of the diffusion characteristics of water in biological tissues, notably, in the brain. The hindrances that the microscopic cellular structure poses to water diffusion are statistically aggregated into the measurable macroscopic dMRI signal. Inferring the microscopic structure of the tissue from the dMRI signal allows one to detect pathological regions and to monitor functional properties of the brain. For this purpose, one needs a clearer understanding of the relation between the tissue microstructure and the dMRI signal. This requires novel numerical tools capable of simulating the dMRI signal arising from complex microscopic geometrical models of tissues.

We formulate and implement such a numerical approach based on the linear finite elements method (FEM) for the multi-compartment Bloch-Torrey partial differential equation (PDE) that allows us to work with general gradient pulses and relatively complex geometries. To compute the long-time effective diffusion tensor predicted by homogenization theory, we also considered the solution of the related steady-state Laplace equations.

Compatible with the linear finite elements discretization, we used linear approximation of the cellular interfaces. The semi-permeable biological cell membranes were modeled by zero-volume elements to allow jumps in the finite elements solution on the membranes. The computational domain was periodically extended by applying the appropriate artificial boundary conditions. This allows us to reduce the edge effects caused by artificial boundaries. This finite elements discretization is second order accurate in space.

The spatial discretization was then coupled to the adaptive explicit Runge-Kutta Chebyshev (RKC) time stepping method that is second order accurate in time. Being an explicit time stepping method, this choice has the advantage that the linear system to be solved at each time step involves only the mass matrix.

Furthermore, using a transformation of the Bloch-Torrey PDE, we reduced the oscillations in the sought-after solution and simplified the implementation of the artificial boundary conditions. In this way, we were able to keep the mass matrix of our FEM real-valued and time-independent after applying the boundary conditions. Because it is real-valued, the mass matrix is only half the size compared to a naive implementation without the transformation. Due to the time independence, the mass matrix only needs to be assembled and the artificial boundary conditions

applied once before the time integration.

In short, our method can bring improvements in the computational time, memory usage, and the accuracy of dMRI signal simulations. Our method was implemented on the FeniCS C++ platform. The finite elements meshes were obtained using the mesh generator Salome that gives an efficient way to manage complex domains with multiple compartments and periodic boundaries.

Next, we considered three application areas for the dMRI simulation method that we have developed.

In the first application, we investigated the long-time asymptotic behavior of the dMRI signal and showed the convergence of the apparent diffusion tensor to the effective diffusion tensor predicted by homogenization. Due to the long history of homogenization techniques and the existence of important results developed using these techniques, we expect that some useful information about biological structures can be revealed by the analysis of the effective diffusion tensor. This would be an easier task than a direct analysis on the time-dependent Bloch-Torrey PDE.

For the second application, we numerically verified that the dMRI signal of a three-compartment model of the biological cell, with a thick membrane layer between the cell interior and the extra-cellular space, approaches that of the two-compartment model of the biological cell, with an infinitely thin and semi-permeable interface between the cell interior and the extra-cellular space. For the three-compartment model, we implemented both isotropic and anisotropic diffusion in the membrane layer and showed both choices lead to dMRI signals that approaches the dMRI signal of the two-compartment model, with the convergence being faster for the case where there is fast tangential diffusion.

In the third application we validated the macroscopic Kärger model of dMRI signal that takes into account inter-compartmental exchange. We verified that the Kärger model is valid for narrow pulse gradients and at low permeabilities.

In the last part of this thesis, we simulated and analyzed the dMRI signal arising from isolated neurons. First, we proposed numerical (PDE) models for accurately computing the dMRI signal inside isolated neurons that is more efficient than full 3D simulation, namely, by reducing the simulation on the 3D neurites tree to a simulation on a 1D neurites tree. We showed that the computational time is greatly reduced while the accuracy is preserved. Then we numerically investigated the water exchange between the soma and its connected neurites tree and concluded that the exchange is negligible under normal dMRI acquisition conditions. Next, we compared our simulation results to a previously published semi-analytical dMRI signal model for neurites. We fitted this dMRI signal model to simulation results on several classes of neurites trees in an attempt to estimate the average branch length of the neurites tree. Finally, we also proposed upper and lower bounds for the dMRI signal for neurites trees and numerically verified those bounds for several classes of neurites trees.

This thesis has 5 chapters and they are organized as follows. In chapter 1, we briefly introduce dMRI concepts as well as related equations and existing works.

In chapter 2, we propose a numerical method based on linear finite elements that allows for more accurate descriptions of complex geometries. Three applications of our method to study diffusion inside multi-compartment models are considered in chapter 3. In chapter 4, we propose two models of the dMRI signals inside isolated neurons. Chapter 5 contains our conclusions and future work.

List of publications

1. D. V. Nguyen, J. R. Li, D. Grebenkov, D. Le Bihan, *Reduced PDE models of the diffusion MRI signal contribution from neurons.* (in preparation)

2. D. V. Nguyen, J.-R. Li, D. S. Grebenkov, and D. Le Bihan, *A finite elements method to solve the Bloch-Torrey equation applied to diffusion magnetic resonance imaging*, J. Comput. Phys. 263, 283-302 (2014).

3. D. V. Nguyen, D. S. Grebenkov, C. Poupon, D. Le Bihan, and J.-R. Li, *Effective diffusion tensor computed by homogenization*, Diff. Fundam. 18 (9), 1-6 (2013).

4. D. V. Nguyen, J. R. Li, D. Grebenkov, D. Le Bihan, *Modeling the diffusion magnetic resonance imaging signal inside neurons*, IC-MSQUARE2013. Open Access Journal of Physics: IOP Conference Series (Accepted - 2013).

Chapter 1

Introduction

1.1 Background

Diffusion magnetic resonance imaging (dMRI) is an imaging modality that gives a measure of the diffusion characteristics of water in tissue during a diffusion time in the range of tens of milliseconds [3, 14, 37, 38, 75], at the spatial resolution on the order of 1 mm^3, meaning the signal acquired represents the average diffusion characteristics in a volume, called a voxel, of that size. While a major application of dMRI has been acute cerebral ischemia (stroke) [49, 77], dMRI is used to image almost every part of the human body. In the brain, dMRI has been used to detect a wide range of physiological and pathological conditions, including tumors [46, 60, 69, 74], myelination abnormalities [25], connectivity [36], as well as in functional imaging where recent work has suggested that water dMRI could also be used to visualize changes in tissue microstructure that might arise during neuronal activation [40].

The microscopic cellular structure of tissue in the brain is very complicated. There are many types of cells in a voxel, including neurons and glial cells, all embedded in the extra-cellular space. Neurons have a solid cell body called the soma that measures 1 to 10μm in diameter. Attached to the soma are long protrusions called neurites (axons and branching dendrites) that measure, respectively, 0.5 and 0.9μm in average diameter, and can be several hundreds of μm in length. The glial cells do not have long protrusions and the tissue is densely packed with cells. In the cortex, soma occupy 11% and the rest includes 34% axons, 35% dendrites, 14% spines and 6% extracellular space in volume [17] (see also in [79]). Averaged over all the brain tissues, the range of the extracellular space volume fraction is between 15 and 30% in the normal adult, with a typical value of 20%, and this fraction falls to 5% during global ischemia whereas the true size of the spaces between cells is less obvious. Recent study indicates that the true average width of the extracellular space in the in vivo rat cortex lies between 38 and 64nm [71]. The cellular organization is complex. The cells of the cortex are organized into layers, with columns of cells linking the different layers. The cells are usually permeable. Water can move between the cells and the extra-cellular space, except across the myelin layer of the myelinated axons.

DMRI is limited to a range of diffusion times it can measure due to biological and technical reasons. In the brain, diffusion times in the range of $1\text{ms} - 100\text{ms}$ can be measured, associated to average diffusion distances of $2.5\mu\text{m} - 25\mu\text{m}$. This distance is averaged over all water molecules. The actual diffusion distance can be different depending on whether the water molecules are in the neuronal bodies, the neurites (dendrites and axons) or the extra-cellular space. If diffusion is homogeneous with diffusion coefficient D, this distance is given by $\ell_D = \sqrt{2\,d\,D\,t_D}$, where d is the problem dimension and t_D is the diffusion time.

1.2 Equations of diffusion MRI

Suppose r_1, r_2, r_3 are the axes of a 3D coordinate system. Inside the MRI scanner, a strong static magnetic field of magnitude B_0 is induced along the positive r_3-direction, and the spins of the water protons inside the body become aligned to this magnetic field, resulting in a net magnetization in the positive r_3-direction. When a time-varying magnetic field (much weaker than the static magnetic field) is applied for a short time at the resonance frequency, $\omega_0 = \gamma B_0$, where $\gamma = 2.67513 \times 10^8\,\text{rad}\,\text{s}^{-1}\text{T}^{-1}$ is the gyromagnetic ratio, the net magnetization is tipped off the r_3-axis. We consider a so-called 90° pulse, an oscillating magnetic field that tips the net magnetization onto the $r_1 - r_2$ plane. The spins then precess around the r_3-axis, inducing a voltage in a receive coil. The net magnetization in the $r_1 - r_2$ (transverse plane to the direction of the main magnetic field) can be measured as a signal.

The net magnetization will realign along the r_3-direction, due to two relaxation effects: the spin-lattice relaxation of the net magnetization along the r_3-direction to its original value, and the spin-spin relaxation of the decay of the net magnetization in the $r_1 - r_2$ plane to zero. The rate constant of the first relaxation is called T_1 and the rate constant of the second kind of relaxation is called T_2. Both T_1 and T_2 vary according to the tissue environment. Additionally, the spin density also varies with the tissue environment.

In addition to T_2 (spin-spin) relaxation, local inhomogeneities also contribute to the signal decay. The latter can be partially canceled by a refocusing 180° pulse, applied at time $t = TE/2$ after the 90° pulse, producing an echo at time TE, that gives a measurable signal that will have the correct contribution from T_2. Such a sequence of applied magnetic fields is called a spin echo sequence.

The spatial encoding of the signal is obtained by applying additional magnetic fields in the r_3 direction, called magnetic field gradients, that vary linearly in space: $\mathbf{r} \cdot \mathbf{G_{im}}(t)$, where $\mathbf{G_{im}}(t)$ will be called the imaging gradient. In the rotating frame at the frequency ω_0, the complex transverse magnetization on the $r_1 - r_2$ plane, $M(\mathbf{r}, t) := M_{r_1}(\mathbf{r}, t) + I M_{r_2}(\mathbf{r}, t)$, (where I is the imaginary unit), obeys the Bloch equation [5]:

$$\frac{\partial M(\mathbf{r}, t)}{\partial t} = -I\gamma\, \mathbf{r} \cdot \mathbf{G_{im}}(t) M(\mathbf{r}, t) - \frac{M(\mathbf{r}, t)}{T_2(\mathbf{r})}, \tag{1.1}$$

where $T_2(\mathbf{r})$ is the local spin-spin relaxation rate. The solution of Eq. (1.1) is

$$M(\mathbf{r},t) = \rho(\mathbf{r})\ \exp\!\left(-\frac{t}{T_2(\mathbf{r})} - I\,\gamma\,\mathbf{r}\cdot\int_0^t \mathbf{G_{im}}(s)\,ds\right),$$

where $t=0$ is the start of the 90° pulse and $\rho(\mathbf{r})$ is the initial transverse magnetization.

Even though 3D imaging is possible, most often the MRI signal is acquired in 2D, slice by slice. Suppose $r_3 \in \left[\left(l-\frac{1}{2}\right)\Delta r_3, \left(l+\frac{1}{2}\right)\Delta r_3\right]$ are the limits of the slice of interest. By choosing $\mathbf{G_{im}}(t) = (0, G_2, 0)$ for a time interval Δt_2 and then choosing $\mathbf{G_{im}}(t) = (G_1, 0, 0)$ for a time interval Δt_1, then the magnetization at $\mathbf{r}$ at TE is

$$M(\mathbf{r},TE) = \rho(\mathbf{r})\ \exp\!\left(-\frac{TE}{T_2(\mathbf{r})} - I\,(k_1 r_1 + k_2 r_2)\right),$$

where $k_1 = \gamma G_1 \Delta t_1$ and $k_2 = \gamma G_2 \Delta t_2$. The MRI signal, acquired at echo time $t = TE$, is the integral of the magnetization in that slice:

$$\widehat{\mu}_l\,(k_1,k_2) = \int_{r_1,r_2} \mu_l(r_1,r_2)\ \exp\!\Big(-I(k_1 r_1 + k_2 r_2)\Big)\,dr_1 dr_2, \tag{1.2}$$

where the contrast function is:

$$\mu_l(r_1,r_2) = \int_{(l-\frac{1}{2})\Delta r_3}^{(l+\frac{1}{2})\Delta r_3} \rho(r_1,r_2,r_3)\ \exp\!\left(-\frac{TE}{T_2(r_1,r_2,r_3)}\right) dr_3. \tag{1.3}$$

It is clear that the MRI signal in Eq. (1.2) is the 2D Fourier transform of the contrast function in Eq. (1.3).

By the appropriate choice of G_1, G_2, and Δt_1 and Δt_2 the Fourier transform can be obtained at a set of 2D Fourier points. Then the inverse Fourier transform can be performed and then sampled at physical space points to obtain in each voxel, $V_{i,j,l}$ where

$$\begin{aligned} V_{i,j,l} := &\left[\left(i-\frac{1}{2}\right)\Delta r_1, \left(i+\frac{1}{2}\right)\Delta r_1\right] \times \left[\left(j-\frac{1}{2}\right)\Delta r_2, \left(j+\frac{1}{2}\right)\Delta r_2\right] \\ &\times \left[\left(l-\frac{1}{2}\right)\Delta r_3, \left(l+\frac{1}{2}\right)\Delta r_3\right], \end{aligned}$$

an average value of the contrast function:

$$\bar{\mu}_l(i,j) \approx \int_{V_{i,j,l}} \rho(r_1,r_2,r_3)\ \exp\!\left(-\frac{TE}{T_2(r_1,r_2,r_3)}\right) dr_1\,dr_2\,dr_3, \tag{1.4}$$

that can be displayed in an image. In Eq. (1.4) we can see two widely used contrast mechanisms in MRI, the spin density and the T_2 relaxation.

Besides the spin density and the T_2 relaxation, water diffusion in the tissue is another source of contrast. This contrast can be encoded by the application of another magnetic field gradient $\mathbf{G_{df}}(t)$. One pulse of the gradient is applied in the direction $\mathbf{g}$ before 180° refocusing pulse and the same pulse after. The lack of complete refocusing is due to water diffusion and gives the diffusion MRI contrast.

The mathematical description of the complex transverse magnetization including effects of diffusion is called the Bloch-Torrey equation [73]:

$$\frac{\partial M(\mathbf{r},t)}{\partial t} = -I\gamma\ \mathbf{r}\cdot\mathbf{G_{im}}(t)\, M(\mathbf{r},t) - \frac{M(\mathbf{r},t)}{T_2(\mathbf{r})} - I\gamma\ \mathbf{r}\cdot\mathbf{G_{df}}(t)\, M(\mathbf{r},t) + \nabla\cdot\Big(\mathbf{D}(\mathbf{r})\nabla M(\mathbf{r},t)\Big), \tag{1.5}$$

where $\mathbf{G_{df}}(t) = \mathbf{g}\ f(t)$, $f(t)$ containing the time profile information of the diffusion-encoding gradient, $\mathbf{D}(\mathbf{r})$ is the (possibly discontinuous) *intrinsic* diffusion tensor. The last term in the above equation concerns diffusion (random movement) of water molecules.

Among numerous time profiles, two profiles are most commonly used:

1. The pulsed-gradient spin echo (PGSE) sequence [66], with two rectangular pulses of duration δ, separated by a time interval $\Delta - \delta$, for which the profile $f(t)$ is

$$f(t) = \begin{cases} 1, & t_1 \le t \le t_1 + \delta, \\ -1, & t_1 + \Delta < t \le t_1 + \Delta + \delta, \\ 0, & \text{otherwise}, \end{cases} \tag{1.6}$$

   where t_1 is the starting time of the first pulse and $\frac{TE}{2}$, the time of the application of the 180 degree refocusing pulse, is between $t_1 + \delta$ and $t_1 + \Delta$. See Figure 1.1a.

2. The oscillating gradient spin echo (OGSE) sequence [15] has been recently introduced to access short diffusion times. An OGSE sequence usually consists of two oscillating pulses of duration σ, each containing n periods, hence the frequency is $\omega = n\frac{2\pi}{\sigma}$, separated by a time interval $\tau - \sigma$ (Figure 1.1b). For a cosine OGSE [8, 15], the profile $f(t)$ is

$$f(t) = \begin{cases} \cos\left(n\frac{2\pi}{\sigma}t\right), & t_1 < t \le t_1 + \sigma, \\ -\cos\left(n\frac{2\pi}{\sigma}(t-\tau)\right), & t_1 + \tau < t \le t_1 + \tau + \sigma, \\ 0, & \text{otherwise}, \end{cases} \tag{1.7}$$

   where $t_1 + \sigma \le \dfrac{TE}{2} \le t_1 + \tau$. See Figure 1.1b.

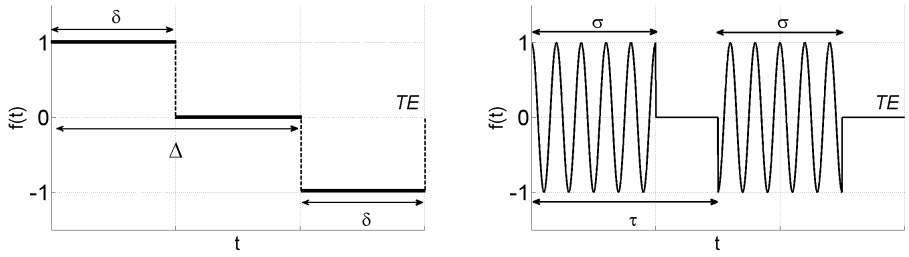

(a) (b)

Figure 1.1: A PGSE sequence (1.1a) and a cos-OGSE sequence (1.1b) for $t_1 = 0$.

In the rest of the thesis, we will neglect the imaging gradients and focus on the contrast function. T_2 effects will also be neglected. Hence, we will analyze and solve the following Bloch-Torrey PDE:

$$\frac{\partial M(\mathbf{r},t)}{\partial t} = -I\gamma\, \mathbf{r}\cdot\mathbf{g}\; f(t)\, M(\mathbf{r},t) + \nabla\cdot\Big(\mathbf{D}(\mathbf{r})\nabla M(\mathbf{r},t)\Big), \tag{1.8}$$

instead of the more complete description of Eq. (1.5). After solving Eq. (1.8) up to $t = TE$, we compute the average value of the contrast function inside the voxel:

$$S = \int\limits_{V_{i,j,l}} M(\mathbf{r},TE)d\mathbf{r}, \tag{1.9}$$

which is called the diffusion MRI signal.

1.3 The apparent diffusion coefficient

Under the assumption that water molecules experience a homogeneous isotropic diffusion environment characterized by the diffusion coefficient D, one can solve Eq. (1.8) in free space. Using the separation of variables [57],

$$M(\mathbf{r},t) = S(t)\, \exp\Big(I\varphi(\mathbf{r},t)\Big), \tag{1.10}$$

and subtituting Eq. (1.10) to Eq. (1.8) and defining the spin phase $\varphi(x,t)$:

$$\varphi(\mathbf{r},t) = \gamma\, \mathbf{g}\cdot\mathbf{r} \int\limits_0^t f(s)\, ds, \tag{1.11}$$

one obtains:

$$\frac{\partial S(t)}{\partial t} = -S(t)\, \Big(\nabla\varphi\Big)^T D\, \Big(\nabla\varphi\Big). \tag{1.12}$$

So,

$$S(TE) = S(0)\exp\Big(-b\, D\Big), \tag{1.13}$$

where the b-value is a weighting factor,

$$b = \gamma^2 \|\mathbf{g}\|^2 \int_0^{TE} du \left(\int_0^u f(s) ds \right)^2 . \tag{1.14}$$

For PGSE, the b-value is [66]:

$$b(\mathbf{g}, \delta, \Delta) = \gamma^2 \|\mathbf{g}\|^2 \delta^2 \left(\Delta - \frac{\delta}{3} \right). \tag{1.15}$$

For the cosine OGSE with *integer* number of periods n in each of the two durations σ, the corresponding b-value is [78]:

$$b(\mathbf{g}, \sigma) = \gamma^2 \|\mathbf{g}\|^2 \frac{\sigma^3}{4n^2\pi^2} = \gamma^2 \|\mathbf{g}\|^2 \frac{\sigma}{\omega^2}. \tag{1.16}$$

The same results also can be obtained using the Fourier transform for 1D free space where $\mathbf{r} = r$ and $\mathbf{g} = g$:

$$\begin{aligned} M(r,t) &= \frac{1}{2\pi} \int_{-\infty}^{\infty} \widehat{M}(k,t) \, \exp\Big(I \, k \, r\Big) \, dk, \\ \widehat{M}(k,t) &= \int_{-\infty}^{\infty} M(r,t) \, \exp\Big(-I \, k \, r\Big) \, dx. \end{aligned} \tag{1.17}$$

The exact solution in the Fourier domain was computed to be [33]:

$$\widehat{M}(k,t) = \widehat{M}\left(k + \gamma \, g \int_0^t f(s) \, ds, 0 \right) \exp\left(-D \int_0^t du \left(k + \gamma \, g \int_u^t f(s) \, ds \right)^2 \right), \tag{1.18}$$

and the signal to be:

$$\begin{aligned} S &= \int_{-\infty}^{+\infty} M(r,t) \, dx = \lim_{k \to 0} \widehat{M}(k,t) \\ &= \widehat{M}\left(\gamma \, g \int_0^t f(s) \, ds, 0 \right) \exp\left(-D \int_0^t du \left(\gamma \, g \int_u^t f(s) \, ds \right)^2 \right). \end{aligned} \tag{1.19}$$

When the initial condition is the Dirac delta function, the signal is

$$S = \exp\Big(-\bar{b} \, D\Big), \tag{1.20}$$

and the b-value is

$$\bar{b} = \int_0^{TE} du \left(\gamma \, g \int_u^{TE} f(s) \, ds \right)^2 . \tag{1.21}$$

We note that although Eq. (1.21) is different from Eq. (1.14) at some $t < TE$, they are identical at $t = TE$ for PGSE and OGSE sequences. Eq. (1.14) is preferred because it is based on the uniform distribution as the initial condition.

The basis of diffusion weighted imaging is that the MRI signal is acquired with a diffusion gradient $\mathbf{g}$ as well as with no diffusion gradient. The first image (after inverse Fourier transform) is divided by the second image in order to estimate $D(r_1, r_2, r_3)$ in each voxel, through the so-called "Apparent Diffusion Coefficient" (ADC):

$$ADC := -\frac{\partial}{\partial b} \log \frac{S(b, TE)}{S(0, TE)}\bigg|_{b=0}, \tag{1.22}$$

which serves as a contrast mechanism. See Figure 1.2 for examples of different MRI contrasts, the last one (D), being the ADC contrast.

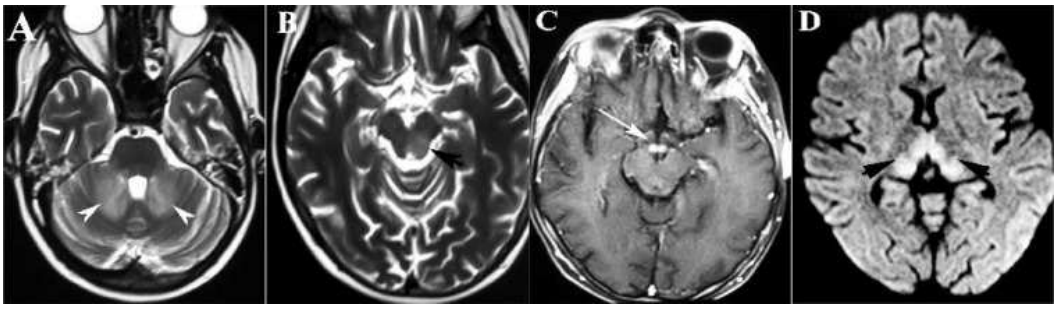

Figure 1.2: Image from Wikimedia Commons. Description: *Brain MRIs demonstrating hyperintense lesions in middle cerebellar peduncles on axial T2 weighted brain MRI (Part A), similar intensities in the tectum and tegmentum of midbrain on the left side (Part B), intense enhancement of mammillary bodies on the T1 weighted MRI with contrast (Part C), and hyperintense lesions in the medial portions of thalami in diffusion weighted MRI (Part D).* Source: `http://www.ncbi.nlm.nih.gov/pmc/articles/PMC3533170/`, Author: Ghorbani et al

1.4 Multiple compartments Bloch-Torrey PDE

It was realized that when the diffusion gradient $\mathbf{g}$ is varied in magnitude or direction, the *ADC* may change significantly. Also, different values of the ADC are obtained when Δ is varied. By fixing the direction of $\mathbf{g}$ and Δ (as well as the pulse duration δ) and varying the amplitude $\|\mathbf{g}\|$, one can see clearly that the diffusion-induced MRI signal attenuation is not a decaying exponential in b [9, 12, 28, 44, 45, 50, 52]. The reason for this is that in biological tissue, the diffusion environment seen by water molecules during the diffusion time (tens of milliseconds) is not homogeneous due to the presence of cells membranes and other heterogeneities. It also cannot be described simply by a *homogenized* diffusion coefficient.

Thus, inside the voxel, we define a geometrical model of tissue, made up of an extra-cellular space, Ω^0, and M non-overlapping biological cells defined by open sets: $\Omega^l \in \mathbb{R}^d$, $l = 1, \ldots, M$, where $\Omega^l \cap \Omega^n = \varnothing$ for $l \neq n$, and d is the space dimension (typically $d = 2$ or $d = 3$). We also allow the possibility of adding a membrane compartment around each biological cell. In this case, there would be

additional M membrane compartments: Ω^l, $l = M+1, \ldots, 2M$. If the membrane compartments are not included in the tissue model, then they are approximated by the semi-permeable interface conditions between the cell compartments and the extra-cellular space. We denote the interface between Ω^l and Ω^n by $\Gamma^{ln} = \overline{\Omega^l} \cap \overline{\Omega^n}$. When we do not need to distinguish between the individual cells, we will group all the cells into one intra-cellular compartment Ω^c, and all the membranes into one membrane compartment Ω^m, and the extra-cellular space will be denoted by Ω^e.

Ideally, the total computational volume $\cup_{l=1}\overline{\Omega^l}$ would be on the scale of the diffusion MRI resolution, usually on the order of 1 mm^3. However, due to the fact that cell features are on the scale of microns, typically a small portion of the tissue contributing to the signal in an imaging pixel is simulated. We denote this portion of tissue by C for the computational domain. Typically, $C = [-L/2, L/2]^d$ is a box that contains a "representative volume" of the tissue in the voxel under study. To simplify the notation, we will assume that any parts of biological cells that are outside of C will be removed so that $C = \bigcup \overline{\Omega^l}$. In addition, we will define $\Gamma = \bigcup \Gamma^{ln} \backslash \partial C$ to be the union of the interfaces minus the boundary of C.

In each compartment Ω^l, the complex transverse magnetization $M(\mathbf{r}, t)$ also satisfies the Bloch-Torrey PDE (1.8):

$$\frac{\partial}{\partial t} M(\mathbf{r}, t) = -I\gamma f(t) \mathcal{G}(\mathbf{r})\, M(\mathbf{r}, t) + \nabla \cdot \Big(\mathbf{D}(\mathbf{r}) \nabla M(\mathbf{r}, t) \Big), \quad \mathbf{r} \in \cup \Omega^l, \tag{1.23}$$

This equation needs to be supplemented by interface conditions at the interfaces Γ^{ln}, and by boundary conditions on ∂C. Let M^k and $\mathbf{D}^k$ be restrictions of M and $\mathbf{D}$ onto the k^{th} compartment (that take the appropriate limiting values in the case when M and $\mathbf{D}$ are discontinuous). The two interface conditions are the flux continuity [20]:

$$\mathbf{D}^l(\mathbf{r}) \nabla M^l(\mathbf{r}, t) \cdot \mathbf{n}^l = -\mathbf{D}^n(\mathbf{r}) \nabla M^n(\mathbf{r}, t) \cdot \mathbf{n}^n, \quad \mathbf{r} \in \Gamma^{ln}, \quad \forall\, l, n, \tag{1.24}$$

and a condition that incorporates a permeability coefficient κ^{ln} across Γ^{ln}:

$$\mathbf{D}^l(\mathbf{r}) \nabla M^l(\mathbf{r}, t) \cdot \mathbf{n}^l = \kappa^{ln} \Big(M^n(\mathbf{r}, t) - M^l(\mathbf{r}, t) \Big), \quad \mathbf{r} \in \Gamma^{ln}, \forall\, l, n, (l \neq n), \tag{1.25}$$

where $\mathbf{n}^k$ is a normal vector pointing outward from Ω^k. If the permeability coefficient is the same at all the interfaces, then we will simply use the notation κ.

In the limit $\kappa^{ln} = \infty$, Eq. (1.25) reduces to the simple continuity condition on $M(\mathbf{r}, t)$:

$$M^l(\mathbf{r}, t) = M^n(\mathbf{r}, t). \tag{1.26}$$

Following [78], we extend C by periodic copies of itself to handle the diffusion of water molecules close to the boundary of C. According to [78], the two boundary conditions on ∂C are

$$M(\mathbf{r}, t)|_{r_i = -L/2} = M(\mathbf{r}, t)|_{r_i = L/2} \exp\Big(I\, \theta_i(t) \Big), \quad i = 1, \cdots, d, \tag{1.27}$$

$$\frac{\partial M(\mathbf{r}, t)}{\partial r_i}\bigg|_{r_i = -L/2} = \frac{\partial M(\mathbf{r}, t)}{\partial r_i}\bigg|_{r_i = L/2} \exp\Big(I\, \theta_i(t) \Big), \quad i = 1, \cdots, d, \tag{1.28}$$

where $\mathbf{r} = (r_1, \cdots, r_d)$,

$$\theta_i(t) := \gamma\, g_i\, L \int_0^t f(s)\, ds,$$

and $\mathbf{g} = (g_1, \cdots, g_d)$. The PDE in Eq. (1.23) also needs an initial condition:

$$M^l(\mathbf{r}, 0) = \rho^l, \qquad \mathbf{r} \in \Omega^l, \quad \forall\, l, \tag{1.29}$$

where ρ^l is the initial transverse magnetization in Ω^l.

The complete multiple compartments Bloch-Torrey PDE problem to be solved involves the PDE (1.23), the two interface conditions Eqs. (1.24,1.25), the two boundary conditions Eqs. (1.27,1.28), and the initial condition Eq. (1.29).

The dMRI signal measured (without the imaging gradients and T_2 effects) is

$$S(b) := \sum_l \int_{\mathbf{r}\in\Omega^l} M^l(\mathbf{r}, TE)\, d\mathbf{r}. \tag{1.30}$$

In a dMRI experiment, the TE and sequence $f(t)$ are usually fixed while $\mathbf{g}$ is varied in amplitude or/and in direction to obtain the signal at different b-values. The ADC (Eq. 1.22) gives an indication of the effective mean squared distance traveled by water molecules, averaged over all starting positions.

1.5 Laplace PDE for the homogenized diffusion tensor

If there is no jump in the magnetization, and supposing the infinite periodic extension of the computational domain C, the effective diffusion tensor in the limit of infinite time, $\mathbf{D}^{\text{hom}}$, can be obtained by homogenization [4]. If there is a jump in the magnetization, the effective diffusion tensor from homogenization can be found in [10]. The apparent diffusion coefficient (ADC) is related to $\mathbf{D}^{\text{hom}}$ by:

$$ADC \to \frac{\mathbf{g}^T}{\|\mathbf{g}\|}\mathbf{D}^{\text{hom}}\frac{\mathbf{g}}{\|\mathbf{g}\|},$$

where $\mathbf{D}^{\text{hom}}$ is the homogenized diffusion tensor that can be obtained by solving the following d steady-state Laplace equations for $W_i(\mathbf{r})$, $i = 1, \ldots, d$, over C [10]:

$$\nabla \cdot \Big(D(\mathbf{r}) \nabla W_i(\mathbf{r}) \Big) = 0, \quad \mathbf{r} \in \cup\Omega^l, \tag{1.31}$$

with the same interface conditions in Eqs. (1.24,1.25) as for the Bloch-Torrey equation, and two simpler boundary conditions on ∂C:

$$W_i(\mathbf{r})|_{r_k=-L/2} = W_i(\mathbf{r})|_{r_k=L/2} - \delta_{i,k}\, L, \quad k = 1, \cdots, d, \tag{1.32}$$

$$\frac{\partial}{\partial r_k} W_i(\mathbf{r})\Big|_{r_k=-L/2} = \frac{\partial}{\partial r_k} W_i(\mathbf{r})\Big|_{r_k=L/2}, \quad k = 1, \cdots, d, \tag{1.33}$$

where $\delta_{i,k} = 1$ for $k = i$, and 0 otherwise. The problem to be solved consists of Eqs. (1.31,1.24,1.25,1.32,1.33), for $i = 1, \cdots, d$.

The entries of the homogenized tensor $\mathbf{D}^{\text{hom}}$ are then given by:

$$\{\mathbf{D}^{\text{hom}}\}_{i,k} = \int_C \mathbf{D}(\mathbf{r}) \nabla W_i(\mathbf{r}) \cdot \mathbf{e}_k \, d\mathbf{r}, \quad i,k = 1, \ldots, d, \tag{1.34}$$

where $\mathbf{e}_k$ is the unit vector in the k^{th} direction.

1.6 Explicit solutions and approximations

1.6.1 Explicit solution

For the PGSE sequence, there exists an analytical solution of the Bloch-Torrey PDE (1.8), proposed in [33]. On the computational box $C = [-L/2, L/2]^d$, if the initial condition is the Dirac delta distribution at $\mathbf{r}_0 = (r_1^0, \ldots, r_d^0) \in C$, with the diffusion gradient vector $\mathbf{g} = (g_1, \ldots, g_d)$, spatial position $\mathbf{r} = (r_1, \ldots, r_d)$ and constant diffusion coefficient D, then

$$M(r_1, \ldots, r_d, t) = \sum_{n_1=-\infty}^{\infty} \cdots \sum_{n_d=-\infty}^{\infty} \prod_{i=1}^{d} \widetilde{M}(r_i, r_i^0 + n_i L, g_i, t),$$

where,

- if $0 < t \leq \delta$:

$$\widetilde{M}(r, r_0, g, t) = \frac{1}{2\sqrt{\pi t D}} \exp\left(\frac{-I}{2} t \, g \, \gamma (r_0 + r) - \frac{t^4 \, D^2 \, g^2 \gamma^2 + 3 \, (r - r_0)^2}{12 \, D \, t} \right),$$

- if $\delta \leq t \leq \Delta$:

$$\widetilde{M}(r, r_0, g, t) = \frac{1}{2\sqrt{\pi \, D \, t}} \exp\left(-\frac{D \, g^2 \gamma^2 \delta^3 \, (-3\,\delta + 4\,t)}{12\,t} \right) \times \exp\left(\frac{-I \, g \gamma \, \delta \Big((2\,t - \delta) \, r_0 + \delta \, r \Big)}{2\,t} - \frac{(r - r_0)^2}{4 \, D \, t} \right)$$

- if $\Delta \leq t \leq \Delta + \delta$:

$$\begin{aligned} \widetilde{M}(r, r_0, g, t) = \frac{1}{2\sqrt{\pi \, D \, t}} & \exp\left(\frac{I \, g \gamma \, (-\delta^2 + t^2 - \Delta^2) \, (r + r_0)}{2\,t} - \frac{(r - r_0)^2}{4 \, D \, t} \right) \\ & \times \exp\left(\frac{-I \, g \gamma \, (-\delta^2 - \Delta^2 + t\delta + t\Delta) \, (r_0)}{t} + \frac{D \, g^2 \gamma^2 \, (\delta^2 + \Delta^2)^2}{4\,t} \right) \\ & \times \exp\left(-\frac{1}{12} \, D \, g^2 \gamma^2 t^3 + \frac{1}{2} \, D \, g^2 \gamma^2 \left(\delta^2 + \Delta^2 \right) t \right) \\ & \times \exp\left(-\frac{D \, g^2 \gamma^2 \, (\delta^3 + 2\,\Delta^3 + 3\,\delta^2 \Delta)}{3} \right), \end{aligned}$$

- if $t > \Delta + \delta$:

$$\widetilde{M}(r, r_0, g, t) = \frac{1}{2\sqrt{\pi\, t\, D}} \exp\left(\frac{D\, g^2\gamma^2\delta^3\,(-\delta + 2\,\Delta)}{3\,t} + \frac{I\, g\gamma\,(r - r_0)\,\Delta\,\delta}{t}\right) \times \exp\left(-\frac{D\, g^2\gamma^2\delta^2\,(-\delta + 3\,\Delta)\,(t - \Delta - \delta)}{3\,t} - \frac{(r - r_0)^2}{4\,t\,D}\right),$$

is a solution of Eq. (1.23) and also satisfies the pseudo-periodic boundary conditions Eqs. (1.27, 1.28). We will use it in later sections as a reference solution.

1.6.2 Narrow pulse approximation

For the PGSE sequence, when the duration of the diffusion gradient pulse, δ, is sufficiently small compared to the interval between pulses: $\delta \ll \Delta$, the influence of the diffusion-encoding magnetic field gradient pulse on the complex transverse magnetization due to water molecules starting at $\mathbf{r}_0$ at $t = t_1$ can be described by a gain of the complex phase $\exp\Big(-I\gamma\mathbf{g}\cdot\mathbf{r}_0\ \delta\Big)$ between t_1 and $t_1 + \delta$. Then, the magnetization due to water molecules at position $\mathbf{r}$ at $t_1 + \Delta$ acquires a complex phase $\exp\Big(I\gamma\mathbf{g}\cdot\mathbf{r}\ \delta\Big)$ between $t_1 + \Delta$ and $t_1 + \Delta + \delta$. Thus, the effect on the MRI signal, compared to having no diffusion gradient $\mathbf{g}$, due to water molecules at $\mathbf{r}_0$ when $t = t_1$, is:

$$\int_{\mathbf{r}\in V_{i,j,l}} P(\mathbf{r}, \mathbf{r}_0, \Delta)\ \exp\left(I\gamma\,\mathbf{g}\cdot(\mathbf{r} - \mathbf{r}_0)\ \delta\right),$$

where the diffusion propagator $P(\mathbf{r}, \mathbf{r}_0, \Delta)$ is the solution to the diffusion equation, i.e., the Bloch-Torrey PDE with $\mathbf{g} = 0$. The narrow pulse assumption allows for the use of classical results about the diffusion equation rather than deriving them for the more complicated Bloch-Torrey PDE.

1.6.3 Gaussian phase approximation

Another way to compute the dMRI signal is based on distribution functions for phases. Different from the narrow pulse approximation, the phases are not only considered at the starting and the ending position but also accumulated along the full molecule trajectory:

$$\varphi(TE) = \gamma \int_0^{TE} dt\, \mathbf{g}\cdot\mathbf{r}. \tag{1.35}$$

The expression for the signal is the average of all contributions of individual molecules:

$$S = S_0 \left\langle \exp\Big(-I\varphi(TE)\Big)\right\rangle. \tag{1.36}$$

For unrestricted diffusion it is simply:

$$S = S_0\ \exp\left(-\frac{1}{2}\Big\langle\varphi^2(TE)\Big\rangle\right), \tag{1.37}$$

where

$$\Big\langle \varphi^2(TE) \Big\rangle = \frac{2\,\gamma^2}{|\Omega|} \int_0^{TE} dt_1 \int_0^{t_1} dt_2 \int_\Omega d\mathbf{r}_1 \int_\Omega d\mathbf{r}_2\, (\mathbf{g}\cdot\mathbf{r}_1)(\mathbf{g}\cdot\mathbf{r}_2)\, P(\mathbf{r}_1,\mathbf{r}_2,t_1-t_2), \quad (1.38)$$

and

$$P(\mathbf{r}_1,\mathbf{r}_2,t_1-t_2) = \frac{1}{\Big(4\pi D(t_1-t_2)\Big)^{\frac{d}{2}}} \exp\left(-\frac{\|\mathbf{r}_1-\mathbf{r}_2\|^2}{4D(t_1-t_2)}\right). \quad (1.39)$$

The signal for PGSE sequence is then:

$$S = S_0\, \exp\Big(-b\,D\Big), \quad (1.40)$$

where $b = \gamma^2\|\mathbf{g}\|^2\delta^2\left(\Delta - \frac{\delta}{3}\right)$.

In the frame of the Gaussian phase approximation (first proposed by Neuman [51]), one neglects the second and higher-order terms in the cumulant expansion of the dMRI signal over the b-value (see the review [19] for details). The signal is therefore approximated as $S(b) = S(0)\exp(-bD_{\text{eff}})$, where the effective (or apparent) diffusion coefficient D_{eff} depends on sequence timing and profile, and on the geometrical confinement. For a given temporal profile $f(t)$ and arbitrary bounded domain Ω, one can get an explicit analytical formula for D_{eff}. For instance, if the temporal profile consists of two rectangular gradient pulses of duration δ separated by diffusion time Δ (Figure 1.1a), one gets [19]:

$$D_{\text{eff}} = \frac{1}{\delta^2(\Delta-\delta/3)} \times \sum_{m=0}^{\infty} \mathcal{B}_{0,m}^2 \left(\frac{2\delta}{D\lambda_m} - \frac{2 + e^{-D\lambda_m(\Delta+\delta)} + e^{-D\lambda_m(\Delta-\delta)} - 2e^{-D\lambda_m\Delta} - 2e^{-D\lambda_m\delta}}{D^2\lambda_m^2} \right), \quad (1.41)$$

where λ_m and $u_m(\mathbf{r})$ are the eigenvalues and eigenfunctions of the Laplace operator in the studied domain Ω: $\nabla^2 u_m(\mathbf{r}) + \lambda_m u_m(\mathbf{r}) = 0$, with reflecting (Neumann) boundary condition. The coefficients $\mathcal{B}_{0,m} = \int_\Omega d\mathbf{r}\; u_m(\mathbf{r})(\mathbf{q}\cdot\mathbf{r})$ determine the projection of the gradient (here $\mathbf{q} = \mathbf{g}/\|\mathbf{g}\|$ is the direction of the gradient) onto the eigenfunctions. For simple shapes such as segment, disk or sphere, the Laplacian eigenbasis is known analytically that allows one to compute explicitly D_{eff}. These representations are summarized in [19]:

• For a segment of length L with reflecting endpoints, one has

$$\lambda_m = \pi^2 m^2/L^2,\; B_{0,m} = L \times \begin{cases} \sqrt{2}\Big((-1)^m - 1\Big)/(\pi^2 m^2) & (m>0), \\ 1/2 & (m=0) \end{cases} \qquad (m = 0,1,2,...). \quad (1.42)$$

• For a disk of radius L with reflecting boundary, one has

$$\lambda_m = \alpha_m^2/L^2, \quad B_{0,m} = L\frac{\sqrt{2}}{\alpha_m\sqrt{\alpha_m^2-1}} \qquad (m = 0,1,2,...), \quad (1.43)$$

in which $\alpha_0,\ \alpha_1, \ldots$ are all positive solutions of the equation $J_1'(z) = 0$, where $J_1'(z)$ is the derivative of the Bessel function $J_1(z)$ of the first kind

$$\alpha_m = 1.8412, \quad 5.3314, \quad 8.5363, \quad 11.7060, \quad 14.8636, \ldots$$

For practical computation, the infinite series in Eq. (1.41) is truncated, given that the eigenvalues λ_m rapidly grow with the index m.

Chapter 2

A finite elements method to solve the multi-compartment Bloch-Torrey equation

Summary A finite elements method is formulated and implemented to solve the steady-state Laplace equation and the time-dependent Bloch-Torrey equation on multi-compartment domains. The computational domains are periodically extended by appropriate boundary conditions. The semi-permeable interface conditions are implemented by allowing jumps in the solution using double nodes. Using a transformation of the Bloch-Torrey PDE we reduce oscillations in the solution and simplify the implementation of the pseudo-periodic boundary conditions. The spatial discretization is then coupled to the adaptive Runge-Kutta-Chebychev time stepping method. Our method is second order accurate in space and second order accurate in time. We implement this method on the FEniCS C++ platform and show time and spatial convergence results.

2.1 Introduction

Biological tissue is a heterogeneous medium, consisting of cells of various sizes and shapes distributed in the extra-cellular space. The cells are separated from each other and from the extra-cellular space by the cell membranes. When water passes very slowly between the cells and the extra-cellular space as compared to the diffusion time, the cell membranes can be approximated as impermeable to water. In this case, various analytical or semi-analytical expressions have been obtained for the dMRI signal arising from *inside* the cells [8, 19, 54, 55, 67, 70]. In general, however, cell membranes are permeable to water, and it is important to study the effect of membrane permeability on the dMRI signal by using a richer numerical model.

In this chapter, we focus on a mathematical model called the multiple compartment Bloch-Torrey partial differential equation (PDE), which is a generalization

of the Bloch-Torrey PDE [73] to heterogeneous domains [20, 55]. This PDE describes the water proton magnetization subject to diffusion-encoding magnetic field gradient pulses and the dMRI signal is given by the integral of the magnetization. The above analytical models can be thought of as starting with the multiple compartment Bloch-Torrey PDE and then using simplifying assumptions to arrive at (semi-)analytical expressions for the dMRI signal.

Numerical solutions of the multiple compartment Bloch-Torrey PDE were reported in [24, 26, 58, 78], in which the finite difference method on a uniform Cartesian grid was coupled to the explicit Forward Euler time-stepping method. This approach is first order accurate in space and time. A finite elements method coupled to the implicit Backward Euler time-stepping has been recently proposed to solve the diffusion equation with Neumann boundary conditions to study the diffusion in the short gradient pulse limit for some simple geometries [48]. With linear basis functions, this approach is first order accurate in time and second order accurate in space. Our approach also uses a finite elements discretization but for the multi-compartment Bloch-Torrey equation so that we can work for general gradient pulses as well as multi-compartment domains. Because of the finite elements discretization, the cellular interfaces are described more accurately. We implemented linear elements to ensure second order spatial convergence. For the time integration, we used an efficient adaptive time-stepping method, called the Runge-Kutta Chebyshev (RKC) method [63]. The RKC method has second order time convergence, whereas the Forward Euler method used in [24, 26, 58, 78] is first order convergent in time. More importantly, the RKC method is adaptive in time as it takes steps commensurate with the desired accuracy of the solution during the course of the simulation. In the case of moderate desired solution accuracy, the RKC time integrator is preferred to the explicit Forward Euler method because in the latter, the time step size is usually limited by numerical stability for diffusive-type problems. We used the formulation in which the computational domain is assumed to be periodically extended to infinity in all three coordinate directions.

In addition, we also solved steady-state Laplace PDEs that produce the homogenized diffusion tensor that describes diffusion in a heterogeneous medium in the long time limit.

For an efficient implementation of finite elements we chose to base our code on the FEniCS Finite Elements platform [43]. The Bloch-Torrey PDE has several unconventional features that cause implementation issues for a standard PDE platform such as FEniCS. We describe these issues and how we resolved them. First, we allowed jumps in the finite elements solution at the compartment interfaces by implementing double-nodes at the interfaces. Second, the pseudo-periodic boundary conditions resulting from the periodic extension of the computational domain are reduced to standard periodic boundary conditions by transforming the Bloch-Torrey PDE, as in [58]. We note, however, that in [58], the discretized PDE using centered finite difference did not take into account first order terms. To obtain second order convergence in space, we had to include all the appropriate first order terms in our discretization. Third, we reformulated the Bloch-Torrey PDE so that the real and imaginary parts of the magnetization are decoupled to allow the solution of two

systems of half the number of unknowns compared to a naive implementation. We then show accuracy and timing results for our method.

The chapter is organized as follows. In Section 2.2, we explain our numerical method, including the double-node formulation to allow jumps in the finite elements solution on the compartment interfaces, the transformation of the PDE to replace pseudo-periodic by standard periodic boundary conditions, the decoupling of the real and imaginary parts, as well as the coupling of the finite elements discretization to the RKC time integration method. In Section 2.3 we briefly describe the implementation of the proposed method on the FEniCS C++ platform as well as the use of the mesh generator Salome. In Section 2.4, we show accuracy and timing results for this method. Section 2.5 contains our conclusions.

2.2 Method

In this section we describe our method to solve the Bloch-Torrey PDE (1.23, 1.24, 1.25, 1.27, 1.28, 1.29) and the steady-state Laplace PDEs (1.31, 1.24, 1.25, 1.32, 1.33).

The standard Galerkin formulation for the Bloch-Torrey PDE in the weak form is

$$\frac{\partial}{\partial t}\int\limits_{\Omega^l} M\, v\, d\mathbf{r} = -\, I\gamma f(t)\int\limits_{\Omega^l} \mathcal{G}Mv d\mathbf{r} - \int\limits_{\Omega^l} \mathbf{D}\nabla M\cdot\nabla v d\mathbf{r} + \int\limits_{\partial\Omega^l\cap\Gamma} \mathbf{D}\nabla M\cdot\mathbf{n}^l v\, ds + \int\limits_{\partial\Omega^l\cap\partial C} \mathbf{D}\nabla M\cdot\mathbf{n}^l v\, ds, \tag{2.1}$$

for each compartment Ω^l, where $\mathbf{n}^l$ is the outward pointing normal and v is a test function. We separated the two surface integrals into one involving the interface conditions and the other involving the boundary conditions. Similarly, the weak form for the steady-state Laplace PDE is

$$\int\limits_{\Omega^l}\mathbf{D}\nabla W\cdot\nabla v\, d\mathbf{r} - \int\limits_{\partial\Omega^l\cap\Gamma}\mathbf{D}\,\nabla W\cdot\mathbf{n}^l\, v\, ds - \int\limits_{\partial\Omega^l\cap\partial C}\mathbf{D}\,\nabla W\cdot\mathbf{n}^l\, v\, ds = 0. \tag{2.2}$$

We will use linear elements and write our code using the finite elements platform FEniCS [43].

There are some numerical issues in the spatial discretization that will be addressed in this section. They concern several non-standard aspects of these two PDEs that require special handling when using a general finite elements platform like FEniCS.

2.2.1 Interface conditions: allowing jumps in the finite elements solution

Standard finite elements discretization enforces that the solution is continuous across elements. Discontinuous Galerkin discretization allows the solution to be

fully discontinuous across all the elements [43]. In our case, the solution is continuous in each compartment Ω^l, and possibly discontinuous on the compartment interfaces $\Gamma = \cup\Gamma^{ln}$. For this reason, the discontinuous Galerkin discretization that would double the nodes on the edges of all the elements, is not efficient and we do not use it. Instead, we keep the finite elements formulation in order to use the matrix assembly routines in FEniCS. To do so, we need to find a way to incorporate jumps in the solution on the interface Γ while still keeping the solution 'continuous', at least formally.

To achieve this goal, we looped through the finite elements mesh and repeated nodes that lie on the interfaces Γ and created elements of zero volume there. We call these additional elements *interface elements*: an element consists of d distinct vertices, each repeated once. Standard linear finite elements are triangles in 2D and tetrahedrons in 3D. Interface elements are "fake" elements that are segments in 2D and triangles in 3D. In this way, the solution is formally continuous across the interface elements, but it is physically discontinuous because the interface elements have zero volume. We will then associate a local stiffness matrix to the interface elements even though this stiffness matrix represents a surface integral and not a volume integral.

We explain this discretization in detail for the steady-state Laplace PDE in Eq. (2.2). We write the solution as $W(\mathbf{r}) = \sum_{i=1}^{N} \xi_i \varphi_i(\mathbf{r})$, where $\varphi_i(\mathbf{r})$ is the linear basis function that is equal to 1 at the ith vertex, $\mathbf{v}_i$, zero at all other vertices, and whose support lies in the elements containing $\mathbf{v}_i$; N is the total number of nodes in a discretized mesh of C. We consider a standard (non-interface) element $E_i \in \Omega^l$ containing the vertices $\{\mathbf{v}_k\}$, with

$$W(\mathbf{r}) = \sum_{\{k, \mathbf{v}_k \in \overline{E_i}\}} \xi_k \varphi_k(\mathbf{r}), \quad \mathbf{r} \in E_i.$$

We set $v = \varphi_j$ and consider the quantity

$$\begin{aligned} &\int_{E_i} \mathbf{D}\nabla W \cdot \nabla \varphi_j \, d\mathbf{r} - \int_{\partial E_i \cap \Gamma} \mathbf{D}\, \nabla W \cdot \mathbf{n}^i \, \varphi_j \, ds \\ &= \sum_{\{k, \mathbf{v}_k \in \overline{E_i}\}} \xi_k \left(\int_{E_i} \mathbf{D}\nabla \varphi_k \cdot \nabla \varphi_j \, d\mathbf{r} \right) - \int_{\partial E_i \cap \Gamma} \mathbf{D}\nabla W \cdot \mathbf{n}^i \, \varphi_j \, ds, \end{aligned} \tag{2.3}$$

for j where $\mathbf{v}_j \in \overline{E_i}$. (For other j, this quantity is zero.) The stiffness matrix associated with the element E_i is the first term on the right hand side and that has entries

$$S_{jk} = \int_{E_i} \mathbf{D}\nabla \varphi_k \cdot \nabla \varphi_j \, d\mathbf{r}. \tag{2.4}$$

The second term on the right hand side,

$$- \int_{\partial E_i \cap \Gamma} \left(\mathbf{D}\nabla W \cdot \mathbf{n}^i \right) \varphi_j \, ds, \tag{2.5}$$

is zero if $\{\mathbf{v}_j\} \notin \partial E_i \cap \Gamma$. So for this term, we only need to consider an E_i that touches a compartment interface Γ^{ln} and only the vertices of E_i that lie on Γ^{ln}. To be specific, we choose $E_i \in \Omega^l$ and restrict j to those $j \in \{k^l\}$ where $\{\mathbf{v}_{k^l}\}$ is the set of vertices that belong to $\partial E_i \cap \Gamma^{ln}$. Because we have doubled nodes on Γ, as described earlier, we know these same vertices are repeated, and let the repeated nodes be $\{\mathbf{v}_{k^n}\}$ and belong to the element $E_{i'} \in \Omega^n$. To compute the above surface integral, we need the flux $D\nabla W \cdot \mathbf{n}^i$ on $\partial E_i \cap \Gamma$. This flux can be related to $\{\{\xi_{k^l}\}, \{\xi_{k^n}\}\}$, the solution values on the repeated vertices, because the flux is related to the jump in the solution due to the interface conditions in Eqs. (1.24,1.25). We can repeat the same argument for the element $E_{i'}$ on the other side of Γ^{ln} to obtain the needed quantities associated with $j \in \{k^n\}$.

Now we collect the terms associated with Eq. (2.5) for the two elements E_i and $E_{i'}$ in local order

$$\mathbf{S}^{loc}\xi_{\{k^l,k^n\}}. \tag{2.6}$$

In 2D and 3D, the local matrices for interface elements with linear basis functions are:

$$\mathbf{S}^{loc} = \frac{\kappa\, C_k}{6}\begin{bmatrix} 2 & 1 & -1 & -2 \\ 1 & 2 & -2 & -1 \\ -1 & -2 & 2 & 1 \\ -2 & -1 & 1 & 2 \end{bmatrix}$$

and

$$\mathbf{S}^{loc} = \frac{\kappa\, C_k}{12}\begin{bmatrix} 2 & 1 & 1 & -1 & -1 & -2 \\ 1 & 2 & 1 & -1 & -2 & -1 \\ 1 & 1 & 2 & -2 & -1 & -1 \\ -1 & -1 & -2 & 2 & 1 & 1 \\ -1 & -2 & -1 & 1 & 2 & 1 \\ -2 & -1 & -1 & 1 & 1 & 2 \end{bmatrix}, \tag{2.7}$$

respectively, where c_k is the length of the interface segment in 2D and the area of the interface triangle in 3D.

For the ease of the global assembly routines, the $\mathbf{S}^{loc}$ matrix will be associated to the interface element defined by the repeated vertices $\mathbf{v}_{\{k^l,k^n\}}$. For all standard (non-interface) elements, the stiffness matrix is the usual one in Eq. (2.4).

2.2.2 Boundary conditions: transformation of the Bloch-Torrey PDE

The pseudo-periodic boundary conditions for the Bloch-Torrey PDE in Eqs. (1.27,1.28) and the steady-state Laplace PDE in Eqs. (1.32,1.33) differ slightly from standard periodic boundary conditions. In addition, the boundary conditions for the Bloch-Torrey PDE involve complex numbers and are time-dependent. We limit our discussion to the Bloch-Torrey PDE because it is the more complicated case.

We assume the mesh of C is generated in such a way that the nodes are mirror reflected on the opposite faces of C. Let $\{E^k\}$ be the elements that touch ∂C. They

give rise to the non-zero entry $\int\limits_{\partial E^k \cap \partial C} \mathbf{D}\,\nabla M \cdot \mathbf{n}\, v\, ds$. Since $\nabla M \cdot \mathbf{n}$ is unknown on ∂C, this quantity has to be eliminated by using the pseudo-periodic relation (1.28) on the normal derivative. For example, in the x-direction, this means replacing the rows of the global finite elements matrices associated to the face of C, $r_1 = b_1$, by new rows that are obtained by multiplying the original rows by $e^{I\theta_1(t)}$ and subtracting them from the rows associated to the opposite face, $r_1 = a_1$. Then one replaces the rows associated to the face, $r_1 = a_1$, by the pseudo-periodic relation on the function value in Eq. (1.27).

This naive way of implementing pseudo-periodic boundary conditions introduces complex arithmetic and time dependence into the global finite elements matrices. This is a very undesired characteristic for the mass matrix, since many linear systems involving the mass matrix have to be solved repeatedly.

If we could change the pseudo-periodic boundary conditions to standard periodic boundary conditions, then we can keep the mass matrix real-valued and time-independent. Thus, similarly to [58], we chose to transform the magnetization to a new unknown $m(\mathbf{r}, t)$:

$$m(\mathbf{r}, t) = M(\mathbf{r}, t)\, e^{I\,\gamma\,\mathcal{G}(\mathbf{r})\,\mathcal{F}(t)}, \quad \mathcal{F}(t) = \int_0^t f(s)\, ds.$$

The Bloch-Torrey PDE (1.23) is then transformed to

$$\frac{\partial}{\partial t} m = -I\,\gamma\,\mathcal{F}\Big(\nabla\mathcal{G}\cdot\mathbf{D}\nabla m + \nabla m\cdot\mathbf{D}\nabla\mathcal{G}\Big) - \nabla\mathcal{G}\cdot\mathbf{D}\nabla\mathcal{G}\, m\Big(\gamma\,\mathcal{F}\Big)^2 + \nabla\cdot\Big(\mathbf{D}\nabla m\Big), \quad \mathbf{r} \in \cup\Omega^l, \tag{2.8}$$

with periodic boundary conditions

$$\begin{aligned} m(\mathbf{r}, t)\Big|_{r_k = -L/2} &= m(\mathbf{r}, t)\Big|_{r_k = L/2}, \quad k = 1, \cdots, d, \\ \frac{\partial}{\partial r_k} m(\mathbf{r}, t)\Big|_{r_k = -L/2} &= \frac{\partial}{\partial r_k} m(\mathbf{r}, t)\Big|_{r_k = L/2}, \quad k = 1, \cdots, d. \end{aligned} \tag{2.9}$$

The interface conditions (1.24, 1.25) are changed to

$$\begin{aligned} \mathbf{D}^n \nabla m^n \cdot \mathbf{n}^n &= \kappa^{ln}\Big(m^l - m^n\Big) + I\,\gamma\, m^n \mathcal{F}\, \mathbf{D}^n \nabla\mathcal{G}\cdot\mathbf{n}^n, \quad \forall\, l, n, \\ \mathbf{D}^l \nabla m^l \cdot \mathbf{n}^l &= \kappa^{ln}\Big(m^n - m^l\Big) + I\,\gamma\, m^l \mathcal{F}\, \mathbf{D}^l \nabla\mathcal{G}\cdot\mathbf{n}^l, \quad \forall\, l, n, \end{aligned} \tag{2.10}$$

where m^l, m^n are the limiting values of $m(\mathbf{r}, t)$ in Ω^l and Ω^n. We note that Eq. (2.8) and Eq. (2.10) are more complicated than those used in [58] because we kept all the first order terms in order to obtain second order accuracy in space.

The weak form of Eq. (2.8) is then

$$\frac{\partial}{\partial t}\int\limits_{\Omega^l} m\,v\,d\mathbf{r} = -\,I\,\gamma\,\mathcal{F}\int\limits_{\Omega^l}\Big(\nabla\mathcal{G}\cdot\mathbf{D}\nabla m+\nabla m\cdot\mathbf{D}\nabla\mathcal{G}\Big)\,v\,d\mathbf{r}-\nabla\mathcal{G}\cdot\mathbf{D}\nabla\mathcal{G}\left(\gamma\,\mathcal{F}\right)^2\int\limits_{\Omega^l} m\,v\,d\mathbf{r} - \int\limits_{\Omega^l}\mathbf{D}\nabla m\cdot\nabla v d\mathbf{r}+\int\limits_{\partial\Omega^l\cap\Gamma}\mathbf{D}\nabla m\cdot\mathbf{n}^l v\,ds+\int\limits_{\partial\Omega^l\cap\partial C}\mathbf{D}\nabla m\cdot\mathbf{n}^l v\,ds. \tag{2.11}$$

Ignoring the boundary and interface conditions, the weak form (2.11) can be rewritten in matrix form:

$$\mathbf{M}\frac{\partial}{\partial t}\xi = -I\,\mathbf{J}\,\xi-\mathbf{K}\,\xi-\mathbf{S}\,\xi, \tag{2.12}$$

where $\mathbf{M}$ and $\mathbf{S}$ are the mass matrix and stiffness matrix, respectively, and

$$\mathbf{J}=\gamma\,\mathcal{F}\int\limits_{\Omega}\Big(\nabla\mathcal{G}\cdot\mathbf{D}\nabla\varphi^T+\nabla\varphi^T\cdot\mathbf{D}\nabla\mathcal{G}\Big)\,\varphi\,d\mathbf{r},$$

$$\mathbf{K}=\left(\gamma\,\mathcal{F}\right)^2\int\limits_{\Omega}\nabla\mathcal{G}\cdot\mathbf{D}\,\nabla\mathcal{G}\,\varphi^T\varphi\,d\mathbf{r},$$

where $\varphi=[\varphi_j]_{j=1..N}$ is the column vector of basis functions.

In particular, we compute the flux term which is now complex-valued and time-dependent,

$$\int\limits_{\partial E_i\cap\Gamma}\Big(\mathbf{D}\nabla m\cdot\mathbf{n}^i\Big)\,\varphi\,ds=\Big(\mathbf{S}^{loc}+I\,\mathbf{J}^{loc}\Big)\,\xi_{\{k^l,k^n\}}, \tag{2.13}$$

where

$$\mathbf{J}^{loc}=\frac{\gamma\,\mathcal{F}\,C_k\,D\nabla\mathcal{G}\cdot\mathbf{n}^i}{6}\begin{bmatrix}2&1&0&0\\1&2&0&0\\0&0&2&1\\0&0&1&2\end{bmatrix}\quad(2D),$$

and

$$\mathbf{J}^{loc}=\frac{\gamma\,\mathcal{F}\,C_k\,D\nabla\mathcal{G}\cdot\mathbf{n}^i}{12}\begin{bmatrix}2&1&1&0&0&0\\1&2&1&0&0&0\\1&1&2&0&0&0\\0&0&0&2&1&1\\0&0&0&1&2&1\\0&0&0&1&1&2\end{bmatrix}\quad(3D).$$

The matrices of the flux term $\mathbf{J}^{loc}$ and $\mathbf{S}^{loc}$ need to be assembled into the matrix $\mathbf{J}$ and the stiffness matrix $\mathbf{S}$. The periodic boundary conditions will be applied to the remaining term in Eq. (2.11), namely $\int\limits_{\partial\Omega^l\cap\partial C}\mathbf{D}\nabla m\cdot\mathbf{n}^l v\,ds$.

After applying the interface and boundary conditions to Eq. (2.12), we obtain

$$\widetilde{\mathbf{M}}\,\frac{\partial}{\partial t}\xi=-I\,\widetilde{\mathbf{J}}\,\xi-\widetilde{\mathbf{K}}\,\xi-\widetilde{\mathbf{S}}\,\xi. \tag{2.14}$$

This matrix equation will be solved to get $\frac{\partial}{\partial t}\xi$, which will be the input of an explicit time-stepping method described in the next section. We can see that the left-hand side contains the mass matrix, while the complex-valued terms are all on the right-hand side. The fact that the mass matrix is real-valued allows one to replace one linear system (2.14) of size $2N \times 2N$ by two linear systems of size $N \times N$:

$$\begin{aligned} \widetilde{\mathbf{M}}\,\frac{\partial}{\partial t}\xi^R &= \widetilde{\mathbf{J}}\,\xi^I - \widetilde{\mathbf{K}}\,\xi^R - \widetilde{\mathbf{S}}\,\xi^R, \\ \widetilde{\mathbf{M}}\,\frac{\partial}{\partial t}\xi^I &= -I\,\widetilde{\mathbf{J}}\,\xi^R - \widetilde{\mathbf{K}}\,\xi^I - \widetilde{\mathbf{S}}\,\xi^I, \end{aligned} \tag{2.15}$$

where ξ^R and ξ^I are the real and imaginary parts of ξ, $\xi = \xi^R + I\,\xi^I$. Moreover, because the mass matrix is time-independent, it needs only to be assembled once, and not at each time step. If Eq. (2.15) is solved directly, $\widetilde{\mathbf{M}}$ will only need to be inverted once. Besides the numerical advantage related to having a real-valued and time-independent mass matrix, this transformation also results in a less oscillatory unknown function $m(\mathbf{r}, t)$ than the original magnetization $M(\mathbf{r}, t)$, and hence, coarser discretizations can be used [58]. Note that m is identical to M at the initial time ($t = 0$) and at the final time $t = TE$ since both $\mathcal{F}(0)$ and $\mathcal{F}(TE)$ vanish.

2.2.3 When the cell interface touches the computational boundary

Because the computational domain C is extended periodically, in some cases the cell interfaces touch ∂C. In this case, the combination of the interface condition and periodic boundary condition is necessary. As a simple example, we consider a computational domain C in which a cell is placed touching $x = a$ (Fig. 2.1). The boundary needs to be periodic at $x = a$ and $x = b$. The cell interior is characterized by a diffusion tensor $\mathbf{D}^c$. The extra-cellular space is the remaining part and characterized by a diffusion tensor $\mathbf{D}^e$. The cell touches the boundary at the interface Σ, which is the intersection between the cell boundary and ∂C.

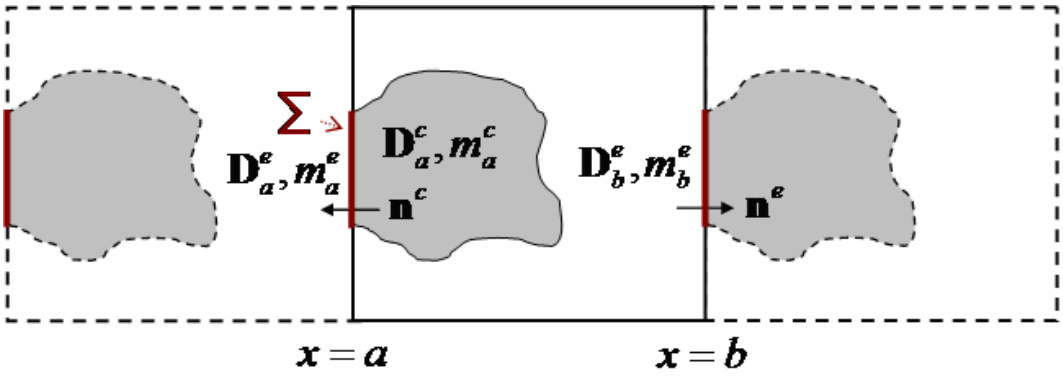

Figure 2.1: When the interface touches ∂C, the interface conditions and periodic boundary conditions are combined.

For the time-dependent Bloch-Torrey PDE, the interface conditions at Σ are

$$\begin{aligned}\mathbf{D}_a^c\nabla m_a^c\cdot\mathbf{n}^c =&\kappa(m_a^e-m_a^c)+I\,\gamma\,m_a^c\mathcal{F}\,\mathbf{D}_a^c\nabla\mathcal{G}\cdot\mathbf{n}^c,\\ \mathbf{D}_a^e\nabla m_a^e\cdot\mathbf{n}^e =&\kappa(m_a^c-m_a^e)+I\,\gamma\,m_a^e\mathcal{F}\,\mathbf{D}_a^e\nabla\mathcal{G}\cdot\mathbf{n}^e,\end{aligned}\tag{2.16}$$

and the periodic boundary conditions are

$$\begin{aligned}m_a^e &= m_b^e,\\ \mathbf{D}_a^e\nabla m_a^e\cdot\mathbf{n}^c &= -\mathbf{D}_b^e\nabla m_b^e\cdot\mathbf{n}^e.\end{aligned}\tag{2.17}$$

Now, we combine Eqs. (2.16, 2.17) to get

$$\begin{aligned}\mathbf{D}_a^c\nabla m_a^c\cdot\mathbf{n}^c =&\kappa(m_b^e-m_a^c)+I\,\gamma\,m_a^c\mathcal{F}\,\mathbf{D}_a^c\nabla\mathcal{G}\cdot\mathbf{n}^c,\\ \mathbf{D}_a^e\nabla m_b^e\cdot\mathbf{n}^e =&\kappa(m_a^c-m_b^e)+I\,\gamma\,m_b^e\mathcal{F}\,\mathbf{D}_b^e\nabla\mathcal{G}\cdot\mathbf{n}^e.\end{aligned}\tag{2.18}$$

Similarly, for steady-state Laplace PDE, the combined conditions are

$$\begin{aligned}\mathbf{D}_a^c\nabla W_a^c\cdot\mathbf{n}^c =&\kappa(W_b^e-M_a^c)-\kappa(b-a),\\ \mathbf{D}_b^e\nabla W_b^e\cdot\mathbf{n}^e =&\kappa(W_a^c-W_b^e)+\kappa(b-a).\end{aligned}\tag{2.19}$$

2.2.4 Time stepping for the Bloch-Torrey PDE using explicit RKC

We solve the system of ODEs in Eq. (2.15) using the Runge-Kutta-Chebyshev (RKC) method [63]. We briefly describe this method as it applies to solving ODEs of the form:

$$\frac{d\{\xi_{ijk}(t)\}}{dt}=F(t,\{\xi_{ijk}(t)\}).$$

Getting $\frac{\partial}{\partial t}\xi(t)$ at a given time from Eq. (2.15) requires solving two linear systems with the same mass matrix $\widetilde{\mathbf{M}}$. To go from $\{\xi_{ijk}\}^n\approx\{\xi_{ijk}(t^n)\}$ to $\{\xi_{ijk}\}^{n+1}\approx\{\xi_{ijk}(t^{n+1})\}$, the following s stages are taken as

$$\begin{aligned}Y^0 &= \{\xi_{ijk}\}^n,\\ Y^1 &= Y^0+\mu^1\tau F(t^n,\{\xi_{ijk}\}^n),\\ Y^j &= \mu^jY^{j-1}+\nu^jY^{j-2}+(1-\mu^j-\nu^j)Y^0+\tilde{\mu}\,\tau F(t^n+c^{j-1}\tau,Y^{j-1})\\ &\quad+\tilde{\gamma}\,\tau F(t^n,Y^0),\quad 2\le j\le s,\\ \{\xi_{ijk}\}^{n+1} &= Y^s,\end{aligned}$$

where $\tau=(t^{n+1}-t^n)$, and the coefficients are determined by Chebyshev polynomials.

Note that the local time error of the RKC method at t^{n+1} can be estimated as

$$err^{n+1}=\frac{1}{15}\Big(12(\{\xi_{ijk}\}^n-\{\xi_{ijk}\}^{n+1})+6\tau\left(F(t^n,\{\xi_{ijk}\}^n)+F(t^{n+1},\{\xi_{ijk}\}^{n+1})\right)\Big),$$

and the time step can be made stable no matter how large it is by increasing the number of stages s. Specifically, the stability criterion is [63]

$$(t^{n+1}-t^n)_{RKC}\le\Delta t_{RKC}^{max}:=\frac{0.653s^2}{\max eig(Jac\,F(t,\{\xi_{ijk}\}(t)))}\approx 0.653\;s^2\frac{h^2}{6\,D}.\tag{2.20}$$

Essentially, the RKC method chooses a t^{n+1} where the error term above is smaller than the user-specified tolerance and the number of stages s is increased to ensure that $t^{n+1} - t^n$ is a stable step. Because the time step can be enlarged as $O(s^2)$ whereas the computational time only increases as $O(s)$, this means that the RKC method with larger time steps computes the solution faster than taking many smaller steps of the Forward Euler method. The number of stages s is typically 30-50 in our simulations. In addition, because of the existence of a three-term recurrence relation for Chebyshev polynomials, the storage requirement does not increase with s, it stays constant being 5 times the number of unknowns.

In contrast, for the Forward Euler method, the stability criterion for a spatial discretization h is

$$\left(t^{n+1} - t^n\right)_{FE} \leq \Delta t_{FE}^{max} := \frac{h^2}{6\,D}. \tag{2.21}$$

For moderate accuracy requirements, it is usually much more efficient to increase s according to Eq. (2.20) to get a time step that is appropriate for the desired accuracy than being limited by the stability condition (2.21). The RKC method has essentially the second order time convergence [63].

2.3 Implementation on FEniCS Finite Elements platform and mesh generator Salome

We call the method that we described in the previous section the FEM-RKC method. This method was implemented on the C++ version of FEniCS 1.0.0. For this purpose, we had to take the following steps.

Because the RKC solver was only available in Fortran, we rewrote it in C++. To define the computational domain, we need two files: a mesh file and a compartment marker file. Currently, we use Salome 6.6.0 to generate meshes. It gives a flexible way to generate complex geometries with multiple compartments and periodic boundaries. We wrote a C++ subroutine to convert a Salome format '.unv' to FEniCS format '.xml' and a subroutine to create the compartment marker file compatible with the 'CellFunction' of FEniCS.

We then wrote a subroutine to split the mesh and add double nodes beyond the FEniCS library. Matrices and vectors for standard elements are automatically assembled by FEniCS supplied routines. We enforced the interface conditions by using subroutines that we wrote beyond the FEniCS library. For a two-compartment model the use of a 1-1 mapping between vertices at the interfaces is enough because there is no more than two compartments coming together at one point. However, when the computational domains include more than two compartments, there are some singular points where more than two compartments come together and the vertex mapping fails. To effectively manage multi-compartment domains, we had to generate a 1-1 mapping between facets at the interfaces instead. Based on the fact that two elements have no more than two facets, this mapping works for general cases.

Various linear solvers are available in FEniCS platform but we mainly use two. For problems with a few thousand unknowns, a direct solver with the sparse LU decomposition of $\widetilde{\mathbf{M}}$ was used because the factorization can be reused after the first iteration. For larger problems, this decomposition becomes slow and memory demanding, and we use the iterative method GMRES. Unless specified differently, the absolute tolerance 10^{-12} and relative tolerance 10^{-10} were set for GMRES.

All simulations were performed on a Lenovo workstation (Intel(R) Xeon(R) CPU X3430@2.40GB), running the program as a serial code on Linux Ubuntu 10.04 LTS.

2.4 Numerical results

In this section we present numerical results on the accuracy and timing of the FEM-RKC method.

Let $\varepsilon(\mathbf{r},t) = M_h(\mathbf{r},t) - M(\mathbf{r},t)$ be the difference between the computed magnetization $M_h(\mathbf{r},t)$ obtained on a mesh with maximum elements size h and the exact solution $M(\mathbf{r},t)$. We will measure the spatial discretization error in three standard norms:

1. The L^2 error: $\|\varepsilon(\mathbf{r},t)\|_{L^2} = \left(\int_\Omega |\varepsilon(\mathbf{r},t)|^2 d\mathbf{r}\right)^{\frac{1}{2}}$;
2. The H^1 error: $\|\varepsilon(\mathbf{r},t)\|_{H^1} = \left(\int_\Omega |\nabla\varepsilon(\mathbf{r},t)|^2 d\mathbf{r}\right)^{\frac{1}{2}}$;
3. The L^∞ error: $\|\varepsilon(\mathbf{r},t)\|_{L^\infty} = \max_{\mathbf{x}\in\Omega} |\varepsilon(\mathbf{x},t)|$.

Additionally, for the application to dMRI, since the dMRI signal is the integral of the magnetization at $t = TE$, we define the dMRI signal error:

4. The signal error: $\|\varepsilon(\mathbf{r},t)\|_S = \left|\int_\Omega \varepsilon(\mathbf{r},t) d\mathbf{r}\right|$.

Strictly speaking, the dMRI signal is experimentally measured only at $t = TE$, but we will show the convergence of the integral of M at $t < TE$ as well.

The FEM-RKC method will be compared to two other methods:

1. the FEM-BE method, coupling the same finite elements discretization described in the previous section to Backward Euler time stepping.
2. the FVM-RKC method [41], coupling a uniform Cartesian finite volume spatial discretization with RKC time-stepping.

2.4.1 Local stiffness matrix for the interface jump condition

First we check the accuracy of the local stiffness matrix at the interface for a 2D problem. On the computational domain $\Omega = [0,40] \times [0,10]$ with the interface

$r_2 = r_1/4$ (Fig. 2.2a), a solution of the Laplace equation is

$$u(\mathbf{r}) = \begin{cases} a\,r_1 + b\,r_2 + c_1 & \text{if } (r_1, r_2) \in \Omega^+, \\ a\,r_1 + b\,r_2 + c_2 & \text{if } (r_1, r_2) \in \Omega^-. \end{cases} \tag{2.22}$$

For a given intrinsic diffusion coefficient D, we can compute the permeability,

$$\kappa = \frac{D\,(a - 4\,b)}{(c_2 - c_1)\sqrt{17}}, \tag{2.23}$$

that satisfies the interface conditions (1.24,1.25). For $a = 40$, $b = 3$, $c_1 = 0$ and $c_2 = 1000$ and $D = 3 \cdot 10^{-3}\text{mm}^2/\text{s}$, we obtain $\kappa = 2.04 \cdot 10^{-5}\frac{\text{m}}{\text{s}}$ and the values of $u(\mathbf{r})$ at the exterior boundaries. The values of $u(\mathbf{r})$ at the exterior boundaries are set as Dirichlet BC and the interface conditions (1.24,1.25) with permeability κ are enforced to obtain a numerical solution. We found that the numerical solution that we obtained is accurate to within 10^{-16} of the theoretical solution at all vertices. The theoretical solution is plotted in Fig. 2.2b.

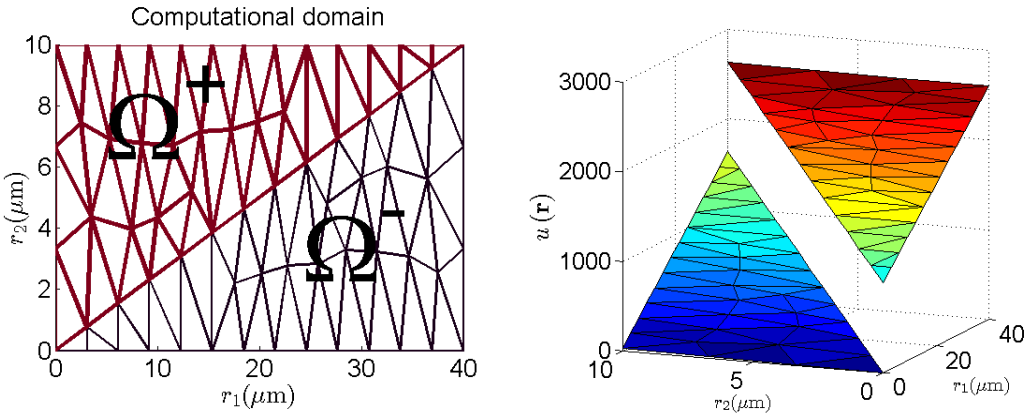

(a) (b)

Figure 2.2: The computational domain with the interface $r_2 = r_1/4$ (2.2a) and exact solution Eq. (2.22) of the Laplace equation with $a = 40$, $b = 3$, $c_1 = 0$ and $c_2 = 1000$, $D = 3{\cdot}10^{-3}\text{mm}^2/\text{s}$ (2.2b). The permeability at the interface is computed by Eq. (2.23) so that the interface conditions (1.24,1.25) are satisfied.

Second, we consider another problem related to the periodic BCs and the interface conditions. Over a box $[-L/2, L/2]^d$ $(L > 0)$ with the interface $r_1 = 0$, we construct a function:

$$u(\mathbf{r}) = \begin{cases} \dfrac{\kappa\,L\,r_1}{\kappa\,L + D} - \dfrac{LD}{\kappa\,L + D}, & \text{if } r_1 \le 0, \\ \dfrac{\kappa\,L\,r_1}{\kappa\,L + D}, & \text{if } r_1 \ge 0. \end{cases}$$

One can see that this function satisfies the Laplace equation (1.31) with the interface conditions (1.24,1.25) and boundary conditions (1.32) where $\mathbf{g} = \vec{e}_1$. We solved Eq.

(1.31) in both 2D and 3D using the FEM-RKC method and recovered the solution to 10^{-16}. Moreover, the analytical effective diffusion coefficient $D_{11}^{\text{eff}} = \dfrac{\kappa L}{\kappa L + D}$ [79] was also obtained to an absolute accuracy of 10^{-16}. This is an agreement between the effective diffusion coefficient computed by homogenization theory and the analytical long-time apparent diffusion coefficient for the 1D interface problem on a periodic domain.

2.4.2 Different positions of computational domain in periodic structures

The pseudo-periodic boundary conditions (1.28) allow us to mimic diffusion in an infinite domain where the computational domain, C, is infinitely repeated in all three coordinate directions. So, the signals should be identical for some positions of the computational domain providing that from those positions, the infinitely extended domain of C for all three directions are the same.

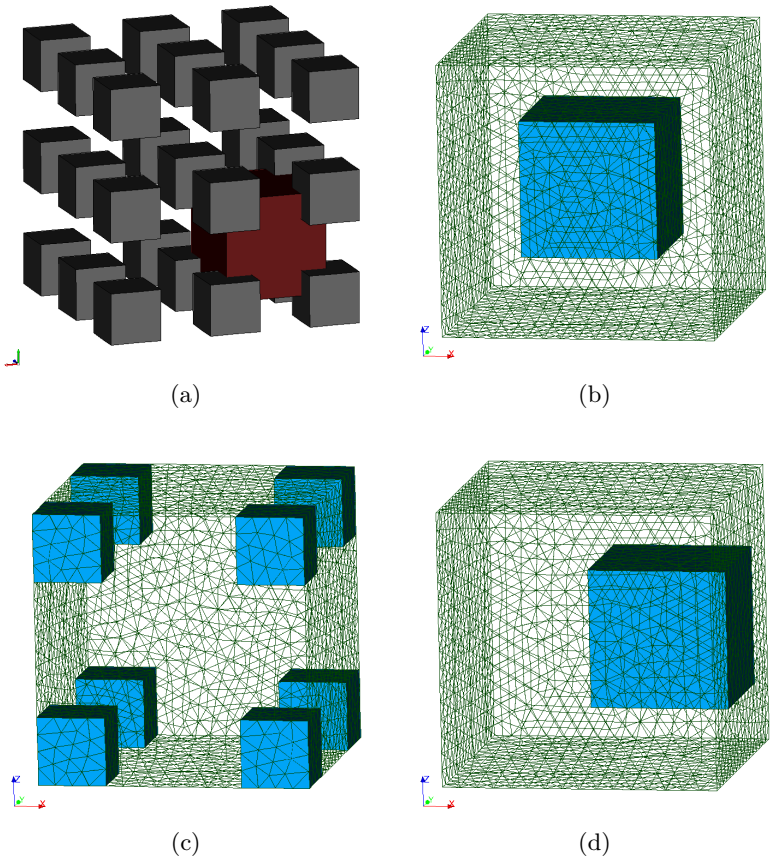

(a) (b)

(c) (d)

Figure 2.3: A computational domain with different positions in a geometrical structure (2.3a) such that it contains a cell (2.3b), cuts cells (2.3c) and touches a cell (2.3d).

The simulations in this section are used to numerically check the effect of the pseudo-peridic boundary conditions (1.28) as well as Eq. (2.18) where the pseudo-periodic boundary conditions are combined with the interface conditions for cells touching the exterior boundaries. We consider different positions of a computational domain $[-2\mu\text{m}, 2\mu\text{m}]^3$ in a model biological structure in which square cells of length $L = 2\mu$m are periodically placed (Fig. 2.3a) such that it contains a cell (Fig. 2.3b), cuts cells (Fig. 2.3c) and touches a cell (Fig. 2.3d).

In theory, the signals on these three domains are identical. We perform three simulations on these three domains for the same parameters $\Delta = \delta = 10$ms, $\kappa = 10^{-5}$m/s and diffusion coefficient $D^c = D^e = 10^{-3}\text{mm}^2/\text{s}$. The relative difference between simulated DMRI signals obtained by solving the Bloch-Torrey PDE on three domains is less than 1% (Fig. 2.4b) for all seven $b-$values from 0 to 3000s/mm^2.

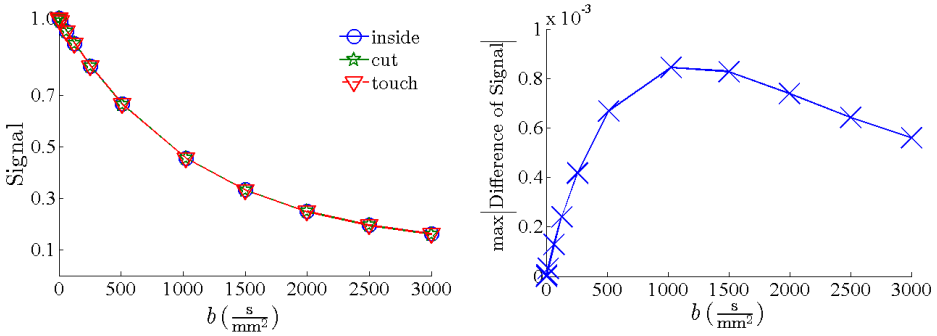

(a) (b)

Figure 2.4: The DMRI signals on three domains are close to each other (2.4a), the relative difference is less than 1% (2.4b).

2.4.3 Spatial discretization

Similar to standard FEM, FEM-RKC with linear basis functions is expected to have the second order convergence in the L^2-norm and the $L^\infty-$norm, and the first order in the H^1-norm.

2.4.3.1 Homogeneous problem

First we consider a homogeneous domain $C = [-5\mu\text{m}, 5\mu\text{m}]^2$, the initial condition is a Dirac delta distribution at $\mathbf{r}_0 = (0, 0)$. The constant diffusion coefficient is $D = 3 \cdot 10^{-3}\text{mm}^2/\text{s}$, $\|\mathbf{g}\| = 373.8\frac{\text{mT}}{\text{m}}$, and the time profile is PGSE with $\delta = 4$ms and $\Delta = 4$ms.
The mesh size was varied from 20×20 to 640×640 vertices for FVM-RKC and from 10×10 to 100×100 vertices for FEM-RKC. The results at $t = 2$ms are shown in Fig. 2.5a, 2.5b, 2.5c. One can see the second order convergence in the L^2-norm

and $L^\infty-$norm, and the first order convergence in the H^1-norm, as expected for FEM-RKC. For FVM-RKC, the convergence is first order in the L^2-norm and the $L^\infty-$norm. The H^1-norm is not defined. Then we study the convergence of the integral of magnetization M. For a homogeneous domain, the mass conservation in both the FEM and FVM methods implies that the integral of M is exact up to numerical accuracy when $\mathcal{F}(t)$ is zero. So we just verify the spatial convergence of the integral of M at $t = \delta$, $\delta < t < \Delta$, and $\delta < t < \Delta + \delta$. Figure 2.5d shows that the integral of M has the second order convergence in space.

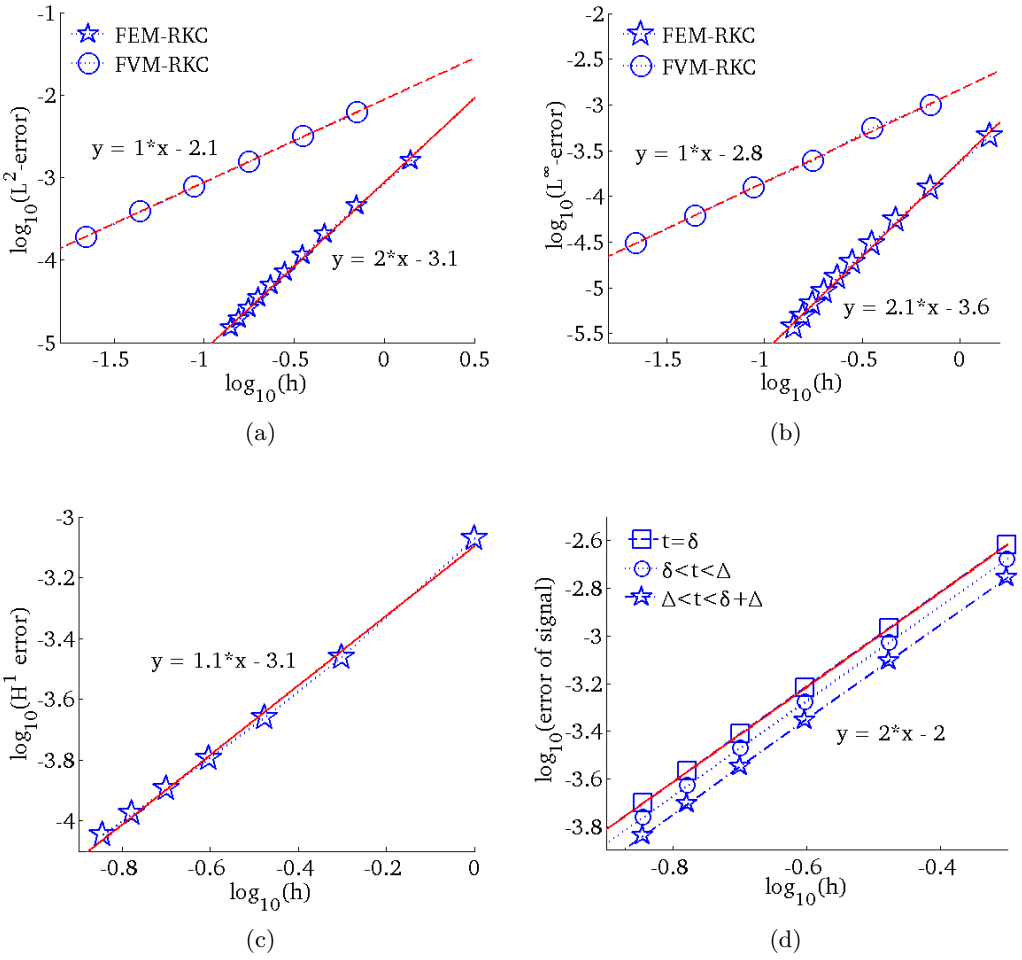

Figure 2.5: Two-dimensional homogeneous problem on $C = [-5\mu\text{m}, 5\mu\text{m}]^2$. The L_2-error (2.5a), L_∞-error (2.5b) and signal error (2.5d) are of second order in h for FEM-RKC and of first order for FVM-RKC; FEM-RKC also gives the first order convergence in H^1-error (2.5c).

The results are similar in 3D. We solve the homogeneous problem on $[-5\mu\text{m}; 5\mu\text{m}]^3$ for the PGSE sequence: $\Delta = \delta = 4\text{ms}$, $D = 3{\cdot}10^{-3}\text{mm}^2/\text{s}$ and $\|\mathbf{g}\| = 373.8\frac{\text{mT}}{\text{m}}$. Fig-

ure 2.6 illustrates the second order convergence in the L^2-norm and the $L^\infty-$norm of FEM-RKC.

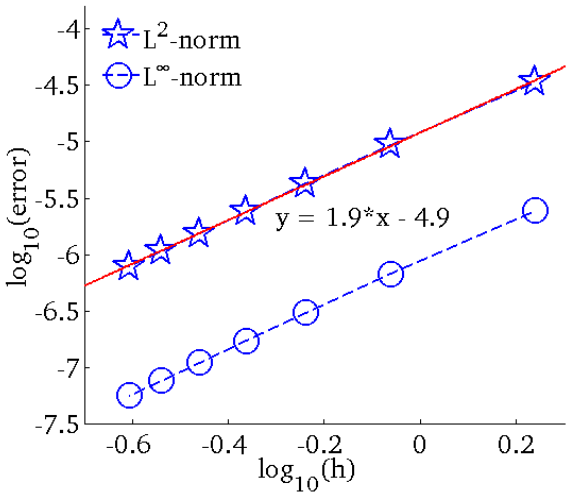

Figure 2.6: Spatial convergence of L^2-error and L^∞-error for a three-dimensional homogeneous problem on $C = [-5\mu\text{m}, 5\mu\text{m}]^3$ with PGSE sequence: $\Delta = \delta = 4\text{ms}$, $D = 3 \cdot 10^{-3}\text{mm}^2/\text{s}$ and $\|\mathbf{g}\| = 373.8\frac{\text{mT}}{\text{m}}$ for FEM-RKC.

2.4.3.2 Impermeable disk and sphere

We consider the convergence of the dMRI signal (integral of the magnetization at echo time $t = TE$) inside impermeable circular and spherical cells for the OGSE sequence. Analytical solution for comparison was obtained using the matrix formalism approach [21]. The simulations are performed for both small and large duration σ.
For small duration $TE = 2\sigma = 10\text{ms}$ with one period of cos-OGSE, the simulated signal for impermeable sphere of radius $R = 4.5\mu\text{m}$ with diffusion coefficient $D = 3 \cdot 10^{-3}\text{mm}^2/\text{s}$ and $b = 1000\text{s}/\text{mm}^2$ versus spatial discretization are shown in Table 2.1.

Table 2.1: The simulated signal obtained by FEM-RKC in spatial discretization for cos-OGSE sequence with the number of periods $n = 1$, impermeable sphere of radius $R = 4.5\mu\text{m}$, $D = 3 \cdot 10^{-3}\text{mm}^2/\text{s}$, $TE = 2\sigma = 10\text{ms}$, and $b = 1000\text{s}/\text{mm}^2$

spatial discretization	simulated signal
2.000	0.17858
0.912	0.17433
0.418	0.17337
0.186	0.17314

Compared to the exact signal 0.17308, FEM-RKC gives the second order of the signal in spatial discretization.

The signal obtained by FEM-RKC for cos-OGSE sequence with $n = 100$ periods, $TE = 2\sigma = 400$ms at $b-$values from 0 to 500s/mm^2 for an impermeable disk of radius $R = 4.5\mu$m, $D = 3 \cdot 10^{-3}$mm^2/s, also converges to the analytical solution at the second order in h (Fig. 2.7a). Similarly, we also obtain the second order convergence for a 3-dimensional impermeable sphere (Fig. 2.7b).

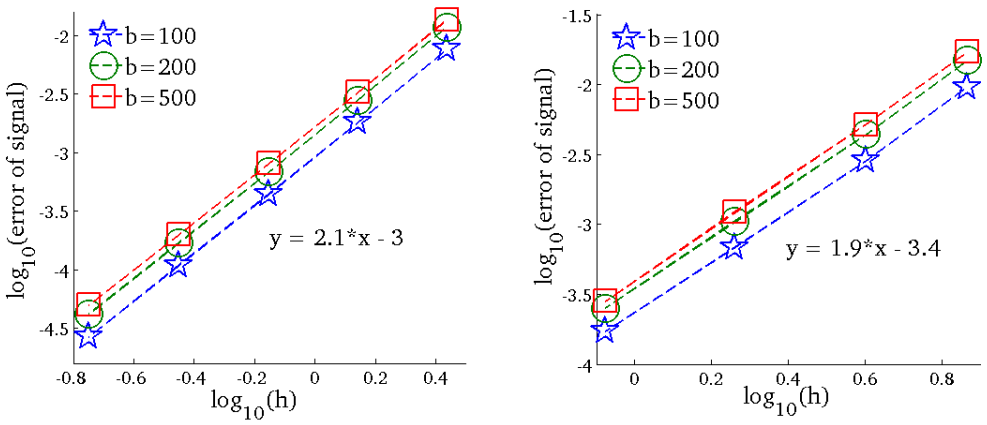

(a) (b)

Figure 2.7: The convergence of the dMRI signal versus space discretization for an impermeable circular cell in 2D (2.7a) and an impermeable spherical cell in 3D (2.7b) with the same cell radius of $R = 4.5\mu$m, $D = 3 \cdot 10^{-3}$mm^2/s, $TE = 2\sigma = 400$ms.

2.4.3.3 Permeable square cell

For permeable square cells, there is no analytical solution. We will compare our numerical solution with the reference numerical solution obtained at the finest mesh. One square cell of side length $L = 8\mu$m is placed in the center of the domain $C = [-5\mu\text{m}; 5\mu\text{m}]^2$. The boundary conditions on ∂C imply the periodic repetition of the square cell outside of C. Both intra-cellular and extra-cellular compartments have the same intrinsic diffusion coefficient $D = 3 \times 10^{-3}$mm^2/s. Setting the permeability $\kappa = 10^{-5}\frac{\text{m}}{\text{s}}$ for the interface, we consider one case of gradient amplitude $\|\mathbf{g}\| = 373.8\frac{\text{mT}}{\text{m}}$. The mesh size was varied from 253 vertices to 7513 vertices and all obtained solutions are compared with the reference solution obtained at 81041 vertices. The time profile is the PGSE sequence with $\Delta = \delta = 10$ms.

The results show that FEM-RKC gives the second order convergence in the L^2 and L^∞ norms (Fig. 2.8a) and the second order convergence in the dMRI signal (Fig. 2.8b), where h is the maximum element size.

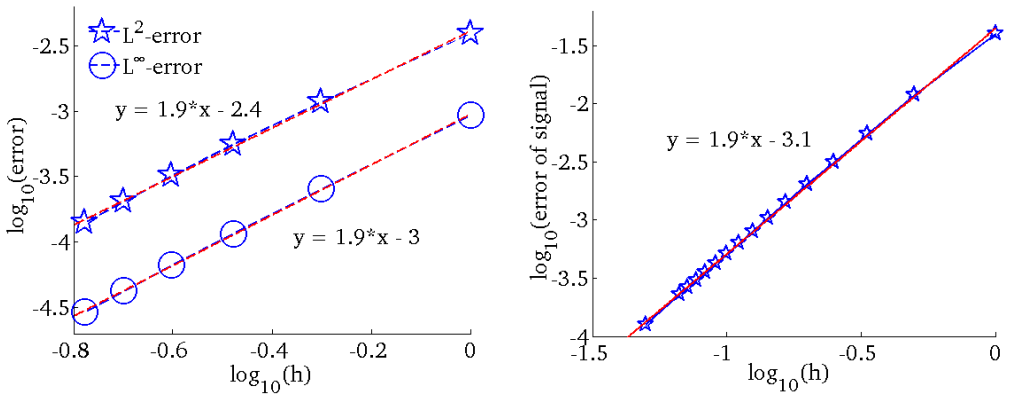

(a) (b)

Figure 2.8: The spatial convergence for permeable square cells is of the second order in the L_2-norm and the L_∞-norm (2.8a) as well as in the dMRI signal (2.8b).

2.4.3.4 Approximation of the interface

Next, we verify that the approximation of the geometry of the interface is more accurate for FEM than FVM, leading to a more accurate dMRI signal approximation. We consider a periodic domain with many striped squares and extract two periodic subdomains: domain 1 and domain 2 (Fig. 2.9).

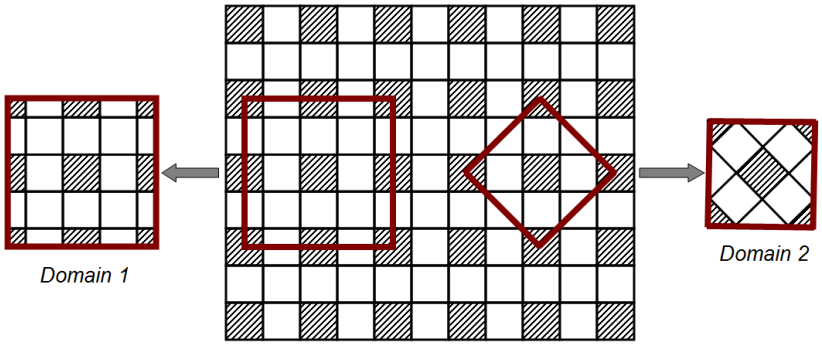

Figure 2.9: Two different computational boxes derived from a periodic domain.

In theory, the signals computed by solving the Bloch-Torrey equation with pseudo-periodic BCs on both cases should be identical. We perform two simulations with the parameters $D^1 = 3 \cdot 10^{-3}\text{mm}^2/\text{s}$, $D^2 = 10^{-3}\text{mm}^2/\text{s}$, $\kappa = 5 \cdot 10^{-5}\frac{\text{m}}{\text{s}}$, using the PGSE sequence with $\delta = \Delta = 5\text{ms}$. The mesh size is 64×64 for FEM-RKC and 300×300 for FVM-RKC. The results for RKC tolerance $tol = 10^{-6}$ are summarized in Table 2.2.

Table 2.2: The dMRI signals computed on domains 1 and 2 from Fig. 2.9 with $D^1 = 3 \cdot 10^{-3}\text{mm}^2/\text{s}$, $D^2 = 10^{-3}\text{mm}^2/\text{s}$, $\kappa = 5 \cdot 10^{-5}\frac{\text{m}}{\text{s}}$, and a PGSE sequence with $\delta = \Delta = 5\text{ms}$, RKC tolerance $tol = 10^{-6}$.

b-value (s/mm^2)	FEM-RKC		FVM-RKC	
	domain 1	domain 2	domain 1	domain 2
0.00	1.0000	1.0000	1.0000	1.0000
92.59	0.8513	0.8514	0.8517	0.8548
370.37	0.5520	0.5526	0.5533	0.5555
833.33	0.3223	0.3226	0.3232	0.3141
1481.48	0.2120	0.2120	0.2123	0.1934
2314.81	0.1680	0.1681	0.1683	0.1456
3333.33	0.1478	0.1480	0.1481	0.1248

One can see that FEM-RKC gives a good approximation of slanted interfaces whereas FVM-RKC fails at high b-values. In fact, the approximation of the slanted interface on a Cartesian grid by a zigzag curve leads to significant errors in the surface area, whatever the spatial resolution of the grid.

2.4.4 Computational efficiency

The RKC solver for parabolic PDEs has the second order convergence in time [76], and this remains true for FEM-RKC. On the other hand, the Backward Euler method has the first order convergence in time.

We numerically show that FEM-RKC is more efficient than FVM-RKC and FEM-BE in running time.

First we fix the mesh size of 200×200 and keep the same parameters: homogeneous domain $C = [-5\mu\text{m}, 5\mu\text{m}]^2$, initial condition as a Dirac delta distribution at $\mathbf{r}_0 = (0, 0)$, diffusion coefficient $D = 3 \cdot 10^{-3}\text{mm}^2/\text{s}$, $\|\mathbf{g}\| = 373.8\frac{\text{mT}}{\text{m}}$. The solution is computed at $t = 2\text{ms}$ for a *constant* gradient, $f(t) = 1, t = 0 \ldots 2\text{ms}$.

Table 2.3: Accuracy and timing of FEM-RKC and FVM-RKC.

	FEM-RKC			FVM-RKC		
Tol	L^2-error	L^∞-error	Timing (s)	L^2-error	L^∞-error	Timing (s)
10^{-3}	$1.05 \cdot 10^{-3}$	$7.02 \cdot 10^{-4}$	41.19	$3.28 \cdot 10^{-3}$	$8.18 \cdot 10^{-3}$	7.78
10^{-4}	$3.93 \cdot 10^{-4}$	$3.03 \cdot 10^{-4}$	54.79	$2.97 \cdot 10^{-3}$	$6.35 \cdot 10^{-3}$	7.62
10^{-5}	$9.89 \cdot 10^{-5}$	$3.19 \cdot 10^{-5}$	87.37	$1.99 \cdot 10^{-3}$	$1.88 \cdot 10^{-3}$	8.06
10^{-6}	$1.71 \cdot 10^{-5}$	$5.45 \cdot 10^{-6}$	142.11	$1.18 \cdot 10^{-3}$	$5.25 \cdot 10^{-4}$	9.09
10^{-7}	$1.84 \cdot 10^{-6}$	$4.26 \cdot 10^{-7}$	240.72	$6.18 \cdot 10^{-4}$	$9.75 \cdot 10^{-5}$	14.99

For FVM-RKC and FEM-RKC, we vary the relative and absolute error tolerances of RKC solver from $tol = 10^{-3}$ to 10^{-7} and present the accuracy in Table 2.3.

Table 2.4: Accuracy and timing of FEM-BE for different sizes of time stepping.

dt (μs)	L^2-error	L^∞-error	Timing (s)
2	$3.83 \cdot 10^{-5}$	$1.01 \cdot 10^{-5}$	1147.21
4	$8.98 \cdot 10^{-5}$	$2.43 \cdot 10^{-5}$	591.22
8	$1.93 \cdot 10^{-4}$	$5.25 \cdot 10^{-5}$	314.13
10	$2.45 \cdot 10^{-4}$	$6.67 \cdot 10^{-5}$	258.31
20	$5.04 \cdot 10^{-4}$	$1.38 \cdot 10^{-4}$	148.41
25	$6.34 \cdot 10^{-4}$	$1.74 \cdot 10^{-4}$	126.11
40	$1.02 \cdot 10^{-3}$	$2.82 \cdot 10^{-4}$	90.70
100	$2.61 \cdot 10^{-3}$	$7.28 \cdot 10^{-4}$	55.01
200	$5.29 \cdot 10^{-3}$	$1.53 \cdot 10^{-3}$	43.58

For FEM-BE, we change the time stepping from 2μs to 200μs (see Table 2.4). These two tables show that FVM-RKC can provide moderate accuracy in a short computational time. However, it does not allow high accuracy on this mesh. In fact, because FVM-RKC has the first order spatial convergence, one needs a finer mesh to get higher accuracy. It is time-consuming for Backward-Euler to get high accuracy because it has the first order time convergence. In contrast, FEM-RKC can provide high accuracy with moderate computational time.

Now, we fix the tolerance of RKC solver at tol $= 10^{-9}$ and consider different mesh sizes. The mesh size was varied from 20×20 to 640×640 for FVM-RKC and from 10×10 to 100×100 for FEM-RKC. We keep the same time stepping dt $= 2\mu$s and vary the mesh size from 10×10 to 80×80 for FEM-BE. The results show that the same accuracy is obtained with FEM-RKC much faster than with FVM-RKC and FEM-BE (Fig. 2.10).

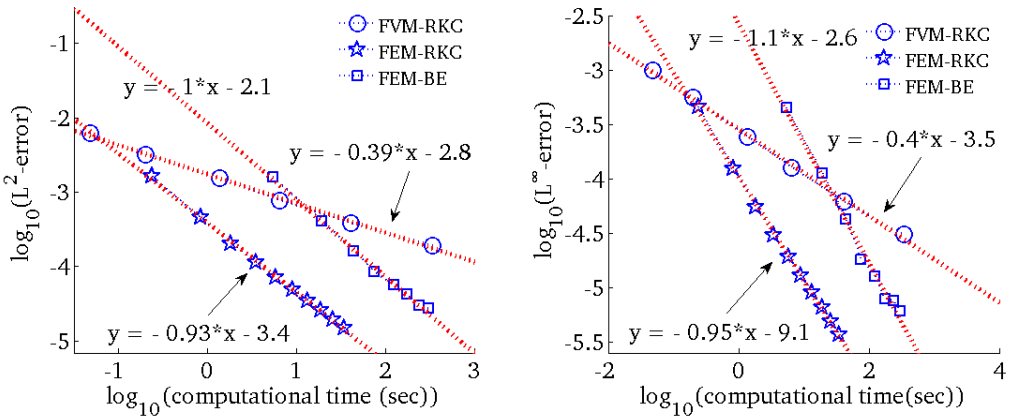

(a) (b)

Figure 2.10: The accuracy of FEM-RKC, FEM-BE and FVM-RKC versus computational time (in second) for different mesh sizes.

2.4.5 Timing on heterogeneous domain

We simulated both PGSE and OGSE sequences on the computational box $C = [-20\mu\text{m}; 20\mu\text{m}]^3$ containing random curved cylindrical cells (Fig. 2.11) created by Salome. The random curved cylinders do not overlap but they do cut the exterior boundaries. Because of that, the water molecules are not obstructed since the domain is periodically repeated. To ensure that the domain is periodic at the boundary ∂C, we create one-eighth of the domain on $[0; 20\mu\text{m}]^3$ including a set of 43 random curved cylinders and the remaining part is the extra-cellular space. The radius r of the curved cylinders is set to 1.2 μm to obtain an intra-cellular volume fraction of $v^c = 40.3\%$. Then, this one-eighth subdomain is mirror reflected across the three planes, $x = 0$, $y = 0$, $z = 0$, to obtain C.

For simulation, the same diffusion coefficient $D = 10^{-3}\text{mm}^2/\text{s}$ was set for both intra-cellular and extra-cellular compartments. A permeability condition with $\kappa = 10^{-5}\frac{\text{m}}{\text{s}}$ was set between the cylinders and the extra-cellular compartment. The uniform distribution $M(\mathbf{r}, 0) = 1$ was set as the initial condition.

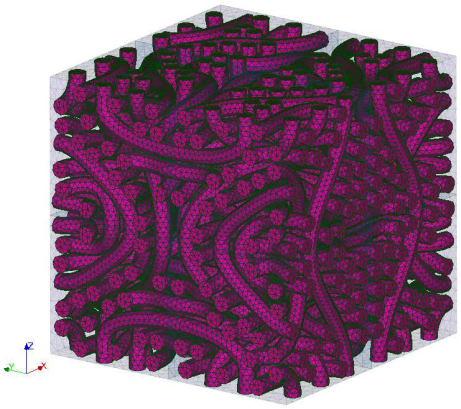

Figure 2.11: The sample with random curved cylinders created by Salome with intra-cellular volume fraction $v^c = 40.3\%$ and 260363 nodes. The random curved cylinders do not overlap.

For such a large scale problem, the sparse LU decomposition (Gaussian elimination) failed to work. The iterative Krylov solver, the GMRES method, was used. We set RKC tolerance at 10^{-4}, the GMRES absolute tolerance at 10^{-10} and the GMRES relative tolerance at 10^{-6}. The slowest computation took about 3 hours for one $b-$value of the cos-OGSE sequence with $n = 4$ periods and the fastest computation was about 20 minutes for one $b-$value ($b > 0$) for the PGSE sequence. The memory usage was 1.4G.

Figure 2.12a shows the dMRI signals for the OGSE sequence with two different frequencies and the PGSE sequence. The signal becomes smaller at higher frequency. The running time increases monotonically with the gradient amplitude $\|\mathbf{g}\|$ (Fig. 2.12b). Because of the reduction of oscillations by transforming the unknown to $m(\mathbf{r}, t)$, the running time only increases slightly with $\|\mathbf{g}\|$.

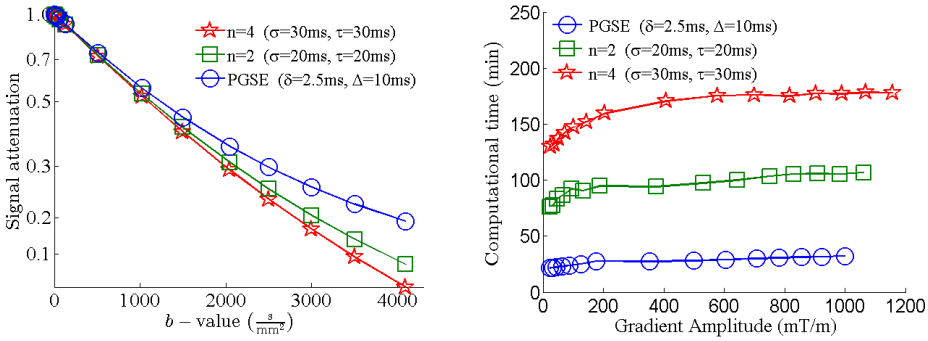

(a) (b)

Figure 2.12: Signal (2.12a) and running time (in minute) (2.12b) for the cos-OGSE sequence with $n = 2, 4$ periods and the PGSE sequence, on the random curved cylinders domain with intra-cellular volume fraction $v^c = 40.3\%$.

2.5 Conclusion

We developed an efficient FEM-RKC method combining the RKC time-stepping method with a specially formulated finite elements spatial discretization to solve two PDEs coming from the field of diffusion MRI. Based on the double-node technique and a body-fitting mesh, FEM-RKC can give a better approximation at the cell interfaces than a Cartesian spatial discretization. By a transformation of the Bloch-Torrey PDE, the pseudo-periodic boundary conditions were transformed to periodic ones and oscillations in the solution were reduced. The FEM-RKC method with linear basis functions gives the second order convergence in both time and space, compared to the approach in the existing literature which is first order accurate in space and time. Our method should result in improvements in both the computational time and the accuracy of dMRI signal simulations. This efficient method can become a useful tool to investigate the diffusion of water molecules in complex biological domains.

Chapter 3

Applications of FEM-RKC code to study diffusion MRI

Summary In this chapter, the FEM-RKC code proposed in Chapter 2 is applied to study the diffusion MRI signal. First, the convergence of the apparent diffusion tensor in the long time limit to the value predicted by the effective diffusion tensor obtained by mathematical homogenization theory was considered. A numerical study was conducted in two and three dimensions to demonstrate the convergence as a function of the diffusion time. Second, we study the relation between the two-compartment model of the biological cell and the corresponding three-compartment model where a thick layer around the biological cell membrane is introduced as the third compartment. We show that the dMRI signal obtained from the two-compartment model approximates the dMRI signal from the three-compartment model as the layer thickness decreases, for both isotropic and tangential membrane diffusion tensors. Finally, we use the code to validate the Kärger model of the dMRI signal, which is a reduced model taking into account inter-compartmental exchange.

3.1 Effective diffusion tensor from homogenization

The standard formulation of homogenization [4] assumes the continuity of the PDE solution. By using a modified formulation of homogenization in which the solution may have jumps at interfaces [10], we compute the effective diffusion tensor and show the convergence of the ADC to the value predicted by homogenization as the diffusion time increases, for complex geometrical domains in 2D and 3D.

To compute the ADC, we solve the Bloch-Torrey equation (1.23) with the conditions Eqs. (1.24, 1.25,1.27,1.28) for Stejskal-Tanner PGSE sequences (Figure 1.1a) with two rectangular gradient pulses of a fixed duration δ and several diffusion times Δ to obtain the dMRI signal at some $b-$values. Not accounting for fitting errors, the apparent diffusion coefficient (ADC) is the first moment of the logarithm of the normalized dMRI signal with respect to b-value computed by Eq. (1.15). To

compute the effective diffusion tensor, we solve the Laplace equation (1.31) with conditions (1.24,1.25,1.32,1.33) to obtain $\mathbf{D}^{\text{hom}}$ via Eq. (1.34). In this section, we show numerically that the ADC converges to $\frac{\mathbf{g}^T}{\|\mathbf{g}\|}\mathbf{D}^{\text{hom}}\frac{\mathbf{g}}{\|\mathbf{g}\|}$, where $\mathbf{g}$ is the gradient direction.

In two biological samples we consider below (Figures 3.1a and 3.3a), the dMRI signals are computed for five $b-$values $0, 50, 200, 500$ and $1000\,\text{s/mm}^2$. From each Δ, the ADC is obtained by fitting the function $-\log S(b)/\log S(0)$ using a cubic polynomial.

The problem is first considered on a computational domain $C = [-5\mu\text{m}; 5\mu\text{m}]^2$ in which the cells have irregular shapes and varying sizes (Figure 3.1a). The black part is considered as the extra-cellular space and the intra-cellular space is what remains.

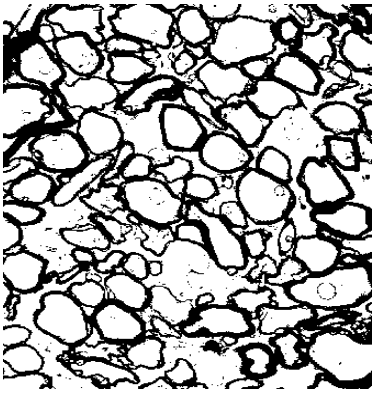

(a)

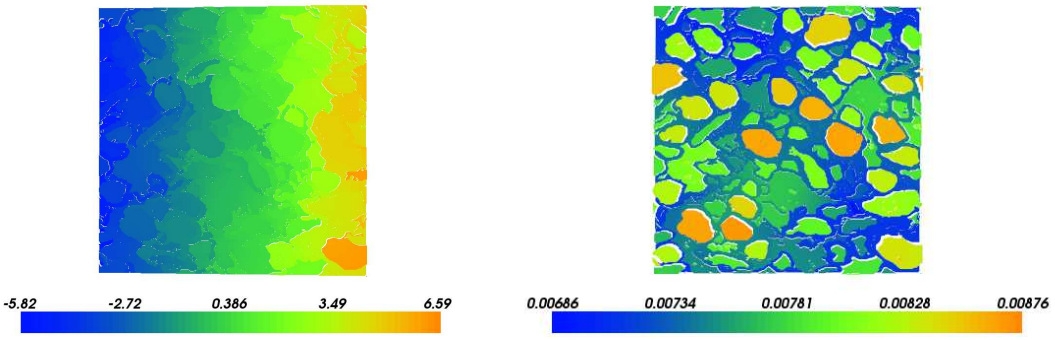

(b) (c)

Figure 3.1: A computational domain in which the cells have irregular shapes and variable sizes (3.1a) and numerical solutions for the direction [1,0] of the steady-state Laplace equation (3.1b) and the time-dependent Bloch-Torrey equation (3.1c) on this domain.

This structure is loaded to Matlab and then the mesh is created, with 14705 vertices. The boundary conditions (1.24, 1.25) require that the opposite boundaries of the

computational domain should be aligned, while Figure 3.1a shows that the cells cut boundaries randomly. A special treatment for the case, when the cell interfaces touch the exterior boundaries, presented in section 2.2.3, is applied to deal with this problem.

We show the solutions obtained by solving Laplace equation (Figure 3.1b) and Bloch-Torrey equation (Figure 3.1c) for $D^e = D^c = 3 \cdot 10^{-3}\text{mm}^2/\text{s}$, $\kappa = 5 \cdot 10^{-5}\text{m/s}$, $\delta = 2.5\text{ms}$ and $\Delta = 5\text{ms}$ for the gradient direction [1,0].

To compute the ADC, we solve the Bloch-Torrey equation for several diffusion times with $\Delta = 5, 10, 20, 40, 80, 160\text{ms}$. The simulations were performed by the FEM-RKC code that took from 5 minutes ($\Delta = 5\text{ms}$) to 20 minutes ($\Delta = 160\text{ms}$) for each b-value.

In Figure 3.2, we plot the entries of ADC and $\frac{\mathbf{g}^T}{\|\mathbf{g}\|}\mathbf{D}^{\text{hom}}\frac{\mathbf{g}}{\|\mathbf{g}\|}$ against Δ^{-1} for two gradient directions [1,0] and [0,1]. One can see that the ADC linearly approaches the effective diffusion tensor $\frac{\mathbf{g}^T}{\|\mathbf{g}\|}\mathbf{D}^{\text{hom}}\frac{\mathbf{g}}{\|\mathbf{g}\|}$. The convergence slope is different for different gradient directions. Based on the ADC and $\frac{\mathbf{g}^T}{\|\mathbf{g}\|}\mathbf{D}^{\text{hom}}\frac{\mathbf{g}}{\|\mathbf{g}\|}$, we see that diffusion in this computational domain is anisotropic and the water molecules can move in direction [0,1] faster than in direction [1,0].

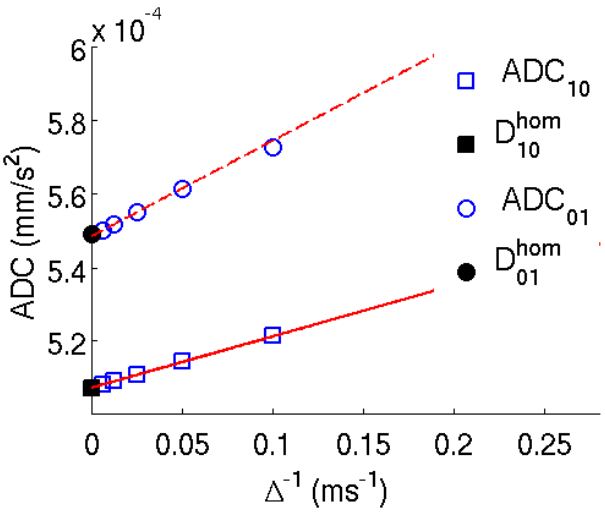

Figure 3.2: The convergence of ADC to $\frac{\mathbf{g}^T}{\|\mathbf{g}\|}\mathbf{D}^{\text{hom}}\frac{\mathbf{g}}{\|\mathbf{g}\|}$ for diffusion inside the domain shown in Figure 3.1a for two gradient direction $[1, 0]$ and $[0, 1]$. The same intrinsic diffusion coefficient is set for extra-cellular and intra-cellular spaces, $D^e = D^c = 3 \cdot 10^{-3}\text{mm}^2/\text{s}$. The permeability $\kappa = 5 \cdot 10^{-5}\text{m/s}$ is set for the membrane. The ADC linearly approaches the effective diffusion tensor $\frac{\mathbf{g}^T}{\|\mathbf{g}\|}\mathbf{D}^{\text{hom}}\frac{\mathbf{g}}{\|\mathbf{g}\|}$ versus Δ^{-1}.

Next, we simulate a 3D example. The computational domain $C = [-10\mu\text{m}, 10\mu\text{m}]^3$ contains 100 Voronoi cells (Figure 3.3a) with intra-cellular volume fraction $v^c = 61.4\%$ and surface-to-volume ratio $1.03\mu\text{m}^{-1}$. The same intrinsic diffusion coefficient $D^e = D^c = 10^{-3}\frac{\text{mm}^2}{\text{s}}$ is set for both intra-cellular and extra-cellular com-

partments. Two permeabilities, $\kappa = 10^{-5}\frac{\mathrm{m}}{\mathrm{s}}$ and $\kappa = 10^{-4}\frac{\mathrm{m}}{\mathrm{s}}$, were simulated. The Bloch-Torrey PDE was solved for the PGSE sequences with $\delta = 2.5$ms and several $\Delta = 10, 20, 40, 80, 160$ms. The steady-state Laplace PDE was also solved over C to obtain $\mathbf{D}^{\mathrm{hom}}$.

Similarly to 2D, Figures 3.3b and 3.3c show that ADC converges to $\frac{\mathbf{g}^T}{\|\mathbf{g}\|}\mathbf{D}^{\mathrm{hom}}\frac{\mathbf{g}}{\|\mathbf{g}\|}$ in three gradient directions: $[1,0,0]$, $[0,1,0]$ and $[0,0,1]$, for both $\kappa = 10^{-4}\frac{\mathrm{m}}{\mathrm{s}}$ and $\kappa = 10^{-5}\frac{\mathrm{m}}{\mathrm{s}}$.

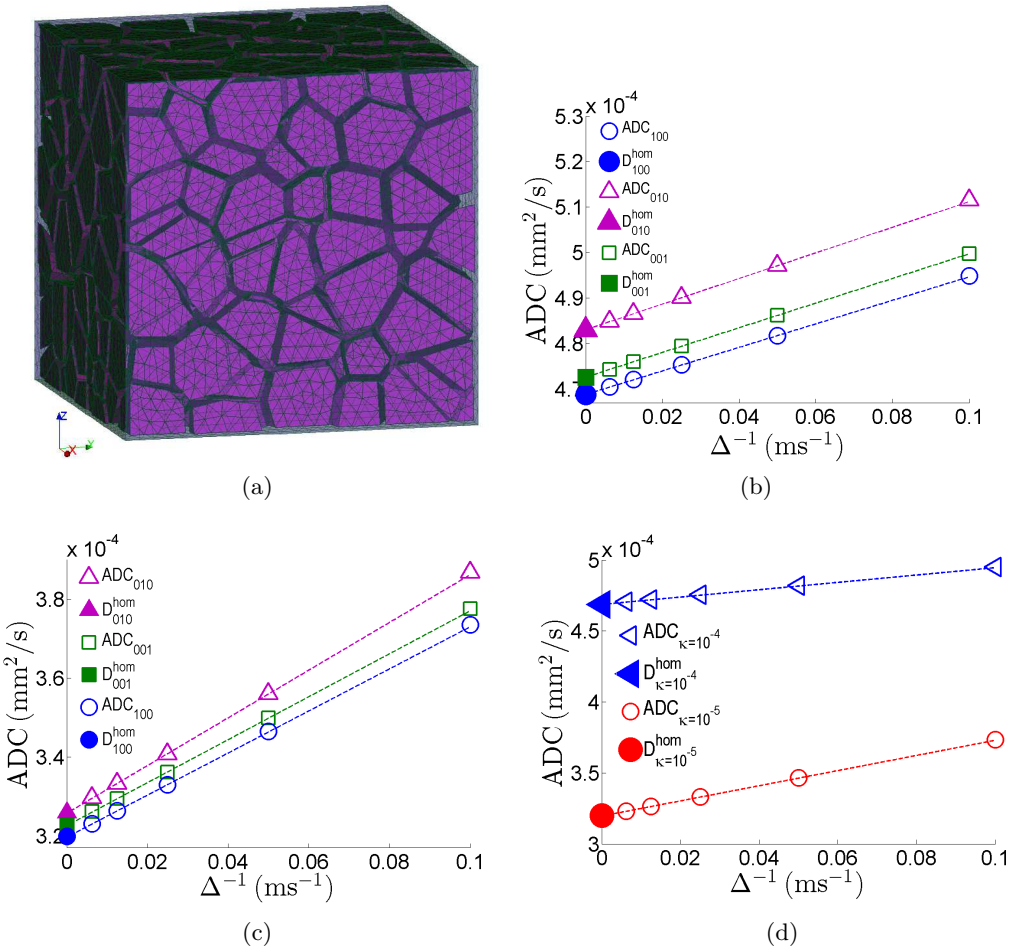

Figure 3.3: The computational domain with 100 Voronoi cells (3.3a) and the convergence of ADC to $\frac{\mathbf{g}^T}{\|\mathbf{g}\|}\mathbf{D}^{\mathrm{hom}}\frac{\mathbf{g}}{\|\mathbf{g}\|}$ in three directions [1,0,0], [0,1,0] and [0,0,1] for $\kappa = 10^{-4}\frac{\mathrm{m}}{\mathrm{s}}$ (3.3b) and $\kappa = 10^{-5}\frac{\mathrm{m}}{\mathrm{s}}$ (3.3c). With the same gradient direction $[1,0,0]$, the convergence is faster at higher permeability (Figure 3.3d) and seems to be linear versus Δ^{-1} when the diffusion time is long enough.

Since water molecules can move more easily at higher permeability, the ADC and $\frac{\mathbf{g}^T}{\|\mathbf{g}\|}\mathbf{D}^{\mathrm{hom}}\frac{\mathbf{g}}{\|\mathbf{g}\|}$ are bigger (Figure 3.3d). The convergence curve seems to be linear versus Δ^{-1} when the diffusion time $\Delta - \delta/3$ is long enough that agrees with the

result for 1D periodic structure in the long-time regime [79].

The computation of $\mathbf{D}^{\text{hom}}$ is much faster than that of the ADC. For a mesh size with 28688 vertices, each ADC is computed in 10 to 20 minutes whereas the computation of one $\mathbf{D}^{\text{hom}}$ takes less than one minute.

This approach can be applied to general geometrical shapes, as long as a good mesh can be generated. Other diffusion-encoding pulse sequences may be used for long enough diffusion times.

The analysis of the steady-state Laplace equation within homogenization theory is much easier than that of the time-dependent Bloch-Torrey equation. We expect that the experimentally obtained apparent diffusion tensors can be used to estimate $\frac{\mathbf{g}^T}{\|\mathbf{g}\|}\mathbf{D}^{\text{hom}}\frac{\mathbf{g}}{\|\mathbf{g}\|}$ by extrapolation in Δ^{-1} and then information, obtained analytically or numerically, about $\frac{\mathbf{g}^T}{\|\mathbf{g}\|}\mathbf{D}^{\text{hom}}\frac{\mathbf{g}}{\|\mathbf{g}\|}$, can be used to infer the properties of the imaged sample.

3.2 Layer compartments and interface conditions

In this section, we will study the effect of including a separate diffusion layer between the intra and the extra-cellular compartments. We refer to the model where the intra and extra-cellular compartments are divided by an infinitely thin interface as the two-compartment model of biological tissue, and the model where a layer compartment of non-zero thickness is placed between the intra and extra-cellular compartments as the three compartment model of biological tissue.

3.2.1 Myelin sheath and slow diffusion layer around cell membranes

Biological cells have plasma membranes that are very thin. The membrane thickness is on the order of nanometers. However, Le Bihan [39] has suggested that even though the membrane thickness is much smaller than the dimensions of the biological cells, there may be a thick layer of water in the vicinity of the cell membranes that experience slow diffusion and this effective layer thickness may be on the order of μm.

The nerve axon is surrounded by a so-called myelin layer which is composed by some layers of lipids or proteins [56]. In human brain, the axonal diameter varies between 2 and 7μm, and myelin thickness from 0.5 to 2.5μm [27, 47, 61]. In the normal nerve of the rabbit, the axon diameters range from 0.5μm to 15μm, with the myelin layer having a thickness from 0.5μm to 2.5μm [59]. Because the myelin sheath is comprised of layers of lipids (see Figure 3.4) it is expected that the diffusion tensor in the myelin layer has a tangential component that is larger than the normal component. Further discussion of diffusion inside the myelin sheath can be found in [3, 35, 39].

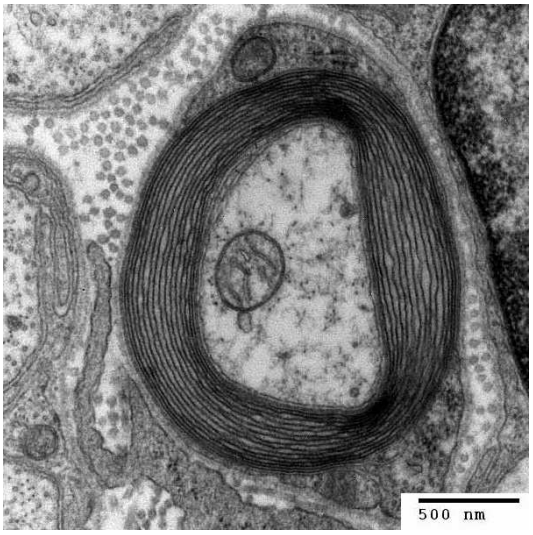

Figure 3.4: Image from Wikipedia Commons. Descriptions: Transmission electron micrograph of a myelinated axon. The myelin layer (concentric) surrounds the axon of a neuron, showing cytoplasmatic organs inside. Generated and deposited into the public domain by the Electron Microscopy Facility at Trinity College. Source http://en.wikipedia.org/wiki/Myelin, Author: user:Roadnottaken.

3.2.2 Three-compartment model of biological tissue

In the three-compartment model of biological tissue, the computational domain is a union of three compartments: the intra-cellular space Ω^c, the extra-cellular space Ω^e, and the membrane layer Ω^m of thickness η (see Figure 3.5a). Each compartment Ω^c and Ω^e is characterized by its own intrinsic diffusion tensor $\mathbf{D}^c$, $\mathbf{D}^e$ respectively. In this section, we assume that diffusion in both compartments Ω^c and Ω^e is isotropic, while diffusion inside the thick membrane may be anisotropic with its diffusion tensor $\mathbf{D}^m$.

Furthermore, the magnetization is supposed to be continuous across the cell-membrane and the membrane-extra-cellular space interfaces. For latter use, we call $\boldsymbol{M}$ the solution M of the Bloch-Torrey equation (1.23) in the three-compartment domain. The interface conditions (1.24, 1.26) at $\Omega^l \cap \Omega^n$ $(l = c, e, m; n = c, e, m; l \neq n)$ can be rewritten

$$\begin{aligned} \mathbf{D}^l \nabla \boldsymbol{M}^l \cdot \mathbf{n}^l &= -\mathbf{D}^n \nabla \boldsymbol{M}^n \cdot \mathbf{n}^n \\ \boldsymbol{M}^l &= \boldsymbol{M}^n \end{aligned} \tag{3.1}$$

where $\mathbf{n}^k$ is the normal vector pointing outward from Ω^k $(k = l, n)$.

3.2.3 The relationship between the two- and three-compartment models

In the two-compartment model, the membrane layer is replaced by an infinitely thin interface Γ (see Figure 3.5b) which is characterized by a finite permeability κ. In our work, Γ is placed in the middle of the membrane layer. For the sake of simplicity, we describe 2D case and assume that Γ is a closed curve which divides the computational domain Ω into two subdomains $\overline{\Omega}^c$ and $\overline{\Omega}^e$. Each subdomain occupies a half of the membrane layer and $\Omega^c \subset \overline{\Omega}^c$, $\Omega^e \subset \overline{\Omega}^e$, $\Omega = \overline{\Omega}^e \cup \overline{\Omega}^c$. We define $\overline{\boldsymbol{M}}^k$ the solution of the Bloch-Torrey equation in the $k-$compartment $(k = c, e)$ on this two-compartment model.

The transverse diffusion coefficient inside the membrane layer (which is perpendicular to Γ) κ_n is related to the permeability κ of Γ as

$$\kappa \approx \kappa_n / \eta. \tag{3.2}$$

At each point $\mathbf{r} \in \Omega^m$, one defines a normal vector $\mathbf{n}(\mathbf{r})$ and a tangential vector $\tau(\mathbf{r})$ to Γ. The diffusion tensor inside the membrane layer can be computed as following

$$\begin{aligned} \mathbf{D}^m(\mathbf{r})\mathbf{n}(\mathbf{r}) &= \kappa_n \mathbf{n}(\mathbf{r}), \\ \mathbf{D}^m(\mathbf{r})\tau(\mathbf{r}) &= \kappa_\tau \tau(\mathbf{r}), \end{aligned} \tag{3.3}$$

where κ_τ indicates the diffusion coefficient along the tangential direction of Γ.

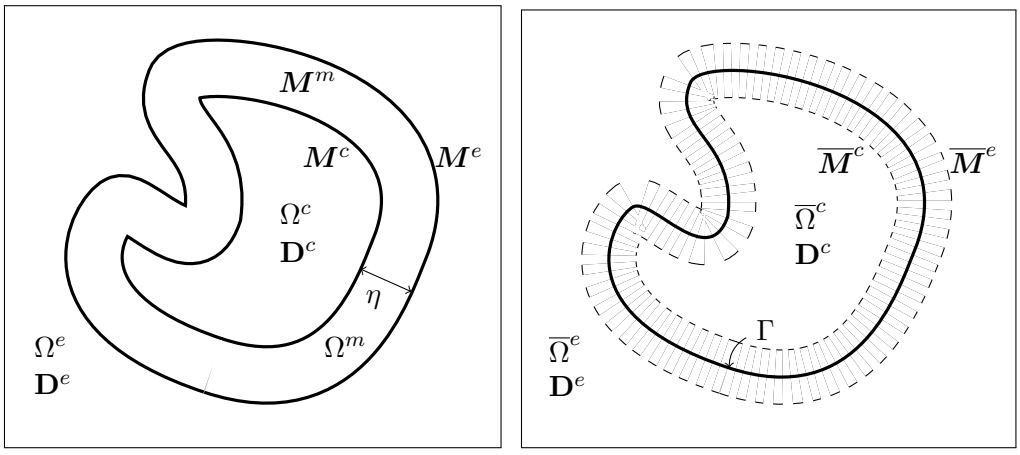

(a) (b)

Figure 3.5: Two models of a cross section of a myelinated axon. In the three-compartment model (3.5a), Ω is a union of three compartments: the intra-cellular space Ω^c, the extra-cellular space Ω^e, and the membrane layer Ω^m of thickness η. Each compartment is characterized by its own intrinsic diffusion tensor $\mathbf{D}^c$, $\mathbf{D}^e$ and $\mathbf{D}^m$ respectively. In the two-compartment model (3.5b), the intermediate layer is replaced by an infinitely thin interface that is characterized by a finite permeability κ.

If diffusion inside the membrane is isotropic, $\kappa_n = \kappa_\tau$, $\mathbf{D}^m$ is diagonal with the same entries

$$\mathbf{D}^m = \kappa\,\eta \begin{bmatrix} 1 & 0 & 0 \\ 0 & 1 & 0 \\ 0 & 0 & 1 \end{bmatrix}.$$

A standard interface condition for the two-compartment model ensures that the flux across the interface is continuous but the magnetization is not [13, 22, 42, 79]

$$\mathbf{D}^l \nabla \overline{\boldsymbol{M}}^l \cdot \mathbf{n}^l = -\mathbf{D}^n \nabla \overline{\boldsymbol{M}}^n \cdot \mathbf{n}^n = \kappa\Big(\overline{\boldsymbol{M}}^n - \overline{\boldsymbol{M}}^l\Big). \tag{3.4}$$

3.2.4 Interface conditions for anisotropic diffusion inside the membrane layer

In this section, we derive the interface conditions for two-compartment model corresponding to the three-compartment model with anisotropic diffusion inside the membrane. We assume that the diffusion coefficient along tangential directions to the membranes is much larger than that along the perpendicular directions: $\kappa_n \ll \kappa_\tau$.

Following the expression of the differential operators given in [23] (see also in [1]), we detail the two dimensional case but similar results should be valid for the three dimensional case. Assuming that Γ is a regular curve (at least C^2) and Ω is simply connected, the boundary Γ can be parametrized in terms of the curvilinear abscissa s as $s \mapsto x_\Gamma(s)$, $s \in [0, L[$, with $|\mathrm{d}x_\Gamma(s)/\mathrm{d}s| = 1$, where L is the length of Γ. We note that this parametrization defines a counter-clockwise orientation. Let $\mathbf{n}$ be the unitary normal vector at $x_\Gamma(s)$ directed to the interior of Ω and set $\tau(s) = \mathrm{d}x_\Omega(s)/\mathrm{d}s$ which is a unitary vector tangential to Γ at $x_\Gamma(s)$. The curvature c can be defined by

$$c(s) := \tau(s) \cdot \mathrm{d}\mathbf{n}(s)/\mathrm{d}s = \nabla_\tau \mathbf{n}.$$

These notations are summarized in Figure 3.6.

Let $\nu_0 := \inf\limits_{0 \le s \le L} \dfrac{1}{|c(s)|}$, $\Omega_0 := \{\mathbf{r}\,;\mathrm{d}(\mathbf{r}, \Gamma) < \nu_0\}$ and x_Γ be the orthogonal projection of $\mathbf{r}$ on Γ. Then,

$$\forall \mathbf{r} \in \Omega_0, \exists!(s, \nu) \in [0, L[\times]-\nu_0, \nu_0[,\ \mathbf{r} = x_\Gamma(s) + \nu\,\mathbf{n}(s). \tag{3.5}$$

The couple (s, ν) will be referred to as curvilinear (or parametric) coordinates of $\mathbf{r} \in \Omega_0$ (with respect to Γ).

Let $\widetilde{\boldsymbol{M}} : [0, L[\times]-\nu_0, \nu_0[$ be defined by $\widetilde{\boldsymbol{M}}(s, \nu) = \boldsymbol{M}(\mathbf{r})$, where $\mathbf{r}$ and (s, ν) satisfy Eq. (3.5). Then, we have

$$\nabla \boldsymbol{M}(\mathbf{r}) = \frac{1}{1 + \nu c} \frac{\partial \widetilde{\boldsymbol{M}}}{\partial s} \tau + \frac{\partial \widetilde{\boldsymbol{M}}}{\partial \nu} \mathbf{n},$$

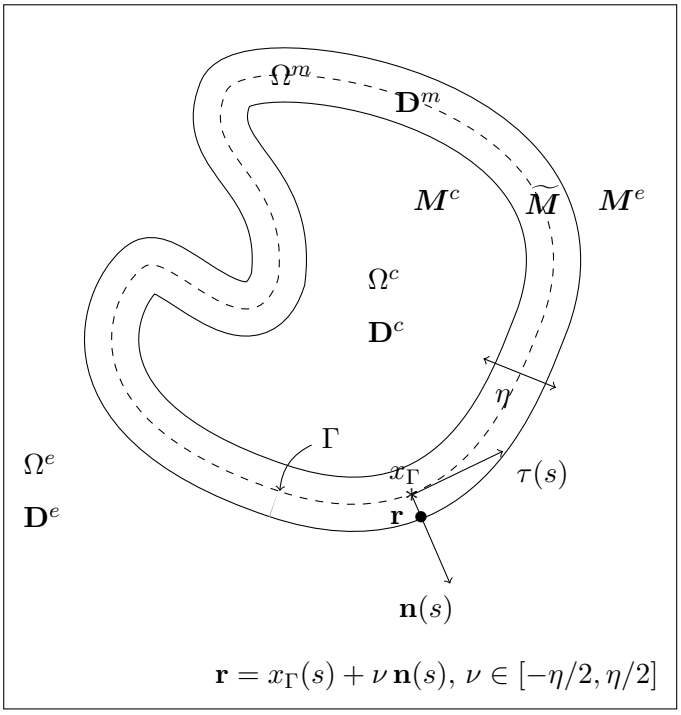

Figure 3.6: Notations

and for a tensor $\mathbf{D}$, we have

$$\begin{aligned}\operatorname{div}\Big(\mathbf{D}\,\nabla \boldsymbol{M}(\mathbf{r})\Big) &= \frac{1}{1+\nu c}\frac{\partial}{\partial s}\left(\frac{1}{1+\nu c}\mathbf{D}\frac{\partial \widetilde{\boldsymbol{M}}}{\partial s}\right) + \frac{1}{1+\nu c}\frac{\partial}{\partial \nu}\left((1+\nu c)\mathbf{D}\frac{\partial \widetilde{\boldsymbol{M}}}{\partial \nu}\right)\\ &= \frac{1}{1+\nu c}\operatorname{div}_\tau\left(\frac{1}{1+\nu c}\mathbf{D}\nabla_\tau \widetilde{\boldsymbol{M}}\right) + \frac{1}{1+\nu c}\frac{\partial}{\partial \nu}\left((1+\nu c)\mathbf{D}\frac{\partial \widetilde{\boldsymbol{M}}}{\partial \nu}\right).\end{aligned}$$

On the membrane Ω^m with assuming $\Omega^m \subseteq \Omega_0$, according to the anisotropy assumption, we have

$$\mathbf{D}^m \nabla \boldsymbol{M}^m = \frac{1}{1+\nu c}\kappa_\tau \nabla_\tau \widetilde{\boldsymbol{M}} + \eta\kappa\partial_\nu \widetilde{\boldsymbol{M}}\,\mathbf{n},$$

and then

$$\operatorname{div}\left(\mathbf{D}^m \nabla \boldsymbol{M}^m\right) = \frac{1}{1+\nu c}\operatorname{div}_\tau\left(\frac{1}{1+\nu c}\kappa_\tau \nabla_\tau \widetilde{\boldsymbol{M}}\right) + \frac{1}{1+\nu c}\partial_\nu\left((1+\nu c)\,\eta\,\kappa\,\partial_\nu \widetilde{\boldsymbol{M}}\right).$$

We set $\xi := \frac{\nu}{\eta}$, with $\nu \in [-\frac{\eta}{2}, \frac{\eta}{2}]$ and then $\xi \in [-\frac{1}{2}, \frac{1}{2}]$. Hence, we obtain:

$$\mathbf{D}^m \nabla \boldsymbol{M} \cdot \mathbf{n} = \kappa\,\partial_\xi \widetilde{\boldsymbol{M}},$$

and

$$\begin{aligned}\operatorname{div}\left(\mathbf{D}^m\nabla\boldsymbol{M}^m\right) &= \frac{1}{1+\eta\xi c}\operatorname{div}_\tau\left(\frac{1}{1+\eta\xi c}\kappa_\tau\nabla_\tau\widetilde{\boldsymbol{M}}\right)+\frac{1}{\eta^2}\frac{1}{1+\eta\xi c}\partial_\xi\left((1+\eta\xi c)\eta\kappa\partial_\xi\widetilde{\boldsymbol{M}}\right)\\ &= \frac{1}{(1+\eta\xi c)^2}\operatorname{div}_\tau\left(\kappa_\tau\nabla_\tau\widetilde{\boldsymbol{M}}\right)-\frac{\eta\xi}{(1+\eta\xi c)^3}\kappa_\tau\nabla_\tau\widetilde{\boldsymbol{M}}\nabla_\tau c\\ &\quad+\frac{\kappa}{\eta}\partial^2_{\xi\xi}\widetilde{\boldsymbol{M}}+\frac{\kappa c}{1+\eta\xi c}\partial_\xi\widetilde{\boldsymbol{M}}.\end{aligned}$$

We also notice that

$$I\,\gamma\,\mathbf{g}\cdot\mathbf{r}\,f(t)\boldsymbol{M}^m = I\,\gamma\,(g_\Gamma\cdot x_\Gamma+g_\nu\eta\xi)f(t)\,\widetilde{\boldsymbol{M}},$$

where g_Γ is the orthogonal projection of $\mathbf{g}$ on Γ.

Then, multiplying the Bloch-Torrey equations (1.23) by $(1+\eta\xi)^3$, we obtain

$$\begin{aligned}&(1+\eta\xi)^3\partial_t\widetilde{\boldsymbol{M}}+(1+\eta\xi)^3\,I\,\gamma\,(g_\Gamma\cdot x_\Gamma+g_\nu\eta\xi)f(t)\widetilde{\boldsymbol{M}}-(1+\eta\xi)\operatorname{div}_\tau\left(\kappa_\tau\nabla_\tau\widetilde{\boldsymbol{M}}\right)\\ &\quad+\eta\xi\kappa_\tau\nabla_\tau\widetilde{\boldsymbol{M}}\nabla_\tau c-\tfrac{\kappa}{\eta}(1+\eta\xi)^3\partial^2_{\xi\xi}\widetilde{\boldsymbol{M}}-(1+\eta\xi)^2\kappa c\partial_\xi\widetilde{\boldsymbol{M}}=\mathbf{0}.\end{aligned}$$

Then, by identification (from the power of $1/\eta$), we obtain:

$$\partial^2_{\xi\xi}\widetilde{\boldsymbol{M}}=0.$$

So,

$$\widetilde{\boldsymbol{M}}(x_\Gamma,\xi)=A(x_\Gamma)+\xi B(x_\Gamma).$$

To shorten notations, we denote $[f_{l,n}]$ and $\left\langle f_{l,n}\right\rangle$ the jump and the average of function f at the interface $\Omega^l\cap\Omega^n$

$$[f]_{l,n}=f^n-f^l,\quad \left\langle f\right\rangle_{l,n}=\frac{f^n+f^l}{2}.$$

and

$$\widetilde{\boldsymbol{M}}^e(x_\Gamma)=\widetilde{\boldsymbol{M}}\Big(x_\Gamma,\frac{1}{2}\Big)\text{ and }\widetilde{\boldsymbol{M}}^c(x_\Gamma)=\widetilde{\boldsymbol{M}}\Big(x_\Gamma,-\frac{1}{2}\Big).$$

Since $[\boldsymbol{M}]_{l,n}=0$ on the interface, we obtain $A(x_\Gamma)=\langle\boldsymbol{M}\rangle_{c,e}$ and $B(x_\Gamma)=[\boldsymbol{M}]_{c,e}$ and then

$$\widetilde{\boldsymbol{M}}\Big(x_\Gamma,\xi\Big)=\left\langle\widetilde{\boldsymbol{M}}\right\rangle_{c,e}+\xi\left[\widetilde{\boldsymbol{M}}\right]_{c,e}.\tag{3.6}$$

Using the flux continuity $[\mathbf{D}\nabla\boldsymbol{M}\cdot\mathbf{n}]_{l,n}=0$, we have

$$\kappa\partial_\xi\widetilde{\boldsymbol{M}}\left(x_\Gamma,\frac{1}{2}\right)=\mathbf{D}^e\nabla\widetilde{\boldsymbol{M}}^e\cdot\mathbf{n}^e\text{ and }\kappa\partial_\xi\widetilde{\boldsymbol{M}}\left(x_\Gamma,-\frac{1}{2}\right)=-\mathbf{D}^c\nabla\widetilde{\boldsymbol{M}}^c\cdot\mathbf{n}^c.$$

Hence

$$\mathbf{D}^c\nabla\widetilde{\boldsymbol{M}}^c\cdot\mathbf{n}^c=-\mathbf{D}^e\nabla\widetilde{\boldsymbol{M}}^e\cdot\mathbf{n}^e=\kappa\left[\widetilde{\boldsymbol{M}}\right]_{c,e}.\tag{3.7}$$

So, we have exactly the same formula proposed for isotropic case Eq. (3.4). However, we emphasize that $\widetilde{\boldsymbol{M}}^c$ and $\widetilde{\boldsymbol{M}}^e$ are defined at $\nu=-\eta/2$ and $\nu=\eta/2$ respectively

and the two-compartment model is established by removing the membrane from the three-compartment model. It means that there is an empty zone between the intra-cellular and extra-cellular compartments. The signal attenuation for two-compartment model in this case should be

$$S = \frac{1}{|\Omega|}\left(\int\limits_{\Omega^c\cup\Omega^e} \boldsymbol{M}\, d\mathbf{r} + \eta \int\limits_{\Gamma} \big\langle \boldsymbol{M} \big\rangle ds\right). \tag{3.8}$$

The empty zone between two compartments Ω^c and Ω^e causes a technical difficulty in implementing the code in 2D and 3D because the vertices along the interface in both compartments should be aligned. To overcome this difficulty, we use Taylor's expansion of $\boldsymbol{M}$ around $\nu = 0$ so that the interface conditions are moved to the middle of the interface. The obtained formula in this case is identical to Eq. (3.7)

$$\mathbf{D}^c \nabla \overline{\boldsymbol{M}}^c \cdot \mathbf{n}^c = -\mathbf{D}^e \nabla \overline{\boldsymbol{M}}^e \cdot \mathbf{n}^e = \kappa \left[\overline{\boldsymbol{M}}\right]_{c,e}.$$

The formula to compute the signal attenuation can be simplified to

$$S = \frac{1}{|\Omega|}\int\limits_{\Omega} \overline{\boldsymbol{M}} d\mathbf{r}. \tag{3.9}$$

In what following, we will numerically study the difference in diffusion characteristics between isotropic and anisotropic diffusion inside the membrane layer.

3.2.5 Simulations

We perform the simulations on the domain $C = [-5\mu\text{m}, 5\mu\text{m}]^d$ containing one circular/spherical cell of radius $R = 4\mu$m. Four values of the thickness $\eta = 0.2, 0.4, 0.8$ and 1.6μm of the membrane layer are used to check the closeness of the two models. Ten $b-$values b =0, 100, 500, 1000, 1500, 2000, 2500, 3000, 3500, 4000 s/mm^2 were considered. The same intrinsic diffusion coefficient $D = 3{\cdot}10^{-3}$ mm^2/s is set for both extra-cellular and intra-cellular compartments. For the three-compartment model with isotropic diffusion in the membrane layer, the diffusion coefficient $D^m = \kappa\,\eta$ is set for the membrane layer. For the three-compartment model with anisotropic diffusion in the membrane layer, the diffusion coefficients are different for different diffusion directions. The diffusion coefficient $\kappa_n = \kappa\,\eta$ is set for the normal direction and $\kappa_\tau = 3 \cdot 10^{-3}$mm^2/s is set for the tangential direction.

For 2D ($d = 2$), the first result is that the signals of three-compartment models with both isotropic and anisotropic diffusion in the membrane layer approach the signal of two-compartment model. It means that when $\eta \to 0$, the contribution of tangential diffusion coefficient is vanishing.

However, there is a significant difference between signals of isotropic and anisotropic diffusion inside a thick membrane layer, and the two-compartment model is always

closer to the three-compartment model with anisotropic diffusion than the three-compartment model with isotropic diffusion in the membrane. Figure 3.7 illustrates this result for the diffusion time $\Delta = 10$ms and $\kappa = 10^{-5}$m/s.

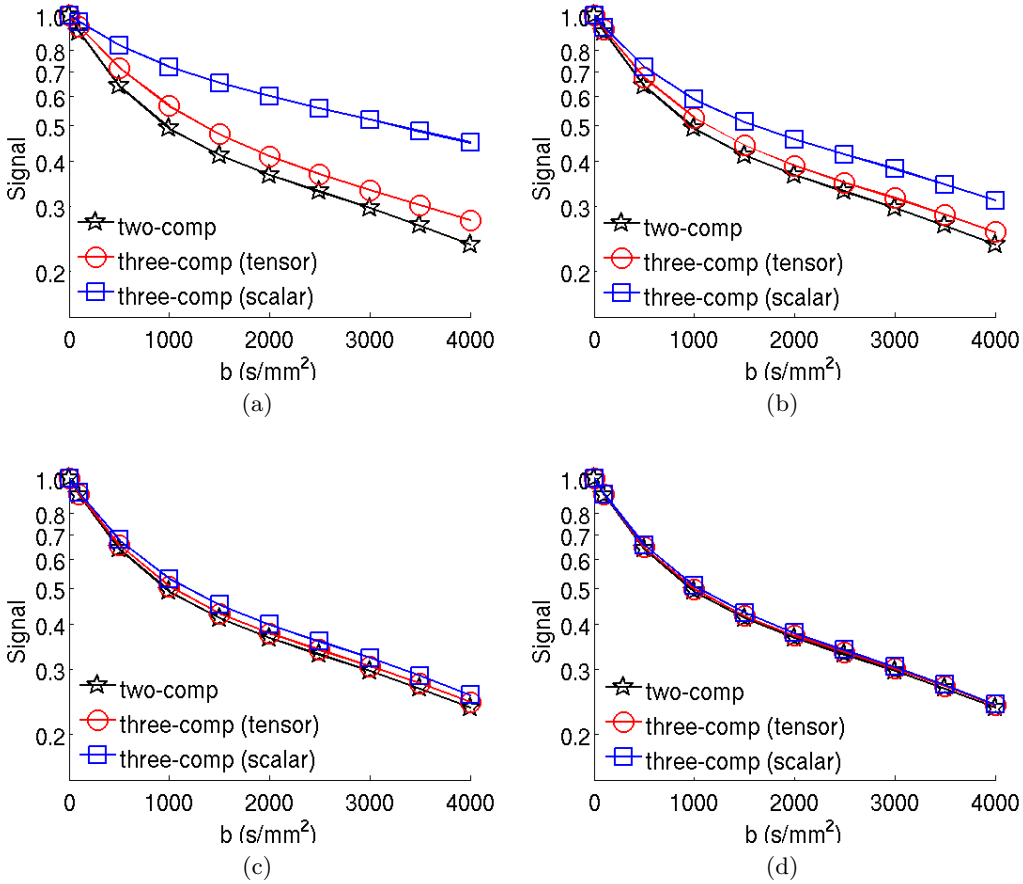

Figure 3.7: Signals of both three-compartment models with isotropic diffusion and anisotropic diffusion in the membrane approach the signal of two-compartment model. Four values of the thickness $\eta = 1.6\mu$m (3.7a), $\eta = 0.8\mu$m (3.7b), $\eta = 0.4\mu$m (3.7c) and $\eta = 0.2\mu$m (3.7d) were considered for $\Delta = 10$ms and $\kappa = 10^{-5}$m/s. However, the signal of two-compartment model is always closer to the signal of the three-compartment model with anisotropic diffusion than to the signal of the three-compartment model with isotropic diffusion in the membrane.

Figure 3.8 shows the convergence slope of the signals of the three-compartment models to the signal of the two-compartment model. Although the L_2- difference between signals of the three-compartment with anisotropic diffusion in the membrane and the two-compartment model is smaller than that between the three-compartment with isotropic diffusion in the membrane and the two-compartment model, both have the first order convergence versus the thickness.

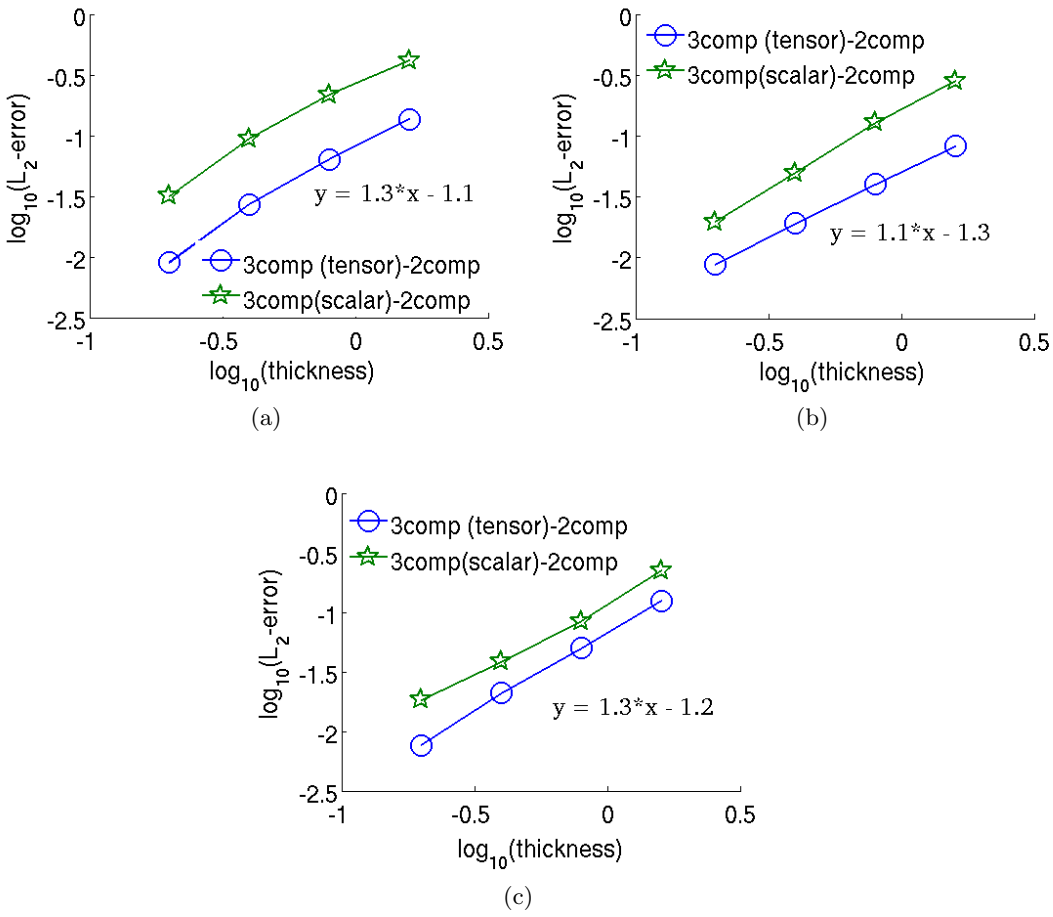

Figure 3.8: The convergence of the three-compartment models to the two compartment model for different diffusion times $\Delta = 2.5$ms (3.8a), $\Delta = 10$ms (3.8b) and $\Delta = 100$ms (3.8c).

The approximation is better at higher permeabilities but the convergence order does not change.

The above results remain true for 3D ($d = 3$). Figure 3.9a shows the $\frac{\mathbf{g}^T}{\|\mathbf{g}\|}\mathbf{D}^{\text{hom}}\frac{\mathbf{g}}{\|\mathbf{g}\|}$, for $\mathbf{g}/\|\mathbf{g}\| = [1, 0, 0]$, computed by solving the steady-state Laplace PDEs (1.31, 1.24, 1.25, 1.32, 1.33) for two- and three-compartment domains with $\kappa = 5 \cdot 10^{-5} \frac{\text{m}}{\text{s}}$. As η tends to 0, the $\frac{\mathbf{g}^T}{\|\mathbf{g}\|}\mathbf{D}^{\text{hom}}\frac{\mathbf{g}}{\|\mathbf{g}\|}$ from the three-compartment models with isotropic and anisotropic diffusion in the membrane layer both linearly approach to $\frac{\mathbf{g}^T}{\|\mathbf{g}\|}\mathbf{D}^{\text{hom}}\frac{\mathbf{g}}{\|\mathbf{g}\|}$ of the two-compartment model. However, the difference between $\frac{\mathbf{g}^T}{\|\mathbf{g}\|}\mathbf{D}^{\text{hom}}\frac{\mathbf{g}}{\|\mathbf{g}\|}$ of the three-compartment model with anisotropic diffusion and the two-compartment model is smaller than that between the three-compartment model with isotropic diffusion and the two-compartment model (Figure 3.9b).

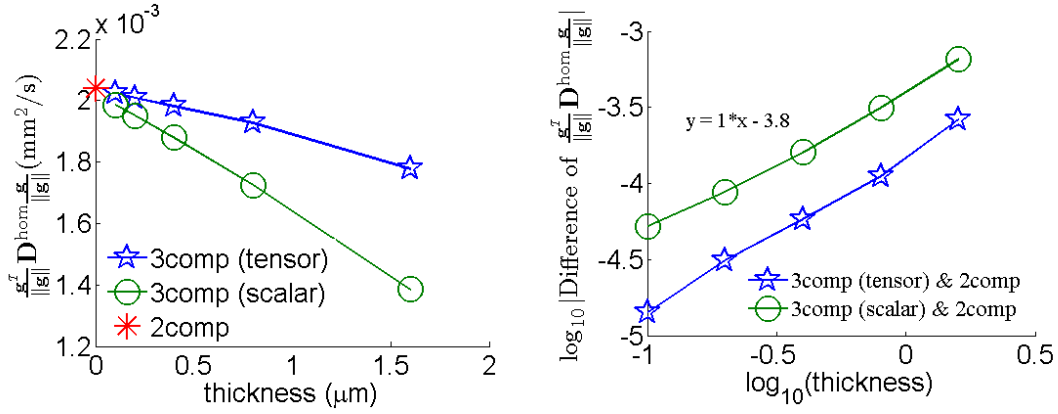

(a) (b)

Figure 3.9: Comparison between $\frac{\mathbf{g}^T}{\|\mathbf{g}\|}\mathbf{D}^{\text{hom}}\frac{\mathbf{g}}{\|\mathbf{g}\|}$, for $\mathbf{g}/\|\mathbf{g}\| = [1,0,0]$ of three-compartment model (3.5a) and two-compartment (3.5b) model for $\kappa = 5\cdot 10^{-5}\frac{\text{m}}{\text{s}}$. As η tends to 0, the $\frac{\mathbf{g}^T}{\|\mathbf{g}\|}\mathbf{D}^{\text{hom}}\frac{\mathbf{g}}{\|\mathbf{g}\|}$ of the three-compartment model approaches that of the two-compartment model (3.9a). The $\log_{10}$ scale of the difference shows that $\frac{\mathbf{g}^T}{\|\mathbf{g}\|}\mathbf{D}^{\text{hom}}\frac{\mathbf{g}}{\|\mathbf{g}\|}$ for both three-compartment models linearly approaches the two-compartment model but the anisotropic model is closer to the two-compartment than the isotropic one (3.9b).

3.3 Validation of Kärger model of the dMRI signal

3.3.1 The Kärger model

The Kärger model starts with the following macroscopic description of two-compartment diffusion [32]. For a two-compartment system made up of the intra- and the extra-cellular compartments, the set of coupled PDEs governing the concentrations, $u^e(\mathbf{r},t), u^c(\mathbf{r},t)$ in the compartments,

$$\frac{\partial u^e(\mathbf{r},t)}{\partial t} = \nabla\cdot\overline{D}^e\nabla u^e(\mathbf{r},t) - \frac{1}{\tau^e}u^e(\mathbf{r},t) + \frac{1}{\tau^c}u^c(\mathbf{r},t), \tag{3.10}$$

$$\frac{\partial u^c(\mathbf{r},t)}{\partial t} = \nabla\cdot\overline{D}^c\nabla u^c(\mathbf{r},t) - \frac{1}{\tau^c}u^c(\mathbf{r},t) + \frac{1}{\tau^e}u^e(\mathbf{r},t). \tag{3.11}$$

In Eqs. (3.10, 3.11) the first term on the right hand side is due to the assumption that the self-diffusion in compartment l is Gaussian with the "effective" diffusion coefficient $\overline{D}^l$. The exchange between the two compartments is effectively accounted for by the other two terms.

The four parameters in the above equations are what we call in this section the "effective" extra-cellular diffusion coefficient $\overline{D}^e$, the "effective" intra-cellular diffusion coefficient $\overline{D}^c$, the effective intra-cellular residence time τ^c, and the effective extra-cellular residence time τ^e. The coupled PDEs in Eqs. (3.10, 3.11) are complemented

by the initial conditions:

$$u^l(\mathbf{r},0) = \rho^l\,\bar{\delta}(\mathbf{r}),\ l = c,e, \tag{3.12}$$

where ρ^l is the relative number of molecules in region l, and $\bar{\delta}(\mathbf{r})$ is the Dirac delta distribution. To conserve mass we have the additional condition:

$$\rho^c\tau^e = \rho^e\tau^c. \tag{3.13}$$

If the equilibrium concentrations in the two compartments are the same, then

$$\frac{\rho^e}{\rho^c} = \frac{v^e}{v^c}, \tag{3.14}$$

where v^j is the volume fraction of compartment j.

Using Eqs. (3.10, 3.11), one can get the dMRI signal in the narrow pulse approximation ($\delta \ll \Delta$), The separate signals due to contributions from compartments c and e are

$$S^l(\mathbf{g},t) \approx \int\limits_{\mathbf{r}\in\mathbb{R}^3} \exp\Big(I\,\gamma\,\delta\,\mathbf{g}\cdot\mathbf{r}\Big)\,u^l(\mathbf{r},t)\,d\mathbf{r}, \quad l = c,e, \tag{3.15}$$

where u^l is the solution of the diffusion problem in Eqs. (3.10, 3.11). Multiplying Eq. (3.10) and Eq. (3.11) by $\exp\Big(I\,\gamma\,\delta\,\mathbf{g}\cdot\mathbf{r}\Big)$, taking the integral and applying the Green's identity, the Kärger equations for the two-compartmental signals are obtained as following:

$$\frac{dS^e(\mathbf{g},t)}{dt} = -\overline{D}^e\gamma^2\|\mathbf{g}\|^2\delta^2 S^e(\mathbf{g},t) - \frac{1}{\tau^e}S^e(\mathbf{g},t) + \frac{1}{\tau^c}S^c(\mathbf{g},t), \tag{3.16}$$

$$\frac{dS^c(\mathbf{g},t)}{dt} = -\overline{D}^c\gamma^2\|\mathbf{g}\|^2\delta^2 S^c(\mathbf{g},t) - \frac{1}{\tau^c}S^c(\mathbf{g},t) + \frac{1}{\tau^e}S^e(\mathbf{g},t), \tag{3.17}$$

subject to initial conditions:

$$S^e(\mathbf{g},0) = v^e, \tag{3.18}$$

$$S^c(\mathbf{g},0) = v^c, \tag{3.19}$$

with v^j being the volume fractions. The solution to Eqs. (3.16-3.19) is

$$\begin{aligned} S(\mathbf{g},t) &= S^e(\mathbf{g},t) + S^e(\mathbf{g},t) \\ &= v^f(\mathbf{g})\exp\left(-D^f(\mathbf{g})\gamma^2\,\|\mathbf{g}\|^2\delta^2\,t\right) + v^s(\mathbf{g})\exp\left(-D^s(\mathbf{g})\gamma^2\,\|\mathbf{g}\|^2\delta^2\,t\right), \end{aligned} \tag{3.20}$$

where

$$\begin{aligned} D^{f,s}(\mathbf{q}) = \frac{1}{2}&\left(\overline{D}^e + \overline{D}^c + \frac{1}{\gamma^2\,\|\mathbf{g}\|^2\delta^2}\left(\frac{1}{\tau^e}+\frac{1}{\tau^c}\right)\right) \\ &\pm\frac{1}{2}\sqrt{\left(\overline{D}^e - \overline{D}^c + \frac{1}{\gamma^2\,\|\mathbf{g}\|^2\delta^2}\left(\frac{1}{\tau^e}-\frac{1}{\tau^c}\right)\right)^2 + \frac{4}{\gamma^4\,\|\mathbf{g}\|^4\delta^4\tau^e\tau^c}} \end{aligned} \tag{3.21}$$

$$v^f(\mathbf{g}) = \frac{1}{D^f(\mathbf{g}) - D^s(\mathbf{g})} \left(v^e \overline{D}^e + v^c \overline{D}^c - D^s(\mathbf{g}) \right), \tag{3.22}$$

$$v^s(\mathbf{g}) = 1 - v^f(\mathbf{g}). \tag{3.23}$$

The residence times τ^e and τ^c can be numerically computed by Eq. (3.16) and Eq. (3.17) with $\mathbf{g} = 0$. What we need are $\frac{dS^e(0,t)}{dt}$, $\frac{dS^c(0,t)}{dt}$, $S^e(0,t)$ and $S^c(0,t)$. They can be found by putting some initial mass inside one of two compartments and leaving the other empty. Then, the diffusion equation will be solved in this domain to give needed values.

There also exists an analytical expression for τ^c for the low permeability κ [32]

$$\tau^c \approx \frac{V}{A\,\kappa}, \tag{3.24}$$

where $\frac{V}{A}$ the volume to surface ratio of the intra-cellular compartment.

Both effective diffusion coefficients $\overline{D}^e$ and $\overline{D}^c$ are computed by solving the Laplace equation (1.31) with conditions (1.24, 1.25, 1.32, 1.33) and using Eq. (1.34) for no-exchange case ($\kappa = 0$) [13].

3.3.2 Simulations

We performed simulations on a cube $\Omega = [-2.5\mu\text{m}, 2.5\mu\text{m}]^3$ containing one spherical cell of radius $R = 2.45\mu$m (Figure 3.10a) for ten $b-$values ranging between 0 and 4000s/mm^2. To mimic diffusion in unbounded domain, the computational domain is repeated periodically in all three directions by imposing the pseudo-periodic boundary conditions (1.27, 1.28). The Laplace PDE gives $\overline{D}^e = 2.32 \cdot 10^{-3}\text{mm}^2/\text{s}$ and $\overline{D}^e = 0$. For this simple case, the residence time for sphere is analytically computed by Eq. (3.24). We fix $\delta = 5$ms for all simulations and the same intrinsic diffusion coefficient $D = 3 \cdot 10^{-3}\text{mm}^2/\text{s}$ was set for both compartments.

First, we see that for a fixed Δ, the model works better for lower permeabilities. Figure 3.10b shows the comparison between simulated signals and the signals obtained from the Kärger model for three permeabilities at $\Delta = 40$ms. It shows that the two signals lie between the signal in the no-exchange case

$$S^{NO\text{-}EX} = v^e \exp(-b\,\overline{D}^e) + v^c \exp(-b\,\overline{D}^c), \tag{3.25}$$

and the signal in the fast-exchange case

$$S^{FAST\text{-}EX} = \exp\Big(-b\,(v^e \overline{D}^e + v^c \overline{D}^c)\Big). \tag{3.26}$$

The maximum of the relative difference between two signals versus ten $b-$values is 23%, 7% and 5% for three permeabilities $\kappa = 5 \cdot 10^{-5}, 10^{-5}$ and $10^{-6}\text{mm}^2/\text{s}$ respectively.

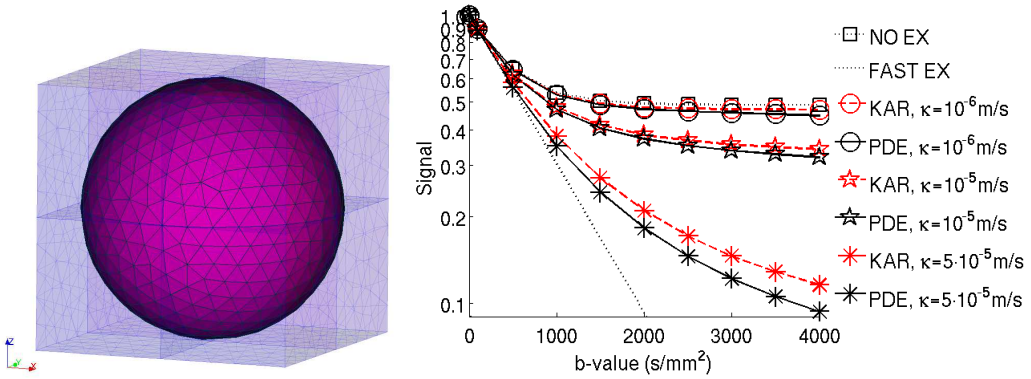

(a) (b)

Figure 3.10: Computational domain $\Omega = [-2.5\mu\text{m}, 2.5\mu\text{m}]^3$ contains one spherical cell of radius $R = 2.45\mu$m (3.10a) and simulated results for three different permeabilities $\kappa = 5 \cdot 10^{-5}, 10^{-5}$ and 10^{-6}mm^2/s at $\Delta = 40$ms (3.10b).

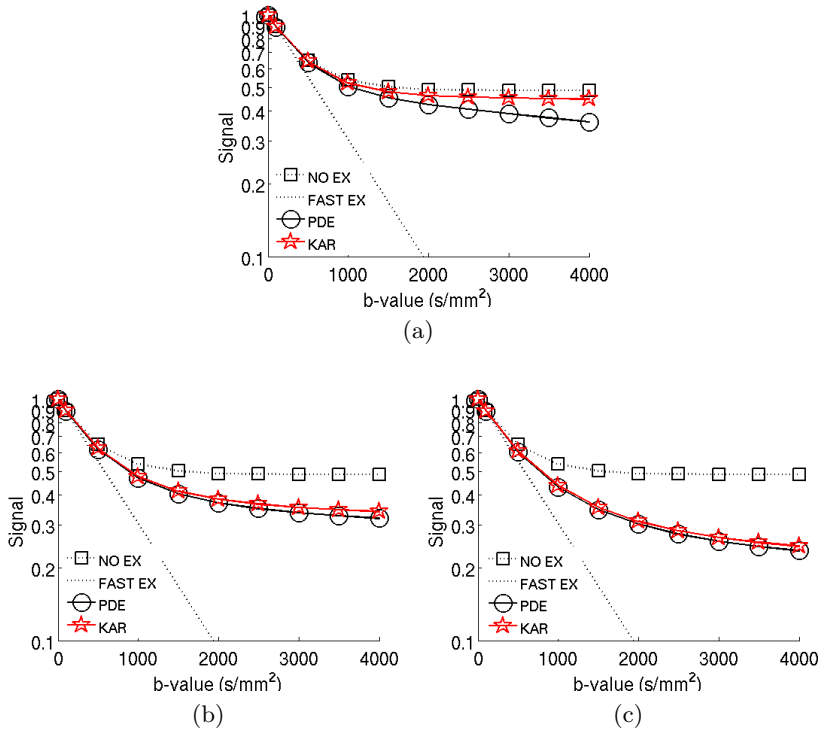

(a)

(b) (c)

Figure 3.11: The Kärger model works better for larger Δ corresponding to the narrow pulse gradients. The maximum of relative difference between two signals is 28% for $\Delta = 10$ms (3.11a), 7% for $\Delta = 40$ms (3.11b) and 4% for $\Delta = 80$ms (3.11c).

For permeability $\kappa = 10^{-5}$m/s, we do simulations for four diffusion times $\Delta = 5, 10, 40$ and 80ms (Figure 3.11). The model works better for larger Δ corresponding to the narrow pulse gradients. The maximum of relative difference between two signals is 28% for $\Delta = 10$ms, 7% for $\Delta = 40$ms and 4% for $\Delta = 80$ms.

3.4 Conclusion

First, the time-dependent ADC converges to $\frac{\mathbf{g}^T}{\|\mathbf{g}\|}\mathbf{D}^{\text{hom}}\frac{\mathbf{g}}{\|\mathbf{g}\|}$ in both isotropic and anisotropic diffusion and general shapes. Because the convergence curve looks linear versus Δ^{-1} for long diffusion time, we hope to obtain the $\frac{\mathbf{g}^T}{\|\mathbf{g}\|}\mathbf{D}^{\text{hom}}\frac{\mathbf{g}}{\|\mathbf{g}\|}$ from experimentally measured ADCs by interpolation. We also expect that the analysis of the effective diffusion tensor can reveal some useful information about the biological structures because it is easier and faster to analyze than the time-dependent ADC computed after solving the Bloch-Torrey equation.

Second, we showed that the two-compartment model can be used to approximate the signal from three-compartment models with isotropic diffusion and anisotropic diffusion in the membrane layer. The signals of both three-compartment models linearly converge to that of the two-compartment model. The two-compartment model gives a better approximation to the anisotropic case than the isotropic case.

Finally, we used the FEM-RKC code to validate the macroscopic Kärger model for narrow pulse gradient. It shows that the Kärger model works better at lower permeability and longer diffusion times Δ.

Chapter 4

Modeling the diffusion magnetic resonance imaging signal inside neurons

Summary Studying the dMRI signal arising from isolated neurons can provide insight into how the geometrical structure of neurons influences the measured signal. We formulate the Bloch-Torrey partial differential equation (PDE) inside an isolated neuron, under no water exchange condition with the extra-cellular space, and show how to reduce the 3D simulation in the full neuron to a 3D simulation in the soma and 1D simulations in the neurites. The cross-sectional area of each neurite segment is taken into account to allow working with neurons in which the neurite segments may have different radii. The transverse diffusion inside each cylindrical segment is also analytically added to give accurate results over a wide range of diffusion times. We show that this approach is computationally much faster than a full 3D simulation. The proposed method is used to validate an earlier published formula about the ADC of the dMRI from neurites. From the dMRI signal of neurites trees, we can invert the ADC formula to get back the average length of the neurite trees. This result indicates a potential way to extract useful information about neurites tree structure. Finally, we also derive the upper and lower bounds for the signal and for the related ADC.

4.1 Introduction

In a complex medium such as brain tissue, it is difficult to explicitly link the dMRI signal to biological parameters such as shape, orientation and volume fraction of neurons or, more generally, tissue micro-structure. The dMRI signal arising from an isolated neuron and its dependence on the geometrical structure are still poorly understood. A number of experimental and numerical works have been devoted to this problem [2, 7, 11, 18, 29–31, 34, 62, 65, 72]. One of the first analytical models of water diffusion in neural tissue was proposed by Szafer *et al.* [72]. Modeling a

tissue as a regular lattice of cylinders, they derived approximate expressions for the apparent diffusion coefficients (ADCs) at long times. Stanisz *et al.* presented an analytical model of restricted diffusion in the bovine optic nerve, in which prolate ellipsoids (axons) and spheres (glial cells) were surrounded by partially permeable membranes [65]. Water exchange was accounted for by a modified Kärger approach. The derived analytical formulas for the dMRI signal were fitted to experimental data for bovine optic nerve. Grant *et al.* reported experimental evidence of multicomponent diffusion in isolated neurons [18]. The usual interpretation of the fractions of fast and slow apparent diffusion components as the volume fractions of extra-cellular and intra-cellular spaces has been questioned by Chin and co-workers [11]. Using a finite difference diffusion simulation model on the basis of optical images from sectioned rat spinal cord, they showed that the observed multicomponent diffusion behavior is caused by motional restriction and limited inter-compartmental water exchange. Assaf *et al.* considered infinitely long isolated cylinders to model brain white matter, with two contributions to the dMRI signal coming from hindered diffusion outside cylinders and restricted diffusion inside cylinders [2]. Kroenke *et al.* explained non-monoexponential dMRI signal decay by restricted diffusion in an ensemble of differently oriented neuronal fibers [34]. Sen and Basser presented a simplified, but self-consistent modeling framework for predicting the long-time apparent diffusion coefficients of water parallel and perpendicular to a "pack" of identical thick-walled (myelinated) cylindrical tubes (axons) arranged periodically in a regular lattice and immersed in an outer medium [62]. The role of water exchange between several "layers" and towards the outer space was also studied in [16, 21, 53, 55]. Jespersen *et al.* proposed a simplified model of neural cytoarchitecture intended to capture the essential features important for water diffusion as measured by NMR [31] (see also [7]). In their model, two contributions to the dMRI signal come from (i) the dendrites and axons, which are modeled as infinitely long isolated cylinders with two diffusion coefficients (parallel and perpendicular to the cylindrical axis), and (ii) water diffusion within and across all other structures (i.e., in the extra-cellular space, neuron soma and glia cells), which is modeled as monoexponential diffusion. This model was confronted to dMRI measurements in a formalin-fixed baboon brain and shown to be able to provide an estimate of dendrite density. The model predictions of neurite density in rats have been successfully compared to optical myelin staining intensity and stereological estimation of neurite volume fraction using electron microscopy [30]. Recently, water diffusion anisotropy measurements have been directly related to characteristics of neuronal morphology [29]. Budde and Frank introduced a biophysical model of neurite beading (i.e., focal enlargement and constriction) and showed that this mechanism was sufficient to substantially decrease ADC and thus rationalize experimental findings after ischemic stroke [6]. Some other theoretical models and concepts of brain dMRI have been reviewed in [79].

In most earlier works, the neurites were modeled by infinitely long *isolated* cylinders (or prolite ellipsoids), meaning the morphological structure (the dendrite trees) was ignored. In fact, neurons are made of a neuronal body called the soma to which are attached long protrusions called neurites (axons and dendrites) and the dendrites

have a tree structure (Fig. 4.1). The size of the soma is on the order of 10μm, the diameter of the dendrite segments can range from a few μm to less than half a μm, and the total length of all the dendrite segments is on the order of several mm [64, 68].

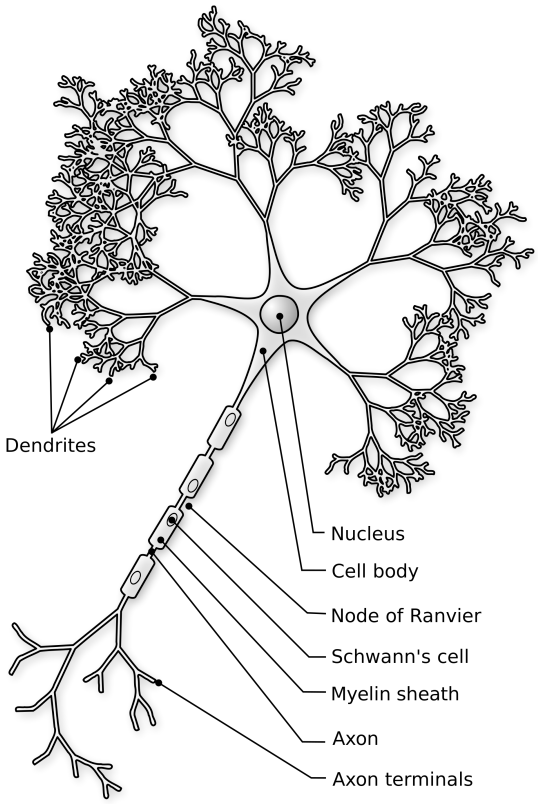

Figure 4.1: Image from Wikimedia Commons. Description: *Biological neuron schema*. Source: http://commons.wikimedia.org/wiki/File:Neuron-figure.svg, Author: Nicolas.Rougier

In this chapter, we study the dMRI signal arising from the interior of a single neuron, under the common assumption of no water exchange between the neuron and the extra-cellular space. We consider the full 3D Bloch-Torrey PDE model on a neuron, comprising of a spherical soma with attached axon and dendrite trees, and formulate an approximate model in which 3D computations in the neurites are replaced by 1D computations. This greatly reduces the computational time and allows one to simulate a large number of neuron configurations. We also simulate the exchange between the soma and the neurites and conclude that the exchange is usually small enough that the soma and the neurites can be simulated separately (as isolated subdomains), which provides numerical supports for the various neuron signal models proposed in the literature. The proposed models are used to simulate

and analyze the dMRI signal from neurites trees. From the dMRI signal of neurites trees, we can invert the ADC formula to get back the average length of the neurite trees. Finally, we derive two analytical upper and lower bounds of the signal and related ADC for neurites trees.

4.2 The Bloch-Torrey PDE in a neuron

Let a neuron be defined by $\Omega = \mathcal{A} \cup \mathcal{N}$, an open set in $\mathbb{R}^3$, that is the union of the soma $\mathcal{A}$ and the attached neurites $\mathcal{N}$. The water proton magnetization $M^{3D}(\mathbf{r}, t)$ satisfies the Bloch-Torrey PDE:

$$\frac{\partial}{\partial t} M^{3D}(\mathbf{r}, t) = -I\gamma f(t)\, \mathbf{g} \cdot \mathbf{r}\, M^{3D}(\mathbf{r}, t) + \nabla \cdot \Big(D \nabla M^{3D}(\mathbf{r}, t) \Big), \quad \mathbf{r} \in \Omega. \tag{4.1}$$

Neglecting water exchange with the extra-cellular space yields homogeneous Neumann boundary condition:

$$D \nabla M^{3D}(\mathbf{r}, t) \cdot \mathbf{n}(\mathbf{r}) = 0, \quad \mathbf{r} \in \partial\Omega. \tag{4.2}$$

Assuming a uniform excitation of the magnetization in the imaging voxel, the initial condition is:

$$M^{3D}(\mathbf{r}, 0) = 1. \tag{4.3}$$

The dMRI signal, which is measured at the echo time $t = TE \geq \Delta + \delta$, is then

$$S^{3D}(b) := \frac{1}{|\Omega|} \int_{\mathbf{r} \in \Omega} M^{3D}(\mathbf{r}, TE)\, d\mathbf{r}. \tag{4.4}$$

If the exchange between the soma and the attached neurites is neglected the Bloch-Torrey PDE can be formulated separately in each domain. On the soma $\mathcal{A}$, the PDE is

$$\frac{\partial}{\partial t} M^{3D,\mathcal{A}}(\mathbf{r}, t) = -I\gamma f(t) \mathbf{g} \cdot \mathbf{r}\, M^{3D,\mathcal{A}}(\mathbf{r}, t) + \nabla \cdot (D \nabla M^{3D,\mathcal{A}}(\mathbf{r}, t)), \quad \mathbf{r} \in \mathcal{A}, \tag{4.5}$$

with boundary conditions

$$D \nabla M^{3D,\mathcal{A}}(\mathbf{r}, t) \cdot \mathbf{n}(\mathbf{r}) = 0, \quad \mathbf{r} \in \partial\mathcal{A}. \tag{4.6}$$

The initial condition is

$$M^{3D,\mathcal{A}}(\mathbf{r}, 0) = 1. \tag{4.7}$$

The dMRI signal is

$$S^{3D,\mathcal{A}}(b) = \frac{1}{|\mathcal{A}|} \int_{\mathbf{r} \in \mathcal{A}} M^{3D,\mathcal{A}}(\mathbf{r}, TE)\, d\mathbf{r} \tag{4.8}$$

Similarly, the PDE on neurites $\mathcal{N}$ is

$$\frac{\partial}{\partial t}M^{3D,\mathcal{N}}(\mathbf{r},t) = -I\gamma f(t)\mathbf{g}\cdot\mathbf{r}\, M^{3D,\mathcal{N}}(\mathbf{r},t) + \nabla\cdot(D\nabla M^{3D,\mathcal{N}}(\mathbf{r},t)), \quad \mathbf{r}\in\mathcal{N}, \tag{4.9}$$

with boundary conditions

$$D\nabla M^{3D,\mathcal{N}}(\mathbf{r},t)\cdot\mathbf{n}(\mathbf{r}) = 0, \quad \mathbf{r}\in\partial\mathcal{N}. \tag{4.10}$$

The initial condition is

$$M^{3D,\mathcal{N}}(\mathbf{r},0) = 1. \tag{4.11}$$

The dMRI signal for neurites is

$$S^{3D,\mathcal{N}}(b) = \frac{1}{|\mathcal{N}|}\int_{\mathbf{r}\in\mathcal{N}} M^{3D,\mathcal{N}}(\mathbf{r},TE)\, d\mathbf{r}. \tag{4.12}$$

The dMRI signal for the disconnected neuron is

$$S^{3D|3D}(b) = \frac{1}{|\mathcal{A}|+|\mathcal{N}|}\left(\int_{\mathbf{r}\in\mathcal{A}} M^{3D,\mathcal{A}}(\mathbf{r},TE)\, d\mathbf{r} + \int_{\mathbf{r}\in\mathcal{N}} M^{3D,\mathcal{N}}(\mathbf{r},TE)\, d\mathbf{r}\right). \tag{4.13}$$

We emphasize that there is no connection between neurites tree $\mathcal{N}$ and soma $\mathcal{A}$. The numerical method to solve these 3D problems was proposed in chapter 2.

4.3 1D model of neurites

In this section we formulate an approximate model of the dMRI signal in a neurites tree that only involves 1D computations. However, the radii of the neurite segments and the transverse diffusion are taken into account to give better approximations for thick neurites and more realistic situations where the neurite segments may have different radii. At this stage, we neglect the soma, i.e. we assume the domain $\Omega = \mathcal{N}$ only contains the neurites.

4.3.1 Problem formulation

To simplify the presentation, a neurites tree is represented as the union of straight cylindrical segments, $\mathcal{N} = \bigcup_{k=1}^{\mathcal{K}} \mathcal{B}_k$, where $\mathcal{K}$ is the number of cylindrical segments, $\mathcal{B}_k = \mathcal{T}_k \times \mathcal{O}_k$, $\mathcal{T}_k$ is a 1D line segment of length ℓ_k, parallel to the unit vector $\mathbf{w}_k$, and $\mathcal{O}_k$ is the disk of radius r_k perpendicular to $\mathbf{w}_k$ (see Figures 4.2a and 4.2b).

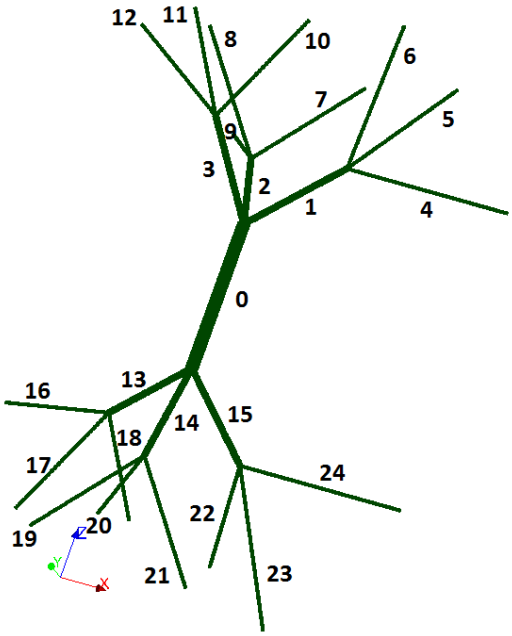

(a)

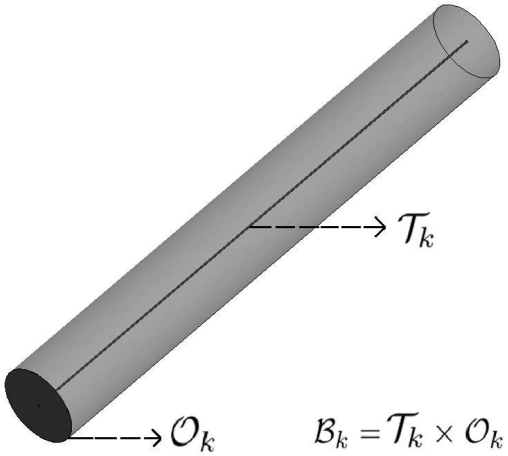

(b)

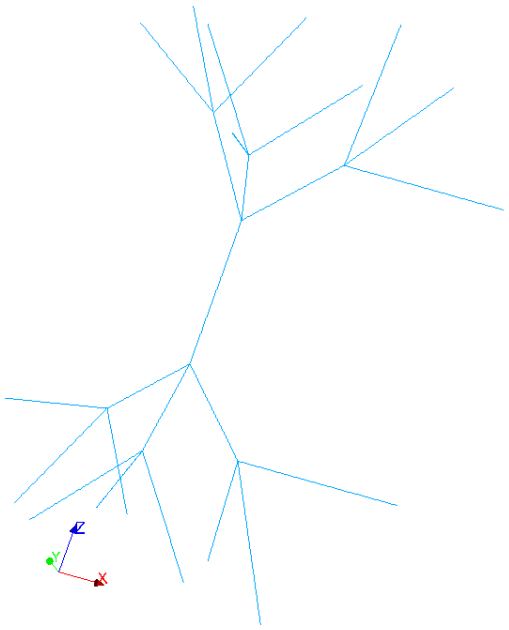

(c)

Figure 4.2: 3D domain of a neurites tree (4.2a), cylindrical segment $\mathcal{B}_k = \mathcal{T}_k \times \mathcal{O}_k$ (4.2b) and corresponding 1D domain (4.2c).

We now formulate an approximation to the full 3D model of the neurite tree $\mathcal{N}$, in which we replace the 3D PDE in the neurites tree by a 1D PDE on the union of

the *linked* line segments $\mathcal{N}^{1D} = \bigcup_{k=1}^{\mathcal{K}} \mathcal{T}_k$. See Fig. 4.2c.

Let $\mathcal{T}_k = \mathbf{p}_k + s\mathbf{w}_k$, $s \in [0, \ell_k]$, be the natural parametrization of the line segment $\mathcal{T}_k$, $\mathbf{p}_k$ being one endpoint of the segment. We define the 1D magnetization on the segment $\mathcal{T}_k$ as the average value of the magnetization over its transverse cross-section $\mathcal{O}_k$:

$$M_k^{1D,\mathcal{N}}(s,t) := \frac{1}{|\mathcal{O}_k|} \int_{(\mathbf{p}_k + s\mathbf{w}_k)\times\mathcal{O}_k} M^{3D,\mathcal{N}}(\mathbf{r},t)d\mathbf{r}, \tag{4.14}$$

where $|\mathcal{O}_k| = \pi r_k^2$ is the surface area of the cross-section. It is easy to show that $M_k^{1D,\mathcal{N}}(s,t)$ satisfies the 1D Bloch-Torrey PDE:

$$\frac{\partial}{\partial t} M_k^{1D,\mathcal{N}}(s,t) = -I\gamma\, f(t)\, \mathbf{g}\cdot(\mathbf{p}_k + s\mathbf{w}_k)\, M_k^{1D,\mathcal{N}}(s,t) + D\frac{\partial^2}{\partial s^2} M_k^{1D,\mathcal{N}}(s,t). \tag{4.15}$$

To be consistent with the full 3D model, two conditions have to be imposed at any intersection point $\mathbf{r}$ of two (or several) line segments. The first condition is the continuity of the magnetization derived from Eq. (4.14):

$$M_k^{1D,\mathcal{N}}(s_k,t) = M_{k'}^{1D,\mathcal{N}}(s_{k'},t), \tag{4.16}$$

for all $k, k' \in \mathcal{K}\,(k \neq k')$ such that $\mathbf{p}_k + s_k\mathbf{w}_k = \mathbf{p}_{k'} + s_{k'}\mathbf{w}_{k'} = \mathbf{r}$.

The second condition is the Kirchhoff law ensuring the conservation of flux. Since the cylinder segments may have different radii, the cross-sectional area of each cylinder $|\mathcal{O}_k|$ needs to be taken into account:

$$\sum_k |\mathcal{O}_k|\, D\frac{\partial}{\partial s'} M_k^{1D,\mathcal{N}}(s_k,t) = 0, \tag{4.17}$$

such that $\mathbf{p}_k + s_k\mathbf{w}_k = \mathbf{r}$, and $s' = s$ if $\mathbf{r} = \mathbf{p}_k$ is the starting point of the segment, $s' = -s$ otherwise.

For the 1D model of neurites, Eqs. (4.3) and (4.14) imply the initial condition

$$M_k^{1D,\mathcal{N}}(s,0) = 1, \quad k = 1 \ldots \mathcal{K}.$$

The Neumann boundary condition in Eq. (4.2) becomes

$$D\frac{\partial}{\partial s} M_k^{1D,\mathcal{N}}(s_k,t) = 0, \tag{4.18}$$

where $\mathbf{p}_k + s_k\mathbf{w}_k$ is an ending point of $\mathcal{N}^{1D}$ for some segment k.

Finally, one gets the dMRI signal for the 1D model according to Eqs. (4.4) and (4.14)

$$S^{1D,\mathcal{N}}(b) = \frac{1}{\sum_k |\mathcal{O}_k|\,\ell_k} \left(\sum_k |\mathcal{O}_k| \int_0^{\ell_k} M_k^{1D,\mathcal{N}}(s,TE)\, ds \right), \tag{4.19}$$

where both sums are taken over all segments.

Eq. (4.19) gives a good approximation of 3D neurites when the transverse diffusion on cylinder segments can be neglected. The contribution of transverse diffusion to the signal can be included into Eq. (4.19) to get a more accurate approximation:

$$S_{tr}^{1D,\mathcal{N}}(b) = \frac{1}{\sum_k |\mathcal{O}_k|\,\ell_k}\left(\sum_k |\mathcal{O}_k|\,S_k^{tr}(b\,\sin^2\theta_k)\int_0^{\ell_k} M_k^{1D,\mathcal{N}}(s,TE)\,ds\right), \tag{4.20}$$

where θ_k is the angle between the gradient direction $\mathbf{g}/\|\mathbf{g}\|$ and $\mathcal{T}_k$. Here, $S_k^{tr}(b)$ is the dMRI signal for the transverse diffusion inside the k^{th} cylinder which can be either approximated by an analytical formula in the frame of the Gaussian phase approximation (see Section 1.6.3), or computed rapidly and very accurately within the matrix formalism (see the review [19] and references therein).

4.3.2 Linear basis functions for 3D line segments

To solve the Bloch-Torrey PDE on linked 1D segments, we need to implement the finite elements method in a 1D tree of segments. In 1D, the linear basis functions for a segment $[x_1, x_2]$ are well known:

$$\begin{aligned}\varphi_1(x) &= -\frac{1}{x_{12}}(x - x_2),\\ \varphi_2(x) &= \frac{1}{x_{12}}(x - x_1),\end{aligned} \tag{4.21}$$

where $x_{12} = x_2 - x_1$.

We will design the basis functions for a segment $\bar{A}_1\bar{A}_2$ in 3D space, $\bar{A}_1(\bar{x}_1, \bar{y}_1, \bar{z}_1)$, $\bar{A}_2(\bar{x}_2, \bar{y}_2, \bar{z}_2)$. For this purpose, we rotate the basis functions $\varphi_1(x)$ and $\varphi_2(x)$ from x-axis to $\bar{A}_1\bar{A}_2$. We denote $\vec{p} = (x_2 - x_1, y_2 - y_1, z_2 - z_1)$ a direction vector of $\bar{A}_1\bar{A}_2$, $\vec{p}_x = (x_2 - x_1, 0, 0)$ a projection of $\vec{p}$ on x-axis.

• If $x_2 \neq x_1$, we can compute $\vec{n}$ and θ representing the axis and the angle of the rotation respectively, $\vec{n} = \vec{p}_x \times \vec{p}$. The formula for this rotation is then $\bar{X} = R\,X$, where R is the rotation matrix,

$$R = \begin{bmatrix} \cos\theta + n_x^2(1-\cos\theta) & n_x n_y(1-\cos\theta) - n_z\sin\theta & n_x n_z(1-\cos\theta) + n_y\sin\theta \\ n_x n_y(1-\cos\theta) + n_z\sin\theta & \cos\theta + n_y^2(1-\cos\theta) & n_y n_z(1-\cos\theta) - n_x\sin\theta \\ n_x n_z(1-\cos\theta) - n_y\sin\theta & n_y n_z(1-\cos\theta) + n_x\sin\theta & \cos\theta + n_z^2(1-\cos\theta) \end{bmatrix} \tag{4.22}$$

$X^T = (x, y, z)$ represents old coordinates, and $\bar{X}^T = (\bar{x}, \bar{y}, \bar{z})$ is new coordinates. From a straightforward computation, we can obtain the basis functions for $\bar{A}_1\bar{A}_2$ as following:

$$\begin{aligned}\varphi_1(\bar{x}, \bar{y}, \bar{z}) &= \theta_x(\bar{x} - \bar{x}_2) + \theta_y(\bar{y} - \bar{y}_2) + \theta_z(\bar{z} - \bar{z}_2),\\ \varphi_2(\bar{x}, \bar{y}, \bar{z}) &= -\theta_x(\bar{x} - \bar{x}_1) - \theta_y(\bar{y} - \bar{y}_1) - \theta_z(\bar{z} - \bar{z}_1),\end{aligned} \tag{4.23}$$

where

$$\theta_x = \frac{1}{A}\Big((n_z^2 + n_y^2)(-1+\cos\theta)+1\Big),$$
$$\theta_y = \frac{-1}{A}\Big(-n_z\sin\theta + n_x\, n_y\,(-1+\cos\theta)\Big),$$
$$\theta_z = \frac{-1}{A}\Big(n_x\, n_z\,(-1+\cos\theta) + n_y\sin\theta\Big),$$

and

$$A = -\bar{x}_{12}\bigg(\Big(n_z^2+n_y^2\Big)\Big(\cos\theta-1\Big)+1\bigg)+\bar{y}_{12}\bigg(n_x\, n_y\,\Big(\cos\theta-1\Big)-n_z\sin\theta\bigg)$$
$$+\bar{z}_{12}\bigg(n_x\, n_z\,\Big(\cos\theta-1\Big)+n_y\sin\theta\bigg).$$

• In the singular case where $x_2 = x_1$, we consider that $\theta = \dfrac{\pi}{2}$ and $\vec{n} = \vec{e}_1 \times \vec{p}$, $\vec{e}_1 = (1,0,0)$.

4.3.3 Simulations

We simulate the dMRI signal in a neurites tree consisting of 25 segments shown in Fig. 4.2a. Information about the neurites tree is summarized in Table 4.1. We emphasize that in the neurites tree, the cylindrical segments have different radii: $r_k \in \{1,2,4\mu\text{m}\}$ and different lengths: $75\mu\text{m} \leq \ell_k \leq 112.5\mu\text{m}$.

Table 4.1: Description of 3D neurites tree in Fig. 4.2a used for the simulation: α_k and β_k indicate the angle between the cylinder axis $\mathcal{T}_k$ and the trunk [0,0,1], and between $\mathcal{T}_k$ and gradient direction $\mathbf{g}/\|\mathbf{g}\| = [1,1,1]/\sqrt{3}$.

k	ℓ_k (μm)	r_k (μm)	α_k	β_k	k	ℓ_k (μm)	r_k (μm)	α_k	β_k
0	100	4	0.0	54.7	13	75.0	2	135.0	105.0
1	75.0	2	45.0	35.3	14	75.0	2	135.0	165.0
2	75.0	2	45.0	98.6	15	75.0	2	135.0	90.0
3	75.0	2	45.0	56.1	16	88.9	1	108.4	89.0
4	112.5	1	90.0	54.7	17	88.9	1	142.2	160.0
5	112.5	1	41.4	77.1	18	88.9	1	142.2	88.5
6	112.5	1	41.4	21.4	19	88.9	1	142.2	125.9
7	88.9	1	37.8	54.1	20	88.9	1	108.4	158.6
8	88.9	1	37.8	70.9	19	88.9	1	142.2	109.1
9	88.9	1	71.8	124.4	22	112.5	1	138.6	86.3
10	88.9	1	37.8	20.0	23	112.5	1	138.6	130.0
11	88.9	1	37.8	91.5	24	112.5	1	90.0	54.7
12	88.9	1	71.6	67.5					

Figure 4.3 shows $S^{3D}(b)$, $S^{1D,\mathcal{N}}(b)$ and $S_{tr}^{1D,\mathcal{N}}(b)$ in the gradient direction $\mathbf{g}/\|\mathbf{g}\| = (1,1,1)/\sqrt{3}$ and at three diffusion times: $\Delta = 2.5, 10$ and 100ms.

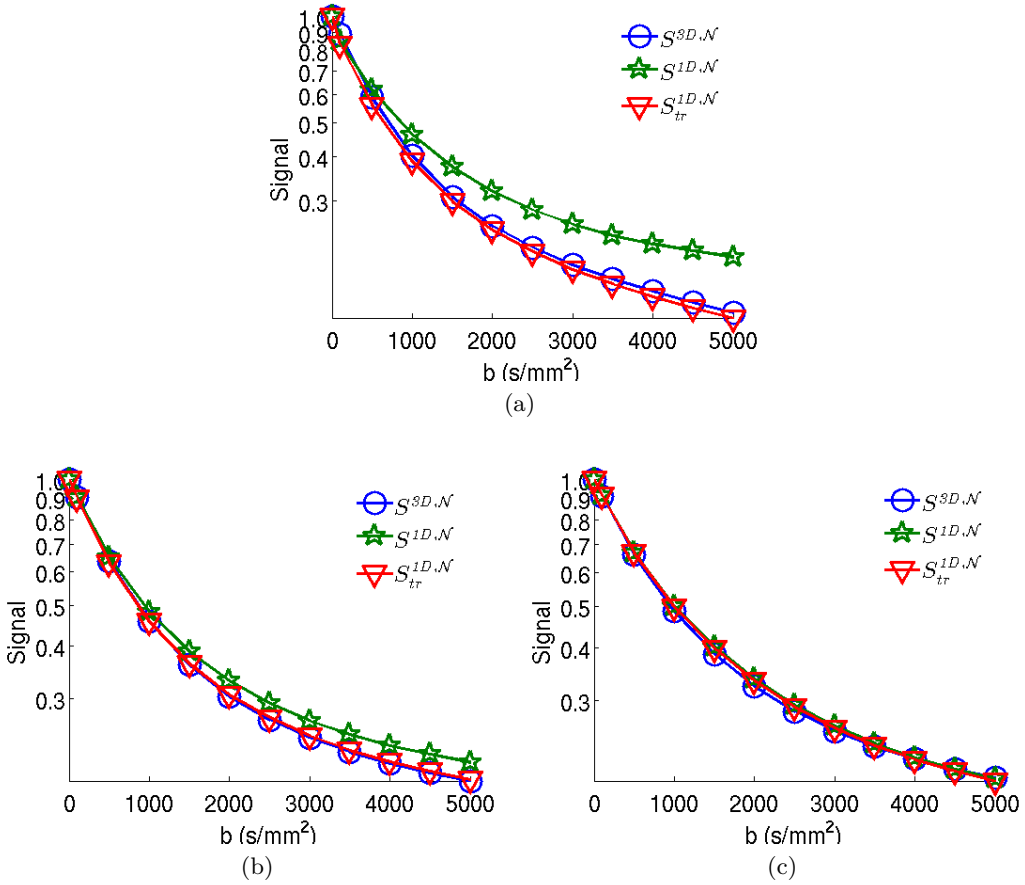

Figure 4.3: The signals from Eqs. (4.12, 4.19, 4.20) for a neurites tree described in Table 4.1 for gradient direction $\mathbf{g}/\|\mathbf{g}\| = (1,1,1)/\sqrt{3}$ and three diffusion times $\Delta = 2.5$ms (Fig. 4.3a), $\Delta = 10$ms (Fig. 4.3b) and $\Delta = 100$ms (Fig. 4.3c). Note that cylindrical segments have different radii.

For short diffusion time ($\Delta = 2.5$ms, Fig. 4.3a), the simulated signal for 1D neurites (green curve with stars) does not give a good approximation to the signal for 3D neurites (blue curve with circles) because the effect of the transverse diffusion is still significant. Accounting for the contribution of the transverse diffusion significantly improves the result (red curve with triangles). For long time diffusion ($\Delta = 100$ms, Fig. 4.3c), the transverse diffusion is irrelevant because the average diffusion distance is much larger than the cylinder radii. In this case, all three curves coincide.

4.4 The "3D+1D" model

We now consider the complete neuron, Ω, composed of the soma, $\mathcal{A}$, and the attached neurites tree, $\mathcal{N}$, such that $\Omega = \mathcal{A} \bigcup \mathcal{N}$. An example of a neuron with a spherical soma attached to two neurite trees is illustrated on Fig. 4.4a. We now

formulate an approximation to the full 3D model by replacing the 3D neurites by 1D neurites (see Sec. 4.3 and Fig. 4.4b).

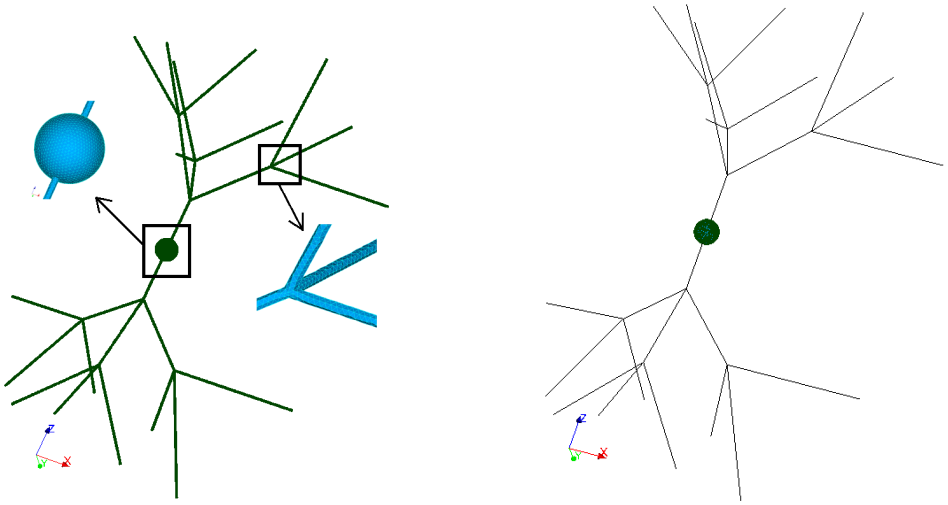

(a) (b)

Figure 4.4: The full "3D" model of a neuron (4.4a) and the reduced "3D+1D" in which the 3D neurites tree is replaced by a 1D neurites tree (4.4b).

Let $\mathcal{I}_k$ be the intersection between the soma $\mathcal{A}$ and the neurite segment $\mathcal{B}_k$ (there may be several of these segments that extend out from the soma) and $\mathcal{I} = \cup_k \mathcal{I}_k$. The Bloch-Torrey PDE applies in both the soma and the neurites:

$$\begin{aligned}
\frac{\partial}{\partial t} M^{3D+1D,\mathcal{A}}(\mathbf{r},t) &= -I\gamma f(t)\mathbf{g}\cdot\mathbf{r}\, M^{3D+1D,\mathcal{A}}(\mathbf{r},t) + \nabla\cdot\left(D\nabla M^{3D+1D,\mathcal{A}}(\mathbf{r},t)\right),\\
\frac{\partial}{\partial t} M_k^{3D+1D,\mathcal{N}}(s,t) &= -I\gamma\, f(t)\,\mathbf{g}\cdot(\mathbf{p}_k + s\mathbf{w}_k)\, M_k^{3D+1D,\mathcal{N}}(s,t) + D\frac{\partial^2}{\partial s^2} M_k^{3D+1D,\mathcal{N}}(s,t),
\end{aligned} \tag{4.24}$$

with interface conditions at the intersections $\mathbf{r}$ between neurite segments:

$$M_k^{3D+1D,\mathcal{N}}(s_k,t) = M_{k'}^{3D+1D,\mathcal{N}}(s_{k'},t), \tag{4.25}$$

$$\sum_k |\mathcal{O}_k|\, D\frac{\partial}{\partial s'} M_k^{3D+1D,\mathcal{N}}(s_k,t) = 0. \tag{4.26}$$

for some k, k' such that $\mathbf{p}_k + s_k\mathbf{w}_k = \mathbf{p}_{k'} + s_{k'}\mathbf{w}_{k'} = \mathbf{r}$.

We assume that no more than one segment extends from one position of soma, i.e. $\mathcal{I}_k \cap \mathcal{I}_{k'} = \varnothing$ for all $k \neq k'$. The continuity of magnetization and the flux conservation at the intersection of the soma and the neurite k are then

$$\frac{1}{|\mathcal{I}_k|}\int_{\mathcal{I}_k} M^{3D+1D,\mathcal{A}}(\mathbf{r},t)d\mathbf{r} = M_k^{3D+1D,\mathcal{N}}(s_k,t), \tag{4.27}$$

$$\frac{1}{|\mathcal{I}_k|}\int_{\mathcal{I}_k} D\nabla M^{3D+1D,\mathcal{A}}(\mathbf{r},t)\cdot\mathbf{n}_k = D\frac{\partial}{\partial s'} M_k^{3D+1D,\mathcal{N}}(s_k,t), \tag{4.28}$$

such that s_k satisfies $\mathbf{p}_k + s_k\mathbf{w}_k = \mathcal{I}_k \cap \mathcal{T}_k$, where $\mathbf{n}_k$, parallel to $\mathcal{T}_k$, is also the normal vector pointing outward the soma at $\mathcal{I}_k$, $s' = s$ if $\mathbf{p}_k + s_k\mathbf{w}_k$ is the starting point of segment k and $s' = -s$ otherwise.

The Neumann boundary conditions are applied to the soma boundaries $\partial\mathcal{A} \setminus \mathcal{I}$ and ending points of neurites $\partial\mathcal{N}^{1D} \setminus (\mathcal{N}^{1D} \cap \mathcal{I})$

$$D\nabla M^{3D+1D,\mathcal{A}}(\mathbf{r},t)\cdot\mathbf{n} = 0, \quad \mathbf{r} \in \partial\mathcal{A} \setminus \mathcal{I} \tag{4.29}$$

$$D\frac{\partial}{\partial s}M_k^{3D+1D,\mathcal{N}}(s_k,t) = 0, \quad \mathbf{p}_k + s_k\mathbf{w}_k \in \partial\mathcal{N}^{1D} \setminus (\mathcal{N}^{1D} \cap \mathcal{I}) \tag{4.30}$$

The initial conditions are

$$M_k^{3D+1D,\mathcal{N}}(s,0) = 1 \quad (k = 1\ldots\mathcal{K}),$$
$$M^{3D+1D,\mathcal{A}}(\mathbf{r},0) = 1.$$

The signal is computed as

$$S^{3D+1D}(b) := \frac{1}{|\mathcal{A}| + |\mathcal{N}|}\left(\int_{\mathcal{A}} M^{3D+1D,\mathcal{A}}(\mathbf{r},TE)d\mathbf{r} + \sum_{k=1}^{\mathcal{K}} |\mathcal{O}_k|\, S_k^{tr}(b\,\sin^2\theta_k)\int_0^{\ell_k} M_k^{3D+1D,\mathcal{N}}(s,TE)\,ds\right), \tag{4.31}$$

where $|\mathcal{N}| = \sum_k |\mathcal{O}_k|\,\ell_k$.

We call the model described here the "3D+1D" model. We emphasize that the solution in the soma and in each of the line segments are mutually *linked* via the interface conditions of the PDE formulation.

4.5 The disconnected "3D | 1D" model

4.5.1 Exchange between neurites and soma

First, we examine whether it is necessary to "link" the soma and the attached neurites.

The residence time

We numerically compute the residence time inside neurites and soma by using the Kärger model from Eqs. (3.16) and (3.17) at $\mathbf{g} = 0$. The neuron is modeled by 26 straight cylindrical segments which may have different lengths but all are of the same radius r, and a spherical soma of radius $R = 10\mu$m. The segment lengths ℓ_k and radius r were changed to generate four neurons whose information is summarized in Table 4.2.

Table 4.2: Information of four neurons.

Neuron index	volume fraction of soma (%)	radius (μm)	segment lengths (μm)	total length (μm)
1	63	1	20 - 45	800
2	29	2	20 - 45	800
3	37	1	50 - 112.5	2272
4	13	2	50 - 112.5	2272

The residence time for these four neurons are shown in Figure 4.5. We see that the residence times in both the soma and neurites are very large ($\tau^l > 500\text{ms}, l = \mathcal{N}, \mathcal{A}$). The residence time inside neurites is usually larger than that of the soma even when the volume fraction of soma is bigger. Finally, we see that the residence times do not approach a limiting value up to $\Delta = 200\text{ms}$.

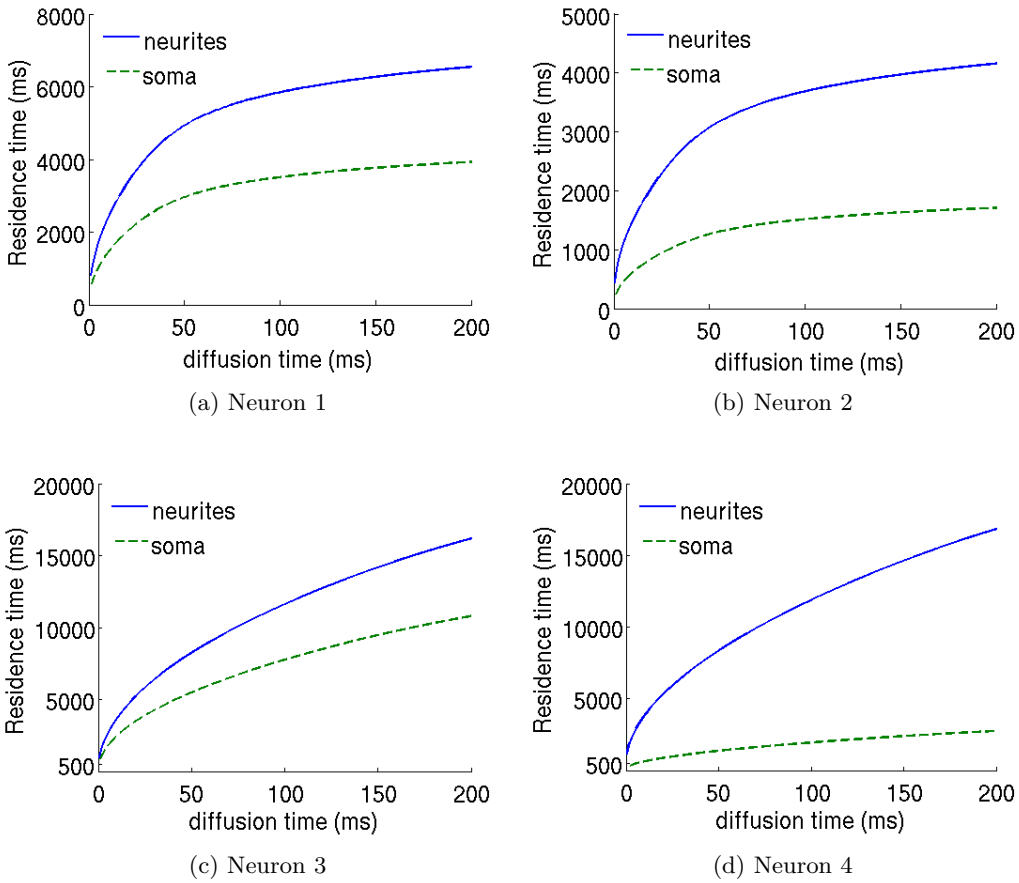

(a) Neuron 1

(b) Neuron 2

(c) Neuron 3

(d) Neuron 4

Figure 4.5: The residence times for four different neurons described in Table 4.2. The residence times are very large in both the soma and neurites. The residence time in neurites is usually larger than that in the soma.

The mass exchange

We denote by M^{3D}_{SIC} the solution M^{3D} when the initial condition is set to 1 for the soma and 0 for neurites and M^{3D}_{NIC} indicates the solution M^{3D} when the initial condition is set to 0 for the soma and 1 for neurites. The mass exchange at $\|\mathbf{g}\| = 0$ from the soma to neurites, $\varepsilon_{\mathcal{A}}$, and from neurites to the soma, $\varepsilon_{\mathcal{N}}$, after normalization, can be computed as:

$$\begin{aligned} \varepsilon_{\mathcal{A}} &= \frac{1}{|\mathcal{A}| + |\mathcal{N}|} \int_{\mathcal{N}} M^{3D}_{SIC}(\mathbf{r}, TE)\, d\mathbf{r}, \\ \varepsilon_{\mathcal{N}} &= \frac{1}{|\mathcal{A}| + |\mathcal{N}|} \int_{\mathcal{A}} M^{3D}_{NIC}(\mathbf{r}, TE)\, d\mathbf{r}. \end{aligned} \tag{4.32}$$

The mass conservation gives $\varepsilon := \varepsilon_{\mathcal{A}} = \varepsilon_{\mathcal{N}}$. We will perform simulations on 3D neurons to numerically check an estimation:

$$\max_b \left\{ \left| S^{3D} - S^{3D|3D} \right| \right\} \leq 2\varepsilon. \tag{4.33}$$

where S^{3D} and $S^{3D|3D}$ are computed by Eq. (4.4) and (4.13).

In Fig. 4.6, we show the 2ε and the difference between signals of connected and disconnected neurons. Two neurons in Table 4.2 are used and eight $b-$values $b = 0, 100, 500, 1000, 1500, 2000, 2500, 3000\text{s/mm}^2$ are considered. The simulations are performed for five diffusion times $\Delta = 10, 40, 80, 100, 200\text{ms}$ with fixed duration $\delta = 2.5\text{ms}$. We see that the difference between two signals is always below 2ε and it is below 10% for all diffusion times. Because neuron 2 is thicker than neuron 1, the mass exchange in neuron 1 (Figure 4.6a) is smaller than that in neuron 2 (Figure 4.6b).

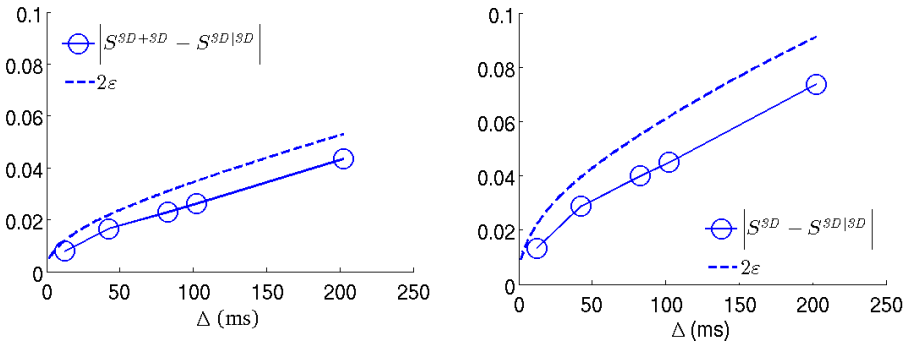

(a) (b)

Figure 4.6: The difference between signals of connected and disconnected neurons in comparison with 2ε for two neurite radii $r = 1\mu$m (4.6a) and $r = 2\mu$m (4.6b).

4.5.2 The disconnected "3D | 1D" model

The simulations of the previous sections showed that the exchange between the soma and neurites is very low and it is can be neglected to consider each domain

separately. Now we replace 3D neurites by corresponding 1D neurites and this leads us to the disconnected "3D|1D" model of the dMRI signal in the neuron:

$$\begin{aligned}\frac{\partial}{\partial t}M^{3D,\mathcal{A}}(\mathbf{r},t) &= -I\gamma f(t)\mathbf{g}\cdot\mathbf{r}\,M^{3D,\mathcal{A}}(\mathbf{r},t) + \nabla\cdot(D\nabla M^{3D,\mathcal{A}}(\mathbf{r},t)),\\ \frac{\partial}{\partial t}M_k^{1D,\mathcal{N}}(s,t) &= -I\gamma\, f(t)\,\mathbf{g}\cdot(\mathbf{p}_k + s\mathbf{w}_k)\,M_k^{1D,\mathcal{N}}(s,t) + D\frac{\partial^2}{\partial s^2}M_k^{1D,\mathcal{N}}(s,t),\end{aligned} \tag{4.34}$$

with interface conditions at the intersections $\mathbf{r}$ between neurite segments:

$$M_k^{1D,\mathcal{N}}(s_k,t) = M_{k'}^{1D,\mathcal{N}}(s_{k'},t), \tag{4.35}$$

$$\sum_k |\mathcal{O}_k|\, D\frac{\partial}{\partial s'}M_k^{1D,\mathcal{N}}(s_k,t) = 0. \tag{4.36}$$

for some k, k' such that $\mathbf{p}_k + s_k\mathbf{w}_k = \mathbf{p}_{k'} + s_{k'}\mathbf{w}_{k'} = \mathbf{r}$.

The Neumann boundary conditions are applied to the soma boundaries $\partial\mathcal{A}$ and ending points of neurites $\partial\mathcal{N}^{1D}$

$$D\nabla M^{3D,\mathcal{A}}(\mathbf{r},t)\cdot\mathbf{n} = 0, \quad \mathbf{r}\in\partial\mathcal{A} \tag{4.37}$$

$$D\frac{\partial}{\partial s}M_k^{1D,\mathcal{N}}(s_k,t) = 0, \quad \mathbf{p}_k + s_k\mathbf{w}_k \in \partial\mathcal{N}^{1D} \tag{4.38}$$

The initial conditions are

$$\begin{aligned}M_k^{1D,\mathcal{N}}(s,0) &= 1 \quad (k = 1\ldots\mathcal{K}),\\ M^{3D,\mathcal{A}}(\mathbf{r},0) &= 1.\end{aligned}$$

The signal is:

$$\begin{aligned}S^{3D|1D}(b) := \frac{1}{|\mathcal{A}|+|\mathcal{N}|}\Bigg(&\int_{\mathcal{A}} M^{3D,\mathcal{A}}(\mathbf{r},TE)d\mathbf{r}\\ &+\sum_{k=1}^{\mathcal{K}}|\mathcal{O}_k|\,S_k^{tr}(b\,\sin^2\theta_k)\int_0^{\ell_k}M_k^{1D,\mathcal{N}}(s,TE)\,ds\Bigg),\end{aligned} \tag{4.39}$$

where $|\mathcal{N}| = \sum_k |\mathcal{O}_k|\,\ell_k$.

We perform simulations for different diffusion times on the neuron including the spherical soma and two neurite trees. The soma radius is fixed to $R = 10\mu$m while the length and radius of neurite segments are changed to study the validity of the two models.

For the neuron with neurite radius $r = 1\mu$m and the length of neurite segments varying from 50 to 112.5μm, there is no significant difference between S^{3D}, S^{3D+1D} and $S^{3D|1D}$ (Fig. 4.7) for two diffusion times $\Delta = 40$ and 100ms. The largest difference is below 3% at the highest $b-$value.

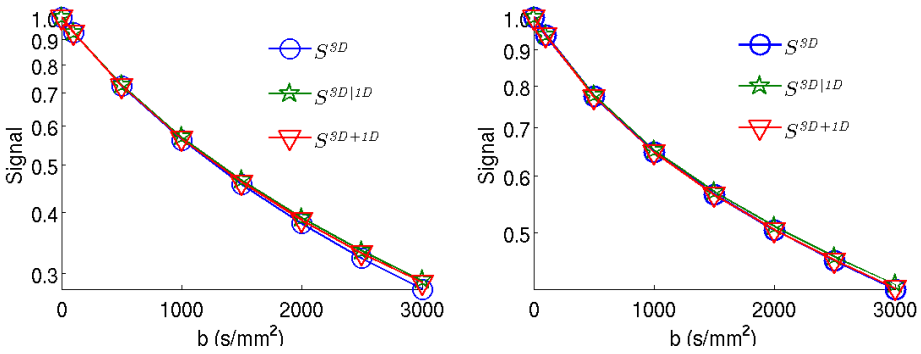

(a) (b)

Figure 4.7: The dMRI signals inside a neuron with the length of neurite segments varying from 50 to 112.5μm in the gradient direction $\mathbf{g}/\|\mathbf{g}\| = (1,1,1)/\sqrt{3}$ at two different diffusion times: $\Delta = 40$ms (4.7a) and $\Delta = 100$ms (4.7b).

For the neuron with short and thick neurites ($r = 2\mu$m, the length of neurite segments is between 20 and 45μm), S^{3D+1D} gives a better approximation to S^{3D} than $S^{3D|1D}$ since the exchange between neurites and the soma is high so that diffusing nuclei have enough time to explore the intersection between neurites and the soma. Figure 4.8 shows the signals for two diffusion times $\Delta = 40$ and 100ms. The relative difference between S^{3D} and $S^{3D|1D}$ becomes bigger for longer diffusion time. The largest difference is about 10% at $\Delta = 100$ms and the smallest difference is about 7% at $\Delta = 40$ms occurring at the highest $b-$values. On the contrary, the relative difference between S^{3D} and S^{3D+1D} remains around 5% for both diffusion times. At short diffusion times, there is no significant difference between two models.

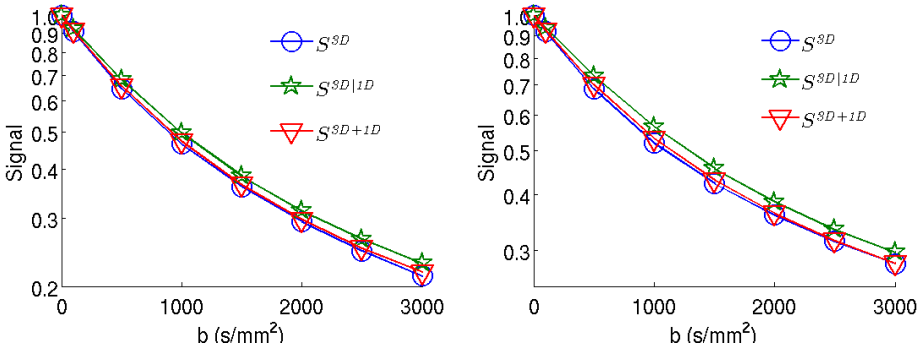

(a) (b)

Figure 4.8: The dMRI signals inside a neuron with the length of neurite segments varying from 20 to 45μm in the gradient direction $\mathbf{g}/\|\mathbf{g}\| = (0,0,1)$ at two different diffusion times: $\Delta = 40$ms (4.8a), $\Delta = 100$ms (4.8b).

4.5.3 Timing

All simulations were performed on a Dell Precision M4700 laptop (Intel(R) Core(TM) i7-3740QM CPU @ 2.70GHz). The simulation for S^{3D} for eight $b-$values between 0 and 3000 s/mm^{2}using the code described in chapter 2 took about 30 minutes on a mesh with 11314 vertices, where the finite element size in the soma is about 1778 vertices. The simulation of the S^{3D+1D} with the same number of $b-$values on a mesh with 2897 vertices (while keeping the same 3D mesh in the soma) took about 5 minutes.

4.6 The ADC inside neurites trees

In this section we study the dMRI signal inside 1D neurites trees. To analyze the signal attenuation as a function of b-values for a chosen pulse sequence, we will compute ADC by Eq. (1.22) for neurites trees, $ADC^{\mathcal{N}}$.

In practice, we obtain $ADC^{\mathcal{N}}$ from the dMRI signal at 11 $b-$values between 0 and 500 s/mm^2 and using cubic polyfit of the logarithm of the signal.

According to [31,34], the $ADC^{\mathcal{N}}$ on a neurites tree can be approximated by

$$ADC^{\mathcal{N}} \approx D^{\mathcal{N}} \int_0^{\pi} \cos^2\theta\, P(\theta)\, d\theta, \tag{4.40}$$

where $D^{\mathcal{N}}$ is the (possibly time-dependent) effective longitudinal (parallel to the dendrite segment) diffusivity, $P(\theta)$ is the probability distribution of the segment orientation with respect to the gradient direction.

For a neurites tree modeled by K connected line segments, if we know exactly the orientation of K segments of the neurites tree, we can rewrite Eq. (4.40) as follows:

$$ADC^{\mathcal{N}} \approx D^{\mathcal{N}} \left(\frac{1}{L} \sum_{k=1}^{K} \ell_k \cos^2\theta_k \right). \tag{4.41}$$

We test the validity of Eq. (4.41) by numerically checking if there exists a (possibly time-dependent) $D^{\mathcal{N}}$ which satisfies Eq. (4.41) for many randomly generated neurites trees.

4.6.1 Generation of random neurites trees

In this section, we assume that each neurites tree is modeled by $\mathcal{K}$ segments of two possibly different lengths: n_1 segments of length ℓ_1 and n_2 segments of length ℓ_2. There are three branches coming from each intersection and the father root is located at the coordinate origin $(0,0,0)$. From a root (x_c, y_c, z_c), we randomly take three points of N random, uniformly distributed points on the upper half of the spherical surface $z = z_c + \sqrt{\ell_k^2 - (x-x_c)^2 - (y-y_c)^2}$ to ensure that the neurites tree always grows up. This root is connected with these three points to make three branches.

Generating N uniform points on a spherical surface is a classical problem. We assume that each point $P(x, y, z)$ on a spherical surface is defined by colatitude φ, longitude θ, and radius ρ (Figure 4.9a). N uniform points are generated by Algorithm 1.

Algorithm 1 Algorithm to generate N random, uniformly distributed points (x, y, z) on the half of spherical surface of radius ρ and center (x_c, y_c, z_c).

1: $\theta :=$ randreal(N, $[0, 2\pi]$); {generate N random values of θ in the interval $[0, 2\pi]$}
2: $\varphi :=$ arcsin(randreal(N, $[0, 1]$)); {generate N values of φ such that $\sin(\varphi)$ is uniformly distributed in the interval $[0, 1]$}
3: $x := \rho\cos(\varphi)\cos(\theta) + x_c$;
$y := \rho\cos(\varphi)\sin(\theta) + y_c$;
$z := \rho\sin(\varphi) + z_c$; {transform spherical to Cartesian coordinates.}

Figures 4.9b and 4.9c show the uniform distribution of 1000 points, generated by Algorithm 1, on the upper half of the spherical surface of radius $\rho = 10\mu$m and center $(x_c, y_c, z_c) = (0, 0, 0)$ in different directions of view.

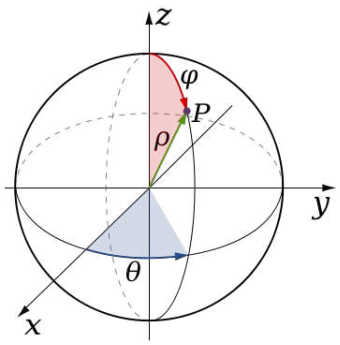

(a)

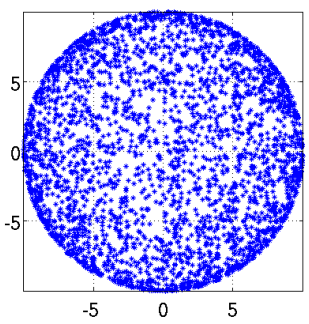

(b)

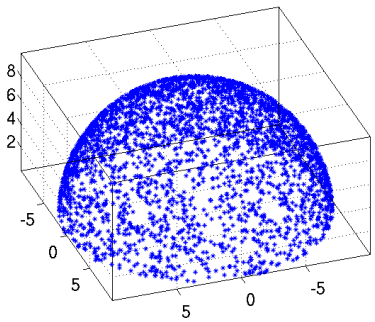

(c)

Figure 4.9: A diagram of spherical coordinates defining a point P by colatitude φ, longitude θ, and radius ρ (4.9a); and the uniform distribution of 1000 points on the upper half of the spherical surface of radius $\rho = 10\mu$m in different direction of view (4.9b, 4.9c)

Next, W neurites trees are randomly generated by Algorithm 2.

Algorithm 2 Algorithm to randomly generate W neurites trees modeled by n_1 segments of length ℓ_1 and n_2 segments of length ℓ_2.

θ := randreal(1000, $[0, 2\pi]$); {Generate 1000 random, uniformly distributed values of θ in $[0, 2\pi]$}
φ := arcsin(randreal(1000, $[0, 1]$)); {Generate 1000 values of φ in $[0, \pi/2]$ such that $\sin(\varphi)$ is random, uniformly distributed in $[0, 1]$}
Initialize two segment lengths ℓ_1 and ℓ_2;
Initialize two numbers of segment lengths n_1 and n_2;
Initialize the numbers of tree generations GN;
Initialize the numbers of branches BN;
FOR ntree **FROM** 1 **TO** W **DO**
    Initialize EDGES as an empty set;
    Initialize NODES as a set of one element (0,0,0);
    num_nodes :=1;
    FOR gn **FROM** 1 **TO** GN **DO**
        SNODE := 2+BN*(BN$^{\text{gn}-2}$-1)/(BN-1);
        ENODE := 1+BN*(BN$^{\text{gn}-1}$-1)/(BN-1);
        FOR node **FROM** SNODE **TO** ENODE **DO**
            (x_c, y_c, z_c) := NODES[node];
            FOR bn **FROM** 1 **TO** BN **DO**
                Randomly choose one length ρ of two lengths ℓ_1 and ℓ_2;
                IF $\rho == \ell_1$ **THEN**
                    Decrease n_1 by 1;
                ELSE
                    Decrease n_2 by 1;
                END IF;
                Randomly choose a pair (θ_1, φ_1) of (θ, φ);
                {transform spherical to Cartesian coordinates.}
                $x := \rho\cos(\varphi_1)\cos(\theta_1) + x_c$;
                $y := \rho\cos(\varphi_1)\sin(\theta_1) + y_c$;
                $z := \rho\sin(\varphi_1) + z_c$;
                Add (x, y, z) to the NODES array;
                Increase num_nodes by 1;
                Connect node and num_nodes to form a new edge;
                Add new edge to the EDGES array;
            END DO
        END DO
    END DO
    RETURN a tree modeled by EDGES and NODES.
END DO

In Fig. 4.10a, we show a neurites tree modeled by 39 segments: 30 segments of length $\ell = 27\mu$m and 9 segments of length $\ell = 90\mu$m. The empirical distribution of

$\frac{1}{L}\sum_{k=1}^{39} \ell_k \cos^2\theta_k$ for 1000 neurites tree is shown in Fig. 4.10b.

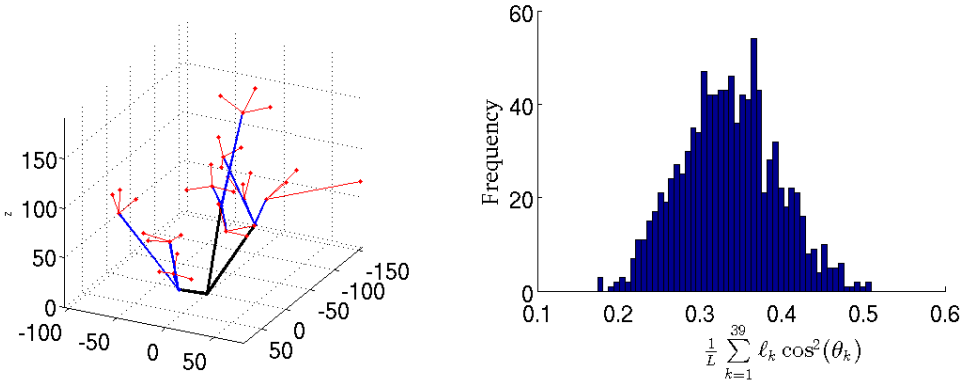

(a) (b)

Figure 4.10: An example of a neurites tree composed of 39 segments: 30 segments of length $\ell = 27\mu$m and 9 segments of length $\ell = 90\mu$m (4.10a) and the empirical distribution of $\frac{1}{L}\sum_{k=1}^{39} \ell_k \cos^2\theta_k$ for 1000 neurites trees generated by Algorithm 2 (4.10b).

4.6.2 Least squares problem

Fitting Eq. (4.41) for many neurites trees is a least squares problem. On the i^{th} neurites tree, let $a_i = \frac{1}{L}\sum_{k=1}^{K} \ell_k \cos^2\theta_k$ and $d_i = ADC^{\mathcal{N}}$. We need to solve

$$\min_{D^{\mathcal{N}}} \sum_{i}^{W} (a_i\, D^{\mathcal{N}} - d_i)^2, \tag{4.42}$$

for W samples of neurites trees. The solution is

$$D^{\mathcal{N}} = \left(\sum_{i}^{W} a_i^2\right)^{-1} \sum_{i}^{W} a_i d_i.$$

The root of the mean squared error is then

$$RMSE = \sqrt{\frac{1}{W}\sum_{i}^{W}\Big(a_i\, D^{\mathcal{N}} - d_i\Big)^2}. \tag{4.43}$$

We generated 1000 neurites trees of three generations to compute $ADC^{\mathcal{N}}$. Figure 4.11 shows the empirical distribution of 1000 simulated $ADC^{\mathcal{N}}$ versus $\frac{1}{L}\sum_k \ell_k \cos^2(\theta_k)$ at $\Delta = 2.5$ms (4.11a), $\Delta = 40$ms (4.11b) $\Delta = 80$ms (4.11c).

The mean values of $ADC^{\mathcal{N}}$ for three diffusion times are $9.4 \cdot 10^{-4}$mm^2/s, $7.9 \cdot 10^{-4}$mm^2/s and $7.2 \cdot 10^{-4}$mm^2/s respectively.

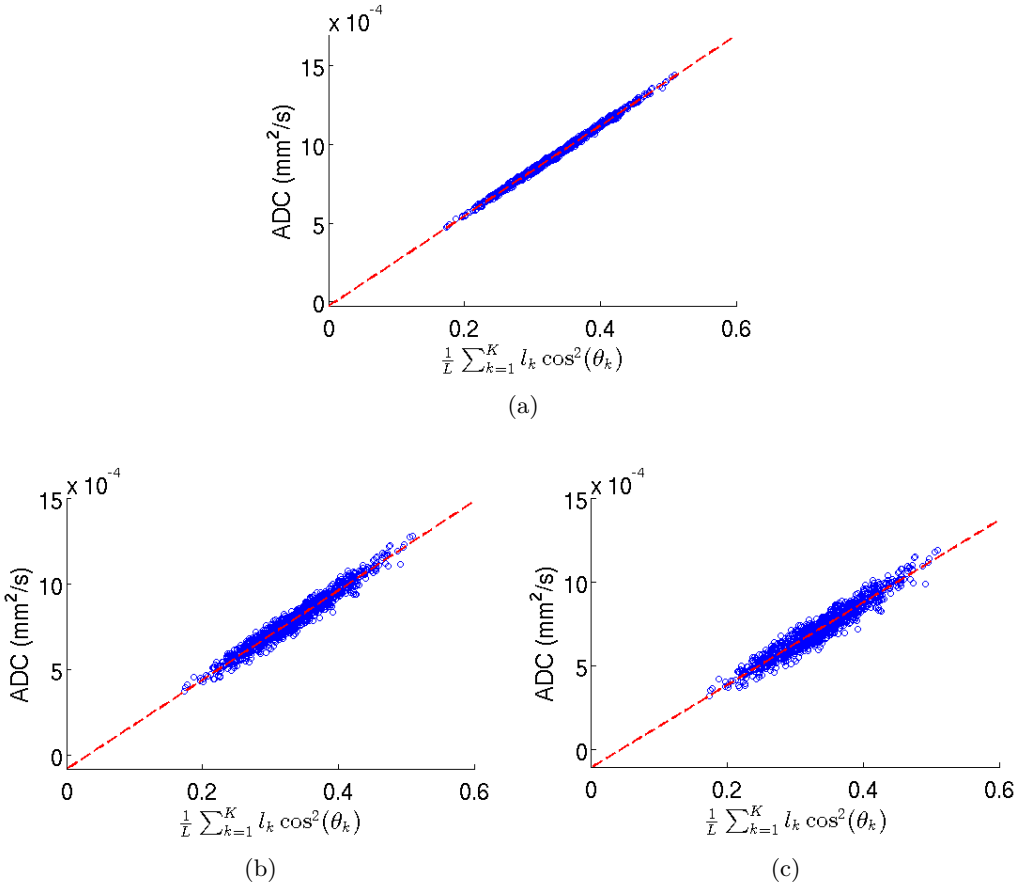

(a)

(b) (c)

Figure 4.11: The distribution of 1000 simulated $ADC^{\mathcal{N}}$ versus $\frac{1}{L}\sum_k \ell_k \cos^2(\theta_k)$ at $\Delta = 2.5$ms (4.11a), $\Delta = 40$ms (4.11b) $\Delta = 80$ms (4.11c). The simulations are performed on 1000 neurites trees modeled by 39 segments: 30 segments of length $\ell = 27\mu$m and 9 segments of length $\ell = 90\mu$m.

The $D^{\mathcal{N}}$ and RMSE obtained by using the least-squares method are summarized in Table 4.3. We see that $D^{\mathcal{N}}$ depends on diffusion time. Additionally, at the short diffusion time $\Delta = 2.5$ms, the fit is very good. The fit becomes less good for longer diffusion times but the relative error, $RMSE/D^{\mathcal{N}}$, is always below 3% for all diffusion times.

Table 4.3: $D^{\mathcal{N}}$ and RMSE of simulated results shown in Fig. 4.11.

Δ (ms)	$D^{\mathcal{N}}$	$RMSE/D^{\mathcal{N}}$ (%)
2.5	$2.81 \cdot 10^{-3}$	0.38
10	$2.67 \cdot 10^{-3}$	0.68
40	$2.38 \cdot 10^{-3}$	1.42
80	$2.16 \cdot 10^{-3}$	2.01
100	$2.08 \cdot 10^{-3}$	2.23

4.6.3 Effective length of neurites trees with variable lengths

Can one find an effective length for a neurite tree that has segments of different lengths? In the first step, in order to calibrate the effective length, we construct many neurites trees with segments of the same length: $\ell_k = \ell, \forall k$. For each length ℓ, $10\mu\text{m} \leq \ell \leq 100\mu\text{m}$, we randomly generate 500 neurites trees. Each neurites tree has 39 segments. The $D^{\mathcal{N}}$ and $RMSE/D^{\mathcal{N}}$ are computed by the least-square method described above for different diffusion times.

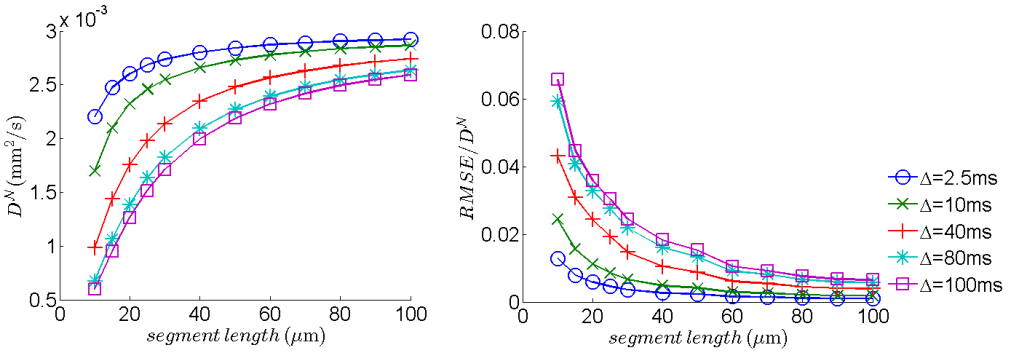

(a)

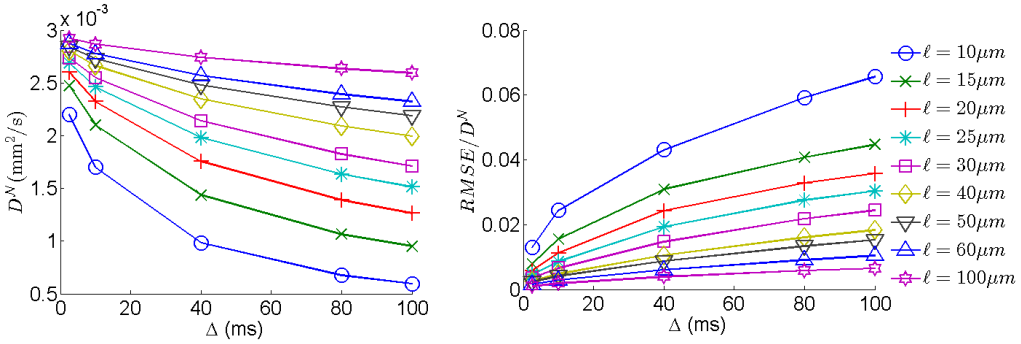

(b)

Figure 4.12: $D^{\mathcal{N}}$ and $RMSE/D^{\mathcal{N}}$ versus segment lengths (4.12a) and diffusion times (4.12b) for neurites trees of the same length $\ell_k = \ell, \forall k$, where $10\mu\text{m} \leq \ell \leq 100\mu\text{m}$.

The results are shown in Fig. 4.12. We see that $D^{\mathcal{N}}$ depends on ℓ and the diffusion time. $D^{\mathcal{N}}$ becomes bigger for longer segments or shorter diffusion times, and it approaches the intrinsic diffusion coefficient $D = 3 \cdot 10^{-3}\text{mm}^2/\text{s}$. We also see that the $RMSE/D^{\mathcal{N}}$ is always below 7% for all diffusion times and segment lengths. This value is smaller for shorter diffusion times or longer segment lengths.

We first interpolate the data in Fig. 4.12 using cubic splines to introduce an effective length $\bar{\ell}$ that corresponds to the fitted $D^{\mathcal{N}}$ at a given diffusion time for an arbitrary neurites tree.

In the next step, we generate many neurites trees, each with 39 segments. There

are now two different lengths in the trees: n_1 segments of length ℓ_1 and n_2 segments of length ℓ_2, $n_1+n_2=39$. The generated 500 samples for each choice of n_1, n_2, l_1, l_2 are shown in Tables 4.4, 4.5 and 4.6. These tables indicate that even for neurites trees with two distinct lengths, an effective length $\bar{\ell}$ is well defined if two lengths ℓ_1 and ℓ_2 are not very far each other (Table 4.4 and Table 4.6 - the first case). In fact, it is close to the volume averaged neurites length

$$\bar{\ell} \approx \ell_{avg} \equiv \left(\sum_k n_k\right)^{-1} \sum_k n_k \ell_k.$$

However, when ℓ_1 is very far from ℓ_2, the effective length $\bar{\ell}$ changes quite a lot for different diffusion times (Table 4.5 and Table 4.6 - the second case) and $\bar{\ell}$ can not give a good approximation to the ℓ_{avg}. This is reasonable because $\ell_2 = 100\mu$m, its effective diffusion coefficients $D^{\mathcal{N}}$ approximates the intrinsic diffusion coefficient for all diffusion times with $\Delta \leq 100$ms (Figure 4.12a). The segments are considered as infinitely long ones and the inversion fails.

Table 4.4: The simulations were performed for $\ell_1 = 27\mu$m, $\ell_2 = 90\mu$m.

	$n_1 = 30, n_2 = 9$ ($\ell_{avg} = 41.5\mu$m)		$n_1 = 9, n_2 = 30$ ($\ell_{avg} = 75.5\mu$m)	
Δ (ms)	$D^{\mathcal{N}}(\text{mm}^2/\text{s}) \pm \frac{RMSE}{D^{\mathcal{N}}}(\%)$	$\bar{\ell}(\mu\text{m})$	$D^{\mathcal{N}}(\text{mm}^2/\text{s}) \pm \frac{RMSE}{D^{\mathcal{N}}}(\%)$	$\bar{\ell}(\mu\text{m})$
2.5	$2.80 \cdot 10^{-3} \pm 0.4$	39	$2.89 \cdot 10^{-3} \pm 0.1$	70
10	$2.67 \cdot 10^{-3} \pm 0.7$	41	$2.82 \cdot 10^{-3} \pm 0.2$	74
40	$2.38 \cdot 10^{-3} \pm 1.4$	42	$2.66 \cdot 10^{-3} \pm 0.4$	76
80	$2.16 \cdot 10^{-3} \pm 2.0$	43	$2.52 \cdot 10^{-3} \pm 0.6$	75
100	$2.08 \cdot 10^{-3} \pm 2.2$	44	$2.47 \cdot 10^{-3} \pm 0.7$	76

Table 4.5: The simulations were performed for $\ell_1 = 10\mu$m, $\ell_2 = 100\mu$m.

	$n_1 = 30, n_2 = 9$ ($\ell_{avg} = 30.8\mu$m)		$n_1 = 38, n_2 = 1$ ($\ell_{avg} = 12.3\mu$m)	
Δ (ms)	$D^{\mathcal{N}}(\text{mm}^2/\text{s}) \pm \frac{RMSE}{D^{\mathcal{N}}}(\%)$	$\bar{\ell}(\mu\text{m})$	$D^{\mathcal{N}}(\text{mm}^2/\text{s}) \pm \frac{RMSE}{D^{\mathcal{N}}}(\%)$	$\bar{\ell}(\mu\text{m})$
2.5	$2.74 \cdot 10^{-3} \pm 0.7$	30	$2.37 \cdot 10^{-3} \pm 1.9$	12
10	$2.58 \cdot 10^{-3} \pm 1.2$	32	$1.97 \cdot 10^{-3} \pm 3.6$	13
40	$2.33 \cdot 10^{-3} \pm 2.0$	39	$1.40 \cdot 10^{-3} \pm 7.1$	15
80	$2.21 \cdot 10^{-3} \pm 2.3$	46	$1.15 \cdot 10^{-3} \pm 9.4$	16
100	$2.16 \cdot 10^{-3} \pm 2.4$	48	$1.09 \cdot 10^{-3} \pm 10.2$	17

Table 4.6: The simulations were performed for two choices of n_1, n_2, l_1, l_2: $n_1 = 10, n_2 = 29, l_1 = 20\mu\text{m}, l_2 = 40\mu\text{m}$ and $n_1 = 35, n_2 = 4, l_1 = 11.4\mu\text{m}, l_2 = 100\mu\text{m}$.

	$n_1 = 10, \ell_1 = 20\mu\text{m}$, $n_2 = 29, \ell_2 = 40\mu\text{m}$ ($\ell_{avg} = 34.9\mu\text{m}$)		$n_1 = 35, \ell_1 = 11.4\mu\text{m}$, $n_2 = 4, \ell_2 = 100\mu\text{m}$ ($\ell_{avg} = 20.5\mu\text{m}$)	
Δ (ms)	$D^{\mathcal{N}}(\text{mm}^2/\text{s}) \pm \frac{RMSE}{D^{\mathcal{N}}}(\%)$	$\bar{\ell}(\mu\text{m})$	$D^{\mathcal{N}}(\text{mm}^2/\text{s}) \pm \frac{RMSE}{D^{\mathcal{N}}}(\%)$	$\bar{\ell}(\mu\text{m})$
2.5	$2.77 \cdot 10^{-3} \pm 0.3$	34	$2.62 \cdot 10^{-3} \pm 1.2$	21
10	$2.61 \cdot 10^{-3} \pm 0.5$	35	$2.38 \cdot 10^{-3} \pm 2.2$	22
40	$2.25 \cdot 10^{-3} \pm 1.2$	35	$2.0 \cdot 10^{-3} \pm 3.8$	26
80	$1.97 \cdot 10^{-3} \pm 1.7$	35	$1.81 \cdot 10^{-3} \pm 4.7$	30
100	$1.86 \cdot 10^{-3} \pm 2.0$	35	$1.76 \cdot 10^{-3} \pm 4.9$	31

Next, we consider the effect of the orientation distribution on the value of $D^{\mathcal{N}}$. Each neurite is modeled by 10 segments of length 20μm and 29 segments of length 40μm. Table 4.7 shows the least squares fitted $D^{\mathcal{N}}$s and the effective length $\bar{\ell}$ for three different cases of orientation distribution. The segment distribution restricted to three different regions: $0 \leq \varphi \leq \frac{\pi}{2}$, $0 \leq \varphi \leq \frac{\pi}{6}$ and $0 \leq \varphi \leq \frac{\pi}{12}$. We see that $D^{\mathcal{N}}$ and $\bar{\ell}$ do not depend on the orientation distribution of the segments.

Table 4.7: Least squares fitted D^N in three different cases of segment orientations distribution of neurites trees. Each tree has 10 segments of length 20μm and 29 segments of length 40μm.

	$0 \leq \varphi \leq \frac{\pi}{2}$		$0 \leq \varphi \leq \frac{\pi}{6}$		$0 \leq \varphi \leq \frac{\pi}{12}$	
Δ ms	$D^{\mathcal{N}}(\text{mm}^2/\text{s})$	$\bar{\ell}(\mu\text{m})$	$D^{\mathcal{N}}(\text{mm}^2/\text{s})$	$\bar{\ell}(\mu\text{m})$	$D^{\mathcal{N}}(\text{mm}^2/\text{s})$	$\bar{\ell}(\mu\text{m})$
2.5	$2.77 \cdot 10^{-3}$	34.08	$2.76 \cdot 10^{-3}$	32.73	$2.76 \cdot 10^{-3}$	32.73
10	$2.61 \cdot 10^{-3}$	34.66	$2.60 \cdot 10^{-3}$	33.79	$2.60 \cdot 10^{-3}$	33.79
40	$2.25 \cdot 10^{-3}$	34.64	$2.23 \cdot 10^{-3}$	33.71	$2.23 \cdot 10^{-3}$	33.71
80	$1.97 \cdot 10^{-3}$	34.86	$1.93 \cdot 10^{-3}$	33.40	$1.93 \cdot 10^{-3}$	33.40
100	$1.86 \cdot 10^{-3}$	34.73	$1.82 \cdot 10^{-3}$	33.36	$1.81 \cdot 10^{-3}$	33.03

Finally, we consider the effect of gradient direction on $D^{\mathcal{N}}$. Obviously, if the neurite segments are uniformly distributed in half a sphere, $D^{\mathcal{N}}$ should be the same for all directions. So, there is no effect of gradient directions. In this case, we choose the segment orientation in the smallest region $0 \leq \varphi \leq \frac{\pi}{12}$ to see if $D^{\mathcal{N}}$ depends on different directions. Table 4.8 shows that there is a small effect of the gradient direction on $D^{\mathcal{N}}$ and $\bar{\ell}$.

Table 4.8: Least squares fitted D^N for different gradient directions on neurites trees containing 10 segments of length 20μm and 29 segments of length 40μm, with orientation distribution $0 \leq \varphi \leq \frac{\pi}{12}$.

	$\mathbf{g}/\|\mathbf{g}\| = (1,1,1)/\sqrt{3}$		$\mathbf{g}/\|\mathbf{g}\| = (1,0,0)$		$\mathbf{g}/\|\mathbf{g}\| = (0,0,1)$	
Δ ms	$D^{\mathcal{N}}(\text{mm}^2/\text{s})$	$\bar{\ell}(\mu\text{m})$	$D^{\mathcal{N}}(\text{mm}^2/\text{s})$	$\bar{\ell}(\mu\text{m})$	$D^{\mathcal{N}}(\text{mm}^2/\text{s})$	$\bar{\ell}(\mu\text{m})$
2.5	$2.76 \cdot 10^{-3}$	32.73	$2.77 \cdot 10^{-3}$	34.08	$2.77 \cdot 10^{-3}$	34.08
10	$2.60 \cdot 10^{-3}$	33.79	$2.62 \cdot 10^{-3}$	35.58	$2.60 \cdot 10^{-3}$	33.79
40	$2.23 \cdot 10^{-3}$	33.71	$2.27 \cdot 10^{-3}$	35.63	$2.23 \cdot 10^{-3}$	33.71
80	$1.93 \cdot 10^{-3}$	33.40	$2.00 \cdot 10^{-3}$	36.03	$1.92 \cdot 10^{-3}$	33.05
100	$1.81 \cdot 10^{-3}$	33.03	$1.90 \cdot 10^{-3}$	36.20	$1.81 \cdot 10^{-3}$	33.03

4.6.4 Fitting $ADC^{\mathcal{N}}$ by two $D^{\mathcal{N}}$s

Now for neurites trees with two different lengths, $\ell_1 = 27\mu$m ($n_1 = 30$) and $\ell_2 = 90\mu$m ($n_2 = 9$) (data shown in Fig. 4.11) we check the fit of $ADC^{\mathcal{N}}$ when two free parameters $D^{\mathcal{N}_1}$ and $D^{\mathcal{N}_2}$ are introduced:

$$ADC^{\mathcal{N}} \approx D^{\mathcal{N}_1}\left(\frac{\ell_1}{L}\sum_{k_1 \in K_1}\cos^2\theta_{k_1}\right) + D^{\mathcal{N}_2}\left(\frac{\ell_2}{L}\sum_{k_2 \in K_2}\cos^2\theta_{k_2}\right), \tag{4.44}$$

where K_1 is the set of the segments of length l_1 and K_2 is the set of the segments of length l_2. We will use the least-squares method to fit the above equation. We denote $a_i = \frac{\ell_1}{L}\sum_{k_1 \in K_1}\cos^2\theta_{k_1}$, $c_i = \frac{\ell_2}{L}\sum_{k_2 \in K_2}\cos^2\theta_{k_2}$, $d_i = ADC_i^{\mathcal{N}}$. From a straightforward computation, we have

$$D^{\mathcal{N}_1} = \frac{\sum_i^N a_i c_i \sum_i^N c_i d_i - \sum_i^N c_i^2 \sum_i^N a_i d_i}{\left(\sum_i^N a_i c_i\right)^2 - \sum_i^N c_i^2 \sum_i^N a_i^2}, \quad D^{\mathcal{N}_2} = \frac{-\sum_i^N d_i a_i \sum_i^N a_i c_i + \sum_i^N a_i^2 \sum_i^N c_i d_i}{\left(\sum_i^N a_i c_i\right)^2 - \sum_i^N c_i^2 \sum_i^N a_i^2}.$$

The root mean square error (RMSE) is:

$$RMSE = \sqrt{\frac{1}{W}\sum_i^W \left(a_i\, D^{\mathcal{N}_1} + c_i\, D^{\mathcal{N}_2} - d_i\right)^2}, \tag{4.45}$$

where W is the number of neurites in our sample.

We see in Table 4.9 that fitting with two parameters $D^{\mathcal{N}_1}, D^{\mathcal{N}_2}$ gives better approximation than just fitting with one parameter $D^{\mathcal{N}}$ (smaller RMSE).

Table 4.9: $D^{\mathcal{N}_1}$, $D^{\mathcal{N}_2}$ and $D^{\mathcal{N}}$ and RMSE (in mm^2/s) of simulated results shown in Fig. 4.11.

Δ ms	One-parameter fit		Two-parameter fit		
	$D^{\mathcal{N}}$	RMSE	$D^{\mathcal{N}_1}$	$D^{\mathcal{N}_2}$	RMSE
2.5	$2.81 \cdot 10^{-3}$	$1.06 \cdot 10^{-5}$	$2.66 \cdot 10^{-3}$	$2.95 \cdot 10^{-3}$	$0.70 \cdot 10^{-5}$
10	$2.67 \cdot 10^{-3}$	$1.82 \cdot 10^{-5}$	$2.43 \cdot 10^{-3}$	$2.91 \cdot 10^{-3}$	$1.20 \cdot 10^{-5}$
40	$2.38 \cdot 10^{-3}$	$3.39 \cdot 10^{-5}$	$1.92 \cdot 10^{-3}$	$2.83 \cdot 10^{-3}$	$2.23 \cdot 10^{-5}$
80	$2.16 \cdot 10^{-3}$	$4.35 \cdot 10^{-5}$	$1.56 \cdot 10^{-3}$	$2.74 \cdot 10^{-3}$	$2.80 \cdot 10^{-5}$
100	$2.08 \cdot 10^{-3}$	$4.63 \cdot 10^{-5}$	$1.44 \cdot 10^{-3}$	$2.71 \cdot 10^{-3}$	$2.95 \cdot 10^{-5}$

The effective lengths, $\bar{\ell}_1$ and $\bar{\ell}_2$, corresponding to $D^{\mathcal{N}_1}$ and $D^{\mathcal{N}_2}$ are shown in Table 4.10. They approximate two lengths $\ell_1 = 27\mu$m and $\ell_2 = 90\mu$m used in the simulations.

Table 4.10: The effective lengths corresponding to $D^{\mathcal{N}_1}, D^{\mathcal{N}_2}$.

Δ (ms)	$\bar{\ell}_1(\mu\mathrm{m})$	$\bar{\ell}_2(\mu\mathrm{m})$
2.5	23	71
10	24	120
40	24	133
80	23	129
100	23	129

4.6.5 A relationship between neurites trees with two lengths and single length

Next, we numerically clarify the relationship between

- $D^{\mathcal{N}}_{\ell_1,\ell_2}$, fitted on trees containing segments of two lengths (l_1 and l_2),
- $D^{\mathcal{N}}_{\ell_1}$, fitted on trees containing segments of the same length (l_1 only),
- $D^{\mathcal{N}}_{\ell_2}$, fitted on trees containing segments of the same length (l_2 only).

The results presented in Table 4.9 suggest an approximation:

$$D^{\mathcal{N}}_{\ell_1,\ell_2} \approx \frac{n_1\ell_1 D^{\mathcal{N}}_{l_1} + n_2\ell_2 D^{\mathcal{N}}_{l_2}}{n_1\ell_1 + n_2\ell_2}, \tag{4.46}$$

where n_1 and n_2 are the numbers of segments with length of ℓ_1 and ℓ_2, respectively. We test this hypothesis and show results for $\ell_1 = 27\mu$m and $\ell_2 = 90\mu$m, with $n_1 = 9$ and $n_2 = 30$ (Figure 4.13a), and $n_1 = 30$ and $n_2 = 9$ (Figure 4.13b). The left and right hand sides of Eq. (4.46) are very close, with relative difference below 0.5%.

Figure 4.13c shows the results for $\ell_1 = 10\mu\text{m}, \ell_2 = 40\mu\text{m}$ and $n_1 = 10, n_2 = 29$. The relative difference between the right and left hand sides of Eq. (4.46) is 1.2%.

The results for $\ell_1 = 10\mu\text{m}$ and $\ell_2 = 100\mu\text{m}$; $n_1 = 30, n_2 = 9$ are shown in Figure 4.13d. The results for $n_1 = 38, n_2 = 1$ are shown in Figure 4.13e. The relative difference is bigger compared to the previous simulations but it is still smaller than 8%.

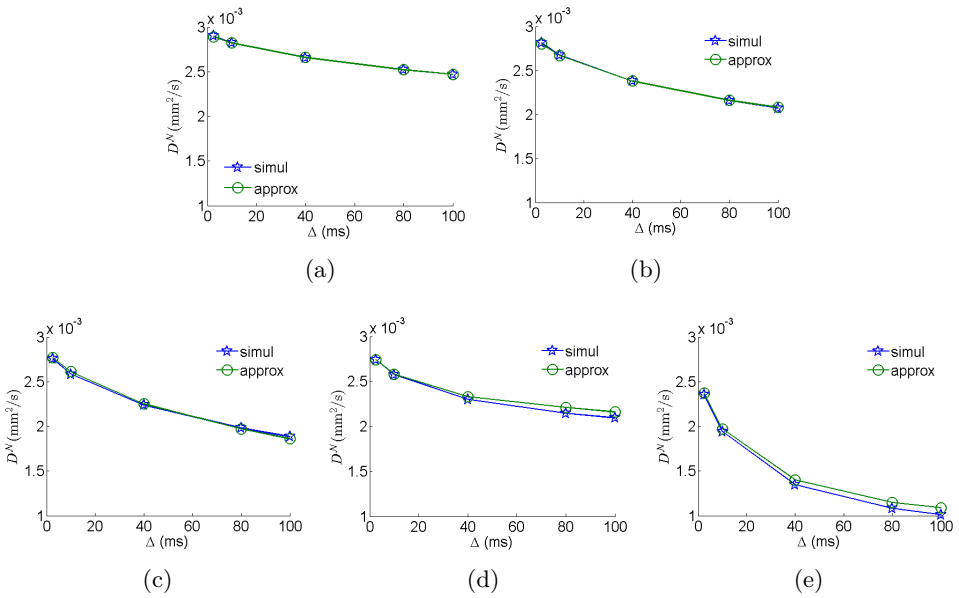

Figure 4.13: The simulated $D^{\mathcal{N}}$ and its approximation by Eq. (4.46) for $\ell_1 = 27\mu\text{m}, \ell_2 = 90\mu\text{m}, n_1 = 9, n_2 = 30$ (4.13a); $\ell_1 = 27\mu\text{m}, \ell_2 = 90\mu\text{m}, n_1 = 30, n_2 = 9$ (4.13b); $\ell_1 = 10\mu\text{m}, \ell_2 = 40\mu\text{m}, n_1 = 10, n_2 = 29$ (4.13c); $\ell_1 = 10\mu\text{m}, \ell_2 = 100\mu\text{m}, n_1 = 30, n_2 = 9$ (4.13d); $\ell_1 = 10\mu\text{m}, \ell_2 = 100\mu\text{m}, n_1 = 38, n_2 = 1$ (4.13e).

4.7 Analytical upper and lower bounds of ADC and signal inside neurites trees

We propose simple analytical expressions for $ADC^{\mathcal{N}}$ on neurites trees that take into account the diffusion time and segment lengths. Let the neurites tree contain segments $\mathcal{T}_k$ and let $D^{\mathcal{T}_k}$ be the longitudinal diffusivity along $\mathcal{T}_k$, then the $ADC^{\mathcal{N}}$ for infinite segments is:

$$ADC^{\mathcal{N}}_{\max} = \frac{1}{\sum_k \ell_k} \sum_k \ell_k \, D^{\mathcal{T}_k}_{\max} \cos^2 \theta_k, \tag{4.47}$$

where $D^{\mathcal{T}_k}_{\max} = D$ is the intrinsic diffusion coefficient. When the segments are considered isolated at the end points, then the $ADC^{\mathcal{N}}$ is:

$$ADC^{\mathcal{N}}_{\min} = \frac{1}{\sum_k \ell_k} \sum_k \ell_k \, D^{\mathcal{T}_k}_{\min} \cos^2 \theta_k, \tag{4.48}$$

where $D_{\min}^{\mathcal{T}_k}$ is given by Eq. (1.41) from Section 1.6.3.

Now we show that the $ADC^{\mathcal{N}}$ for neurites trees lies between $ADC_{\min}^{\mathcal{N}}$ and $ADC_{\max}^{\mathcal{N}}$. Figure 4.14 shows the results for a neurites tree with $200\mu\text{m} \leq l_k \leq 450\mu\text{m}$ in the gradient direction $\mathbf{g}/\|\mathbf{g}\| = (1,1,1)/\sqrt{3}$. The difference between $ADC_{\min}^{\mathcal{N}}$ and $ADC_{\max}^{\mathcal{N}}$ is less than 11% even at the very long diffusion time, $\Delta = 200$ms. One can also see that the simulated ADC curve lies between $ADC_{\min}^{\mathcal{N}}$ and $ADC_{\max}^{\mathcal{N}}$ curves.

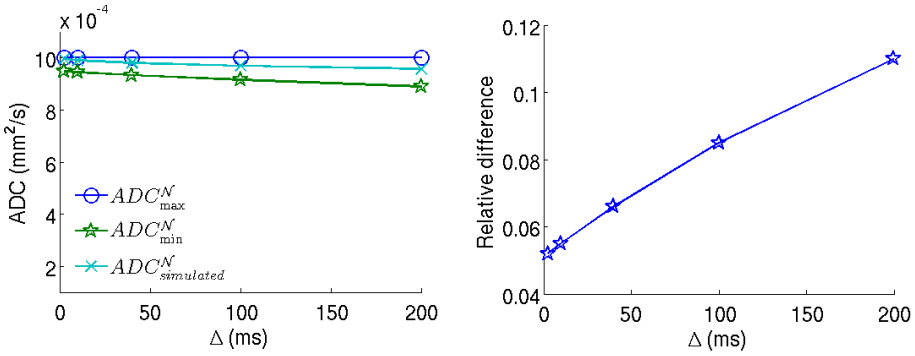

(a) (b)

Figure 4.14: The $ADC_{\min}^{\mathcal{N}}$, $ADC_{\max}^{\mathcal{N}}$ and simulated ADC for the neurites with the length varying from 200 to 450μm and $\mathbf{g}/\|\mathbf{g}\| = (1,1,1)/\sqrt{3}$ are close to each other (4.14a). The relative difference between $ADC_{\min}^{\mathcal{N}}$ and $ADC_{\max}^{\mathcal{N}}$ is between 5% ($\Delta = 2.5$ms) and 11% ($\Delta = 200$ms) (4.14b).

Similarly, we can write the upper and lower bounds for the signal attenuation:

$$S_{\min}^{\mathcal{N}}(b) = \frac{1}{\sum_k \ell_k} \sum_k \ell_k \exp\Big(-b\, D \cos^2\theta_k\Big), \tag{4.49}$$

$$S_{\max}^{\mathcal{N}}(b) = \frac{1}{\sum_k \ell_k} \sum_k \ell_k \exp\Big(-b\, D_{\min}^{\mathcal{T}_k} \cos^2\theta_k\Big), \tag{4.50}$$

Figure 4.15 shows the dMRI signals for the neurites trees with $50\mu\text{m} \leq \ell_{\text{k}} \leq 112.5\mu$m, in the gradient direction $\mathbf{g}/\|\mathbf{g}\| = (0,0,1)$ and at three diffusion times $\Delta = 2.5, 40,$ and 100ms. All simulated signals are between $S_{\min}^{\mathcal{N}}(b)$ and $S_{\max}^{\mathcal{N}}(b)$.

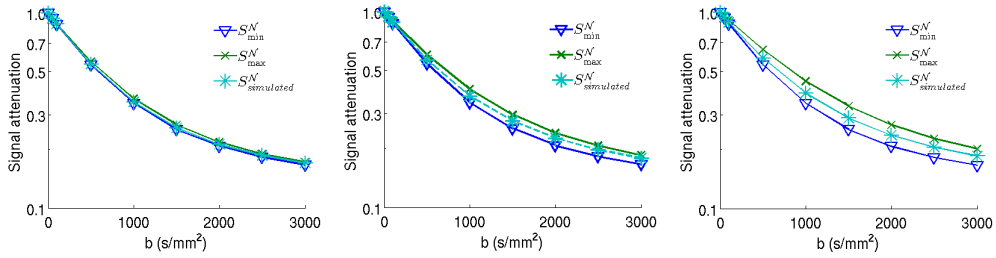

(a) (b) (c)

Figure 4.15: The signals for neurites with the length varying from 50 to 112.5μm and gradient direction $\mathbf{g}/\|\mathbf{g}\| = (0, 0, 1)$ and three diffusion times $\Delta = 2.5$ms (4.15a), $\Delta = 40$ms (4.15b) and $\Delta = 100$ms (4.15c).

Figure 4.15 shows the dMRI signals for the neurites trees with $20\mu\text{m} \leq \ell_{\text{k}} \leq 45\mu\text{m}$, in the gradient direction $\mathbf{g}/\|\mathbf{g}\| = (0, 0, 1)$ and at three diffusion times $\Delta = 2.5, 40,$ and 100ms. All simulated signals are between $S^{\mathcal{N}}_{\min}(b)$ and $S^{\mathcal{N}}_{\max}(b)$.

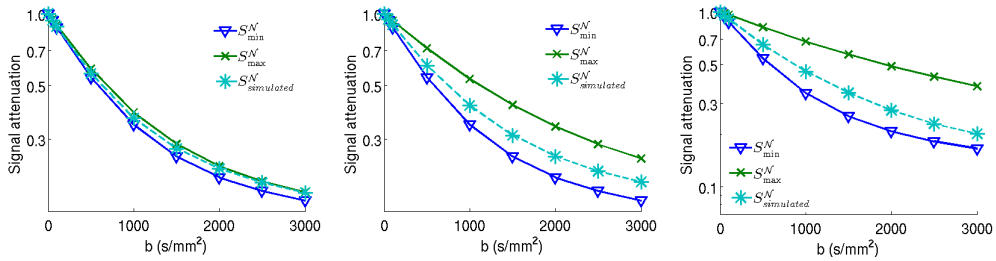

(a) (b) (c)

Figure 4.16: The signals for neurites with the length varying from 20 to 45μm and gradient direction $\mathbf{g}/\|\mathbf{g}\| = (0, 0, 1)$ for three diffusion times $\Delta = 2.5$ms (4.16a), $\Delta = 40$ms (4.16b) and $\Delta = 100$ms (4.16c).

4.8 Conclusion

We proposed two numerical models to simulate the dMRI signal arising from a single neuron by replacing the 3D simulation in the full neuron by a 3D simulation in the soma and 1D simulations in the neurites. The first model allows water exchange between the soma and neurites and it works better than the second model in which there is no exchange between them. However, the latter is still valid for many cases where the neurites are thin or long enough. Because the cross-sectional area of each cylindrical segment is taken into account, these models are accurate even for neurons with neurite segments of different radii. The transverse diffusion on each segment is analytically added that allows us to work with thick neurites or short diffusion times where the transverse diffusion is not totally neglectable. In addition to computational advantages, the two proposed models of the dMRI signal

of neurons, being more amenable to theoretical analysis due to the existence of (semi-)analytical results about diffusion in line segments, disks, and spheres, may be potentially exploited to produce semi-analytical expressions for the dMRI signal in neurons. Two models were implemented based on finite elements method for 1D line segments and coupled with the variable time-stepping RKC method. We used the implemented code to study the ADC inside neurites trees. First we validated an earlier published formula for the apparent diffusion coefficient. We also inverted the measured dMRI signal from a class of neurites trees to get the effective length which is close to the average length. This result may give a potential way to extract useful information about neurites structure from the measured dMRI signal. We also showed that for neurites trees containing two different segment lengths, the use of two effective longitudinal diffusivity gives better fits of the data, while two effective lengths obtained by the inversion can be used to estimate the two true lengths. Finally, we also derived the upper and lower bounds of the ADC and the signal attenuation inside neurite trees.

Chapter 5

Conclusion and Future work

5.1 Conclusion

We formulated and implemented a linear finite elements method coupled to the adaptive RKC time stepping method to solve the Bloch-Torrey equation. It enables us to work with general gradient pulses and complex geometries. The long-time limit of this equation from homogenization theory, Laplace equation, was also parallely considered. The interfaces are described accurately and the jump conditions of semi-permeable membrane is implemented by introducing zero-volume elements. The computational domain is periodically extended by appropriate boundary conditions. The PDE transformation simplifies the pseudo-periodic boundary conditions to periodic boundary conditions that reduces oscillation in the solution that allows getting more accuracy. In this way, the mass matrix is kept real-valued and time-independent that reduces memory usage and the time we enforce the boundary conditions for each time step. This method achieves the second order convergence in both time and space. This method has been implemented in the FeniCS C++ platform and coupled with the mesh generator Salome. Three application areas were considered. First, we showed the convergence of an apparent diffusion coefficient to the effective diffusion tensor computed by homogenization. Second, we numerically verified that an infinitely thin and semi-permeable membrane model can be used to approximate the finite thickness membrane model in which diffusion inside membrane is either isotropic or anisotropic. Third, we validated the macroscopic Kärger model that takes into account compartmental exchange.

We also proposed two numerical models of isolated neurons consisting of a spherical soma and cylindrical segments. These numerical models greatly reduce computational time and form a solid basis for developing further semi-analytical models of the dMRI signal arising from neurite trees. These models were also implemented in FeniCS C++ based on finite elements method for 1D segments, coupled with the RKC method. The simulations are performed to check the accuracy of the numerical models and to validate a published formula about the ADC. We also inverted the measured dMRI signal from a class of neurite trees to get the effective length which is close to the average length of tree segments. Finally, we proposed and

numerically checked the analytical upper bound and lower bound of the signal and related ADC inside neurite trees.

All these preliminary results show that the FEM-RKC code provided high performance and can be used as a guiding tool for further investigations in dMRI.

5.2 Future work on mesh generation

Although the mesh generator Salome was efficient for complex geometries with multiple compartments and periodic structures, our computational domains are still far from realistic biological structures.

First, in volume the intra-cellular space occupies about 6% in the cortex and 20% over all the brain tissues. This volume fraction is small compared to that of the computational domains that we could generate. For some special shapes like cubic or spherical cells, we may obtain such volume fractions but in general, it is very difficult to reach these values. The most complex geometries that we generated is formed by random cylindrical curves. In that case, the computational domain contains about 60% of the extra-cellular space which is much smaller than 6-20% in brain tissue. The problem remains how mesh generators like Salome can overcome singular points where the distance between two biological cells is very small (nearly touch each other). The Salome generator usually fails when working with complex geometries with such features.

Second, the resolution of dMRI (order of 1mm^3) is very large compared to cells features (from sub-micron for diameter of neurites to tens of micron for the soma). If neurites are described by 3D meshes in a computational domain, one has to deal with excessive number of elements and vertices to describe the structures accurately because the neurite diameter (order of μm) is much smaller than the neurite length (order of 1mm). This problem may be solved by generating anisotropic finite elements meshes or describing them in lower dimensions. In two proposed numerical models based on finite elements of 1D line segments, we effectively approached thin and long neurites. However, one also needs to include diffusion in the extra-cellular space, as well as the exchange across the biological cell membranes. That leads to another difficulty about how to link the anisotropic or lower dimension meshes of neurites/cells with that of the extra-cellular space.

All multi-compartment domains we generated were based on body-fitting features in a unique mesh, i.e. submeshes share the same nodes at the interface. However, for large scale problems in which the number of elements/vertices is excessive, it is better to generate meshes for compartments independently. Because vertices/faces of compartment meshes at common interfaces should be aligned, the way we link these meshes becomes very important and a vertex/face mapping at the interfaces may give a good way to manage this problem. This idea is very similar to the way one generates the periodic boundaries except that the mapping is built for a unique mesh in periodic boundaries and for different meshes in multiple compartments.

Figure 5.1 shows a forest of pyramidal neurons. One can imagine how hard to

describe correctly this geometry. The first problem is how to automatically place non-crossing neurites which are usually dense and easy to cross, in a computational domain with extra-cellular space. One can manually defines this domain (as what we did in chapter 2, about cylindrical curves) but it is very time-consuming and the volume fraction of the extra-cellular space is high.

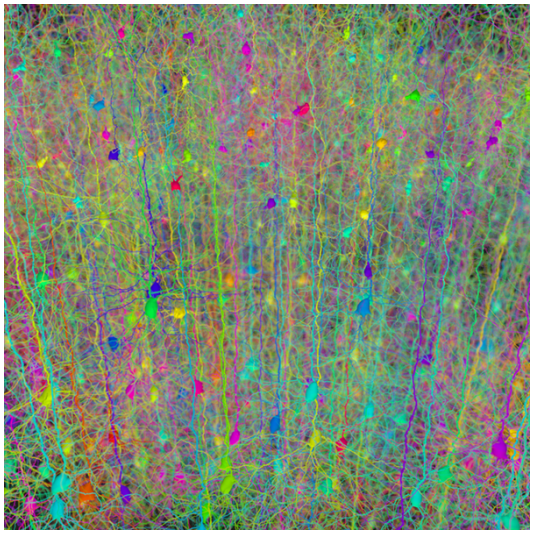

Figure 5.1: Image from Wikimedia Commons. Description: Forest of synthetic pyramidal dendrites grown using Cajal's laws of neuronal branching. Source http://commons.wikimedia.org/wiki/File:Forest_of_synthetic_pyramidal_dendrites_grown_using_Cajal%27s_laws_of_neuronal_branching.png, Author: Hermann Cuntz.

5.3 Future work on optimizing the FEM-RKC code

In FeniCS, parallel computing was considered in two paradigms. The first paradigm uses OpenMP for shared memory machines for some special purposes such as multi-threaded assembly for finite element matrices and vectors, linear solvers. The second one uses MPI to parallelize computations. For both paradigms, a mesh should be preprocessed in special ways. For multi-threaded parallelization, a so-called coloring approach is used, while for distributed parallelization, a mesh partitioning approach is used [43]. These features support well serial meshes in which each mesh includes all compartments. For large-scale problems with excessive number of vertices, this is disadvantageous in terms of memory usage.

Naturally, our code can be parallelized basing on subdomain decomposition. Fortunately, since our FEM-RKC method uses the explicit time stepping, each compartment can be managed separately and needs to be synchronized only once at the beginning of each time step. For two-compartment domains, four independent linear solvers can run in parallel.

5.4 Ongoing applications of FEM-RKC to dMRI

At this point, we recall that exact solutions to the Bloch-Torrey equation are known only for free space. It is therefore natural to resort either to approximate solutions or models (such as Gaussian phase approximation, narrow pulse approximation and macroscopic models), or to numerical techniques. The complexity of brain tissue often leads to the failure of classical approximations, especially at high b-values which are nowadays are available in MR scanners. The research for more accurate and elaborate models for fitting and interpreting experimental dMRI signal is very active.

The numerical analysis and three applications of the FEM-RKC method to dMRI show that the FEM-RKC code can offer high performance and enable us to work with complex geometries. Moreover, the FEM-RKC code allows one to operate easily with diffusion tensors that opens new possibilities in studying and modeling anisotropic diffusion in the brain.

List of Figures

List of Algorithms

Bibliography

[1] B. Aslanyürek, H. Haddar, and H. Çahintürk, *Generalized impedance boundary conditions for thin dielectric coatings with variable thickness*, Wave Motion, 48 (2011), pp. 681 – 700. (Cited on page 50.)

[2] Y. Assaf, R. Z. Freidlin, G. K. Rohde, and P. J. Basser, *New modeling and experimental framework to characterize hindered and restricted water diffusion in brain white matter*, Magnetic Resonance in Medicine, 52 (2004), pp. 965–978. (Cited on pages 61 and 62.)

[3] C. Beaulieu, *The basis of anisotropic water diffusion in the nervous system – a technical review*, NMR in Biomedicine, 15 (2002), pp. 435–455. (Cited on pages 7 and 47.)

[4] A. Bensoussan, J.-L. Lions, and G. Papanicolaou, *Asymptotic analysis for periodic structures*, vol. 5 of Studies in Mathematics and its Applications, North-Holland Publishing Co., Amsterdam, 1978. (Cited on pages 15 and 43.)

[5] F. Bloch, *Nuclear induction*, Phys. Rev., 70 (1946), pp. 460–474. (Cited on page 8.)

[6] M. D. Budde and J. A. Frank, *Neurite beading is sufficient to decrease the apparent diffusion coefficient after ischemic stroke*, Proceedings of the National Academy of Sciences, 107 (2010), pp. 14472–14477. (Cited on page 62.)

[7] N. Buhl and S. Jespersen, *A simulation framework for diffusion weighted mri in digitalized neurons: Extracting cytoarchitectural parameters using a new theoretical model for diffusion*, in Proc. Intl. Soc. Mag. Reson. Med, vol. 15, 2007, p. 1540. (Cited on pages 61 and 62.)

[8] P. Callaghan, *A simple matrix formalism for spin echo analysis of restricted diffusion under generalized gradient waveforms*, Journal of Magnetic Resonance, 129 (1997), pp. 74–84. (Cited on pages 10 and 21.)

[9] S. Chabert, N. Molko, Y. Cointepas, P. Le Roux, and D. Le Bihan, *Diffusion tensor imaging of the human optic nerve using a non-CPMG fast spin echo sequence*, J. Magn. Reson. Imaging, 22 (2005), pp. 307–310. (Cited on page 13.)

[10] H. Cheng and S. Torquato, *Effective conductivity of periodic arrays of spheres with interfacial resistance*, Proceedings: Mathematical, Physical and Engineering Sciences, 453 (1997), pp. 145–161. (Cited on pages 15 and 43.)

[11] C.-L. Chin, F. W. Wehrli, S. N. Hwang, M. Takahashi, and D. B. Hackney, *Biexponential diffusion attenuation in the rat spinal cord: computer simulations based on anatomic images of axonal architecture*, Magnetic resonance in medicine, 47 (2002), pp. 455–460. (Cited on pages 61 and 62.)

[12] C. A. Clark and D. Le Bihan, *Water diffusion compartmentation and anisotropy at high b values in the human brain*, Magn. Reson. Med., 44 (2000), pp. 852–859. (Cited on page 13.)

[13] J. Coatléven, H. Haddar, and J.-R. Li, *A new macroscopic model including membrane exchange for diffusion mri*. Submitted. See http://www.cmap.polytechnique.fr/ jingrebeccali/preprints.html, 2013. (Cited on pages 50 and 58.)

[14] Y. Cohen and Y. Assaf, *High b-value q-space analyzed diffusion-weighted mrs and mri in neuronal tissues–a technical review*, NMR in Biomedicine, 15 (2002), pp. 516–542. (Cited on page 7.)

[15] M. D. Does, E. C. Parsons, and J. C. Gore, *Oscillating gradient measurements of water diffusion in normal and globally ischemic rat brain*, Magn. Reson. Med., 49 (2003), pp. 206–215. (Cited on page 10.)

[16] E. Fieremans, D. S. Novikov, J. H. Jensen, and J. A. Helpern, *Monte carlo study of a two-compartment exchange model of diffusion*, NMR in Biomedicine, 23 (2010), pp. 711–724. (Cited on page 62.)

[17] L. GAREY, *Cortex: Statistics and geometry of neuronal connectivity, 2nd edn. by v. braitenberg and a. schÜz. (pp. xiii+249; 90 figures; isbn 3 540 63816 4). berlin: Springer. 1998.*, Journal of Anatomy, 194 (1999), pp. 153–157. (Cited on page 7.)

[18] S. Grant, D. Buckley, S. Gibbs, A. Webb, and S. Blackband, *Mr microscopy of multicomponent diffusion in single neurons*, Magn. Reson. Med., 46 (2001), pp. 1107–1112. (Cited on pages 61 and 62.)

[19] D. Grebenkov, *Nmr survey of reflected brownian motion*, Reviews of Modern Physics, 79 (2007), pp. 1077–1137. (Cited on pages 18, 21 and 68.)

[20] D. S. Grebenkov, *Pulsed-gradient spin-echo monitoring of restricted diffusion in multilayered structures*, Journal of Magnetic Resonance, 205 (2010), pp. 181–195. (Cited on pages 14 and 22.)

[21] ——, *Use, misuse, and abuse of apparent diffusion coefficients*, Concepts in Magnetic Resonance Part A, 36A (2010), pp. 24–35. (Cited on pages 36 and 62.)

[22] ——, *Pulsed-gradient spin-echo monitoring of restricted diffusion in multilayered structures: Challenges and solutions*, AIP Conf. Proc., 1330 (2011), pp. 65–68. (Cited on page 50.)

[23] H. HADDAR, P. JOLY, AND H.-M. NGUYEN, *Generalized impedance boundary conditions for scattering by strongly absorbing obstacles: The scalar case*, Mathematical Models and Methods in Applied Sciences, 15 (2005), pp. 1273–1300. (Cited on page 50.)

[24] K. D. HARKINS, J.-P. GALONS, T. W. SECOMB, AND T. P. TROUARD, *Assessment of the effects of cellular tissue properties on ADC measurements by numerical simulation of water diffusion*, Magn. Reson. Med., 62 (2009), pp. 1414–1422. (Cited on page 22.)

[25] M. A. HORSFIELD AND D. K. JONES, *Applications of diffusion-weighted and diffusion tensor mri to white matter diseases, a review*, NMR Biomed., 15 (2002), pp. 570–577. (Cited on page 7.)

[26] S. N. HWANG, C.-L. CHIN, F. W. WEHRLI, AND D. B. HACKNEY, *An image-based finite difference model for simulating restricted diffusion*, Magnetic Resonance in Medicine, 50 (2003), pp. 373–382. (Cited on page 22.)

[27] M. IBRAHIM, A. BUTT, AND M. BERRY, *Relationship between myelin sheath diameter and internodal length in axons of the anterior medullary velum of the adult rat*, Journal of the Neurological Sciences, 133 (1995), pp. 119 – 127. (Cited on page 47.)

[28] J. H. JENSEN, J. A. HELPERN, A. RAMANI, H. LU, AND K. KACZYNSKI, *Diffusional kurtosis imaging: The quantification of non-Gaussian water diffusion by means of magnetic resonance imaging*, Magnetic Resonance in Medicine, 53 (2005), pp. 1432–1440. (Cited on page 13.)

[29] S. JESPERSEN, L. LEIGLAND, A. CORNEA, AND C. KROENKE, *Determination of axonal and dendritic orientation distributions within the developing cerebral cortex by diffusion tensor imaging*, Medical Imaging, IEEE Transactions on, 31 (2012), pp. 16–32. (Cited on pages 61 and 62.)

[30] S. N. JESPERSEN, C. R. BJARKAM, J. R. NYENGAARD, M. M. CHAKRAVARTY, B. HANSEN, T. VOSEGAARD, L. ASTERGAARD, D. YABLONSKIY, N. C. NIELSEN, AND P. VESTERGAARD-POULSEN, *Neurite density from magnetic resonance diffusion measurements at ultrahigh field: Comparison with light microscopy and electron microscopy*, NeuroImage, 49 (2010), pp. 205–216. (Cited on pages 61 and 62.)

[31] S. N. JESPERSEN, C. D. KROENKE, L. ØSTERGAARD, J. J. ACKERMAN, AND D. A. YABLONSKIY, *Modeling dendrite density from magnetic resonance diffusion measurements*, NeuroImage, 34 (2007), pp. 1473–1486. (Cited on pages 61, 62 and 77.)

[32] J. Karger, H. Pfeifer, and W. Heinik, *Principles and application of self-diffusion measurements by nuclear magnetic resonance*, Advances in magnetic resonance, 12 (1988), pp. 1–89. (Cited on pages 56 and 58.)

[33] V. Kenkre, *Simple solutions of the torrey-bloch equations in the nmr study of molecular diffusion*, Journal of Magnetic Resonance, 128 (1997), pp. 62–69. (Cited on pages 12 and 16.)

[34] C. D. Kroenke, J. J. Ackerman, and D. A. Yablonskiy, *On the nature of the naa diffusion attenuated mr signal in the central nervous system*, Magnetic resonance in medicine, 52 (2004), pp. 1052–1059. (Cited on pages 61, 62 and 77.)

[35] L. J. Lanyon, *Diffusion tensor imaging: Structural connectivity insights, limitations and future directions*. (Cited on page 47.)

[36] M. Lazar, *Mapping brain anatomical connectivity using white matter tractography*, NMR Biomed., 23 (2010), pp. 821–835. (Cited on page 7.)

[37] D. Le Bihan and H. Johansen-Berg, *Diffusion mri at 25: Exploring brain tissue structure and function*, NeuroImage, 61 (2012), pp. 324–341. (Cited on page 7.)

[38] D. Le Bihan, J.-F. Mangin, C. Poupon, C. A. Clark, S. Pappata, N. Molko, and H. Chabriat, *Diffusion tensor imaging: concepts and applications*, Journal of magnetic resonance imaging, 13 (2001), pp. 534–546. (Cited on page 7.)

[39] D. LeBihan, *The 'wet mind': water and functional neuroimaging.*, Physics in medicine and biology, 52 (2007), pp. –. (Cited on page 47.)

[40] D. LeBihan, C. Poupon, A. Amadon, and F. Lethimonnier, *Artifacts and pitfalls in diffusion mri*, Journal of Magnetic Resonance Imaging, 24 (2006), pp. 478–488. (Cited on page 7.)

[41] J.-R. Li, D. Calhoun, C. Poupon, and D. Le Bihan, *Numerical simulation of diffusion mri signals using an adaptive time-stepping method*. Submitted, see http://www.cmap.polytechnique.fr/ jingrebeccali/preprints.html, 2013. (Cited on page 31.)

[42] J.-R. Li, D. Calhoun, C.-H. Yeh, C. Poupon, and D. LeBihan, *Efficient numerical solution of the bloch-torrey equation for modeling multiple compartment diffusion*, in ISMRM, 2011. (Cited on page 50.)

[43] A. Logg, K.-A. Mardal, G. N. Wells, et al., *Automated Solution of Differential Equations by the Finite Element Method*, Springer, 2012. (Cited on pages 22, 23, 24 and 93.)

[44] R. L. Magin, O. Abdullah, D. Baleanu, and X. J. Zhou, *Anomalous diffusion expressed through fractional order differential operators in the bloch-torrey equation*, Journal of Magnetic Resonance, 190 (2008), pp. 255 – 270. (Cited on page 13.)

[45] S. E. Maier, P. Bogner, G. Bajzik, H. Mamata, Y. Mamata, I. Repa, F. A. Jolesz, and R. V. Mulkern, *Normal brain and brain tumor: Multicomponent apparent diffusion coefficient line scan imaging1*, Radiology, 219 (2001), pp. 842–849. (Cited on page 13.)

[46] S. E. Maier, Y. Sun, and R. V. Mulkern, *Diffusion imaging of brain tumors*, NMR Biomed., 23 (2010), pp. 849–864. (Cited on page 7.)

[47] G. V. Michailov, M. W. Sereda, B. G. Brinkmann, T. M. Fischer, B. Haug, C. Birchmeier, L. Role, C. Lai, M. H. Schwab, and K.-A. Nave, *Axonal neuregulin-1 regulates myelin sheath thickness*, Science, 304 (2004), pp. 700–703. (Cited on page 47.)

[48] B. F. Moroney, T. Stait-Gardner, B. Ghadirian, N. N. Yadav, and W. S. Price, *Numerical analysis of {NMR} diffusion measurements in the short gradient pulse limit*, Journal of Magnetic Resonance, 234 (2013), pp. 165 – 175. (Cited on page 22.)

[49] M. Moseley, J. Kucharczyk, J. Mintorovitch, Y. Cohen, J. Kurhanewicz, N. Derugin, H. Asgari, and D. Norman, *Diffusion-weighted mr imaging of acute stroke: correlation with t2- weighted and magnetic susceptibility-enhanced mr imaging in cats*, AJNR Am J Neuroradiol, 11 (1990), pp. 423–429. (Cited on page 7.)

[50] R. V. Mulkern, H. Gudbjartsson, C.-F. Westin, H. P. Zengingonul, W. Gartner, C. R. G. Guttmann, R. L. Robertson, W. Kyriakos, R. Schwartz, D. Holtzman, F. A. Jolesz, and S. E. Maier, *Multi-component apparent diffusion coefficients in human brainâĂă*, NMR Biomed., 12 (1999), pp. 51–62. (Cited on page 13.)

[51] C. Neuman, *Spin echo of spins diffusing in a bounded medium*, The Journal of Chemical Physics, 60 (1974), p. 4508. (Cited on page 18.)

[52] T. Niendorf, R. M. Dijkhuizen, D. G. Norris, M. van Lookeren Campagne, and K. Nicolay, *Biexponential diffusion attenuation in various states of brain tissue: Implications for diffusion-weighted imaging*, Magn. Reson. Med., 36 (1996), pp. 847–857. (Cited on page 13.)

[53] D. S. Novikov, E. Fieremans, J. H. Jensen, and J. A. Helpern, *Random walks with barriers*, Nat Phys, 7 (2011), pp. 508–514. (Cited on page 62.)

[54] J. Pfeuffer, U. Flogel, W. Dreher, and D. Leibfritz, *Restricted diffusion and exchange of intracellular water: theoretical modelling and diffusion time dependence of 1H NMR measurements on perfused glial cells*, NMR in Biomedicine, 11 (1998), pp. 19–31. (Cited on page 21.)

[55] W. S. Price, A. V. Barzykin, K. Hayamizu, and M. Tachiya, *A model for diffusive transport through a spherical interface probed by pulsed-field gradient NMR*, Biophysical Journal, 74 (1998), pp. 2259–2271. (Cited on pages 21, 22 and 62.)

[56] R. H. Quarles, W. B. Macklin, and P. Morell, *Myelin formation, structure and biochemistry*, (2006). (Cited on page 47.)

[57] D. Rohmer and G. T. Gullberg, *A Bloch-Torrey Equation for Diffusion in a Deforming Media*, Dec 2006. (Cited on page 11.)

[58] G. Russell, K. D. Harkins, T. W. Secomb, J.-P. Galons, and T. P. Trouard, *A finite difference method with periodic boundary conditions for simulations of diffusion-weighted magnetic resonance experiments in tissue*, Physics in Medicine and Biology, 57 (2012), p. N35. (Cited on pages 22, 26 and 28.)

[59] F. K. Sanders, *The thickness of the myelin sheaths of normal and regenerating peripheral nerve fibres*, Proceedings of the Royal Society of London. Series B - Biological Sciences, 135 (1948), pp. 323–357. (Cited on page 47.)

[60] D. Schnapauff, M. Zeile, M. B. Niederhagen, B. Fleige, P.-U. Tunn, B. Hamm, and O. Dudeck, *Diffusion-weighted echo-planar magnetic resonance imaging for the assessment of tumor cellularity in patients with soft-tissue sarcomas*, J. Magn. Reson. Imaging, 29 (2009), pp. 1355–1359. (Cited on page 7.)

[61] J. Schröder, J. Bohl, and K. Brodda, *Changes of the ratio between myelin thickness and axon diameter in the human developing sural nerve*, Acta Neuropathologica, 43 (1978), pp. 169–178. (Cited on page 47.)

[62] P. N. Sen and P. J. Basser, *A model for diffusion in white matter in the brain*, Biophys J, 89 (2005), pp. 2927–2938. (Cited on pages 61 and 62.)

[63] B. P. Sommeijer, L. F. Shampine, and J. G. Verwer, *RKC: An explicit solver for parabolic PDEs*, Journal of Computational and Applied Mathematics, 88 (1998), pp. 315–326. (Cited on pages 22, 29 and 30.)

[64] N. Spruston, *Pyramidal neurons: dendritic structure and synaptic integration*, Nature Reviews Neuroscience, 9 (2008), pp. 206–221. (Cited on page 63.)

[65] G. J. Stanisz, G. A. Wright, R. M. Henkelman, and A. Szafer, *An analytical model of restricted diffusion in bovine optic nerve*, Magn. Reson. Med., 37 (1997), pp. 103–111. (Cited on pages 61 and 62.)

[66] E. O. Stejskal and J. E. Tanner, *Spin diffusion measurements: Spin echoes in the presence of a time-dependent field gradient*, The Journal of Chemical Physics, 42 (1965), pp. 288–292. (Cited on pages 10 and 12.)

[67] S. D. Stoller, W. Happer, and F. J. Dyson, *Transverse spin relaxation in inhomogeneous magnetic fields*, Phys. Rev. A, 44 (1991), pp. 7459–7477. (Cited on page 21.)

[68] G. Stuart, N. Spruston, and M. Hausser, *Dendrites*, Oxford Univ. Press, Oxford, New York, 1999. (Cited on page 63.)

[69] T. Sugahara, Y. Korogi, M. Kochi, I. Ikushima, Y. Shigematu, T. Hirai, T. Okuda, L. Liang, Y. Ge, Y. Komohara, Y. Ushio, and M. Takahashi, *Usefulness of diffusion-weighted mri with echo-planar technique in the evaluation of cellularity in gliomas*, J. Magn. Reson. Imaging, 9 (1999), pp. 53–60. (Cited on page 7.)

[70] A. L. Sukstanskii and D. A. Yablonskiy, *Effects of restricted diffusion on MR signal formation*, Journal of Magnetic Resonance, 157 (2002), pp. 92–105. (Cited on page 21.)

[71] E. Syková and C. Nicholson, *Diffusion in brain extracellular space*, Physiological Reviews, 88 (2008), pp. 1277–1340. (Cited on page 7.)

[72] A. Szafer, J. Zhong, and J. C. Gore, *Theoretical model for water diffusion in tissues*, Magn. Reson. Med., 33 (1995), pp. 697–712. (Cited on page 61.)

[73] H. Torrey, *Bloch equations with diffusion terms*, Physical Review Online Archive (Prola), 104 (1956), pp. 563–565. (Cited on pages 10 and 22.)

[74] Y. Tsushima, A. Takahashi-Taketomi, and K. Endo, *Magnetic resonance (mr) differential diagnosis of breast tumors using apparent diffusion coefficient (adc) on 1.5-t*, J. Magn. Reson. Imaging, 30 (2009), pp. 249–255. (Cited on page 7.)

[75] D. S. Tuch, T. G. Reese, M. R. Wiegell, and V. J. Wedeen, *Diffusion mri of complex neural architecture*, Neuron, 40 (2003), pp. 885–895. (Cited on page 7.)

[76] J. G. Verwer, W. H. Hundsdorfer, and B. P. Sommeijer, *Convergence properties of the Runge-Kutta-Chebyshev method*, Numerische Mathematik, 57 (1990), pp. 157–178. (Cited on page 39.)

[77] S. Warach, D. Chien, W. Li, M. Ronthal, and R. R. Edelman, *Fast magnetic resonance diffusion-weighted imaging of acute human stroke*, Neurology, 42 (1992), pp. 1717–. (Cited on page 7.)

[78] J. Xu, M. Does, and J. Gore, *Numerical study of water diffusion in biological tissues using an improved finite difference method.*, Physics in medicine and biology, 52 (2007). (Cited on pages 12, 14 and 22.)

[79] D. A. Yablonskiy and A. L. Sukstanskii, *Theoretical models of the diffusion weighted mr signal*, NMR Biomed., 23 (2010), pp. 661–681. (Cited on pages 7, 33, 47, 50 and 62.)